8.1.2.7 Epidotes, chevkinites, vesuvianite, orientite and related silicates

The above sorosilicates were classified in groups VIIIB15-VIIIB19 according to the Mineral Reference Manual [91N1]. Their compositions are listed in Table 1.

8.1.2.7.1 Crystal structure. Lattice parameters

Epidotes

The epidote group of silicates can be represented by the ideal formula $A_2M_3(SiO_4)(Si_2O_7)(O,F)(OH)$, where the A sites contain large, high coordination number cations such as Ca, Sr, rare-earth (R) etc., and the M sites are occupied by octahedrally coordinated, trivalent (occasionally divalent) cations such as Al^{3+}, Fe^{3+}, Mn^{3+}, Fe^{2+}, Mg^{2+}, etc. Epidotes consist primarily of the solid solution series between end members clinozoisite $Ca_2[Al_2Al]Si_3O_{12}OH$ and pistacite $Ca_2[Al_2Fe]Si_3O_{12}OH$. In general the amount of Fe^{3+} is restricted to 1.05 Fe apfu. Monoclinic members up to 0.5 Fe pfu are commonly called clinozoisite, and those with more than 0.5 Fe apfu, epidote [01G1].

The crystal structure of epidote was solved by [50I1] for iron rich species, and subsequently was confirmed in detail for other intermediate members of the series clinozoisite-epidote by X-ray [53B1, 54I1, 56F1, 71D1, 73G1, 80C1, 87S1, 95B1] and neutron difraction studies [78N1, 88K1] and for allanites [55U1, 59R1], wherein rare-earth (R) replace calcium, and ferrous iron or magnesium is found in octahedral sites in addition to aluminium and ferric ions.

The members of the epidote group (VIIIB15) - Table 1 - with the exception of zoisite crystallize in a monoclinic-type structure having space group $P2_1/m$ [68D1, 71D1]. The polyhedral connectivity is shown in Fig. 1 and the atomic sites are listed in Table 2. The structure contains chains of edge sharing octahedra of two types: a single chain of M2 octahedra and a multiple or zig-zag chain composed on central M1 and peripheral M3 octahedra. The chains are cross-linked by SiO_4 and Si_2O_7 groups. Finally, between the chains and cross-links there remain relatively large cavities which house the A1 and A2 cations. The differences in the occupation of only some sites (A2, M1 and M3) in epidotes determine changes in the coordination polyhedra surrounding these sites and result in minor modifications or mere rotation-translation of the connecting polyhedra. In the structure, Si1 and Si2 share O9, forming an Si_2O_7 group, while Si3 forms an isolated SiO_4 group. Each tetrahedron retains essentially its shape and size in all structures. The near uniform length of a given bond in various silicates of the group is consistent with local charge balance, since the degree of local charge imbalance is primarily a result of the topology and therefore is essentially the same. The O-Si-O angles in the Si_2O_7 group are all within 4^o of the ideal tetrahedral angle (109.5^o). The Si3 tetrahedron is somewhat distorted. The degree of flexing of the Si_2O_7 group i.e. the Si1-O9-Si2 shows variation in different structures and appears to be directly related to the solid-solution-caused expansion of the connected M3 octahedron. The Si1-O9-Si2 angle decreases more or less regularly from 164^o in clinozoisite to 145^o in allanite [71D1].

In the epidotes there is an unequal occupancy of the three octahedral positions (M1, M2 and M3). The M2 octahedral chain contains only aluminium atoms with the non-Al octahedral atoms substituting entirely into the other M1-M3 composite octahedral chain. Within the M1-M3 chain the occupancy is non-uniform. The peripheral M3 octahedra contain a larger fraction of the non-aluminium atoms (mainly Fe and Mn) than the central M1 octahedra. In clinozoisite and low iron epidote, the small amount of iron is present entirely in the M3 site. The remaining epidote minerals show substitution of (Fe,Mn) into M3 and M1, with a maximum of 34 % in the latter site being so replaced in allanite. This substitution into M1 occurs even though the M3 site is not completely occupied by (Fe,Mn). The maximum amount of (Fe,Mn) substitution into the M3 site is ~ 85 % with Al occupying the remaining 15 % [71D1]. Clinozoisite, epidote and low iron epidote have both the large A sites occupied entirely by calcium atoms. In the other epidotes the Ca atoms are partially replaced by other divalent ions such as Sr^{2+} and Pb^{2+} or trivalent R elements. All atoms replacing Ca are found only in the A2 site, none in the A1 site.

Where polyhedra share edges (such as the M1-M3 composite chain) the expansion of one polyhedron necessitates the expansion of (at least one edge of) the connected polyhedron, but there is little rotational reorientation between the two units. When only a corner is shared (such as between M3 and Si2 polyhedra) there is a possibility for rotation of one unit relative to the other. In the epidote series this rotation of polyhedra is a

prominent aspect of the structural difference between the members. Polyhedral expansion or contraction occurs at those sites involved in composition change but a single mechanism, involving mainly rigid rotation of polyhedra, allows all other polyhedra to retain their same geometries in all the structures [71D1].

Zoisite, the orthorhombic variety of the epidote mineral group with the idealized formula $Ca_2Al_2Al[SiO_4|Si_2O_7|(O|OH)]$, contains up to 20 mol % of hypothetical end member $Ca_2Al_2Fe^{3+}[SiO_4|Si_2O_7(O|OH)]$ (pistacite). Because of its stability at high pressure, it is considered to be an important carrier of H_2O to depth in subduction zones [98P2]. The structure of zoisite was determined by [55F1, 56F1] and later refined [68D1]. It contains one type of endless octahedral chain parallel to ***b*** with two distinct octahedral sites M1,2 and M3, which are occupied by Al (M1,2) and Al or Fe^{3+} (M3), respectively [71G1]. The octahedral chains are linked by SiO_4 tetrahedra (T3) and Si_2O_7 groups (T1 and T2) in the ***a*** and ***c*** directions. In this framework of interconnected octahedral chains there are irregularly shaped sevenfold-coordinated cavities (A1,A2) occupied by Ca. The Fe^{3+}-Al^{3+} substitutions in synthetic zoisite were analyzed [02L2]. Discontinuities in refined lattice parameters at ~ 0.05 x_{ps} ($x_{ps} = Fe^{3+}/(Fe^{3+}+Al\text{-}2)$ - Fig. 2 - were attributed to two distinct modifications: zoisite I (< 0.05 x_{ps}) and zoisite II (> 0.05 x_{ps}). The composition dependences of the lattice parameters for zoisite I are: $a = -3.72\cdot10^{-2}\, x_{ps} + 16.1913$, $b = 6.43\cdot10^{-2}\, x_{ps} + 5.5488$, $c = 3.43\cdot10^{-2}\, x_{ps} + 10.0320$ and for zoisite II: $a = -8.26\cdot10^{-2}\, x_{ps} + 16.2061$, $b = 8.14\cdot10^{-2}\, x_{ps} + 5.5486$, $c = 1.18\cdot10^{-1}\, x_{ps} + 10.0263$ where *a*, *b* and *c* are in Å [02L2]. In both modifications, substitution of Fe^{3+} expands the M3 octahedron, resulting in opposed rotations of the corner-linked T1 and T2 tetrahedra of the Si_2O_7 group. The extent of rotation is limited and controls the maximum Fe^{3+} content in zoisite I and II. With increasing Fe^{3+} content, zoisite I transforms to zoisite II and zoisite II to clinozoisite. The transformation from zoisite I to II can be classified as a substitutionally induced isosymmetric displacive phase transition.

The crystal structures of epidote [71D1, 80C1], clinozoisite [68D1] and piemontite [69D1] contain two large sites, A1 and A2 which are usually occupied by Ca, three tetrahedral sites occupied only by Si, and three octahedrally coordinated sites M1, M2 and M3 principally occupied by cations of charge (+3) as Al^{3+}, Fe^{3+} or Mn^{3+}. This gives rise to formula $Ca_2M_3^{3+}Si_3O_{12}(OH)$.

Synthetic Mn^{3+} piemontites, $Ca_2(Al_{3-x}Mn_x^{3+})[OH\,|\,O\,|\,(SiO_4)Si_2O_7]$, with $0.5 \le x \le 1.75$ were obtained [77A1]. Discontinuities in the lattice constants and refractive indices with respect to composition were observed. However, the partitioning of Mn^{3+} over the different octahedral sites M1, M2 and M3 in clinozoisite structure types was not solved. At a substitution degree of x = 0.25, Mn-bearing orthozoisite was found [77A1]. This variety was named “thulite“. In Fig. 3, the different octahedra into the clinozoisite-type structure, projected onto the (010) plane are plotted. The orientations of the ***a*** and ***c***-axis, occurring in this plane, as well as the two main optical directions ***X*** and ***Z***, as well as the internal octahedral axes of the M3 octahedron are given. In hancockite [71D1, 85D1], Pb and Sr substitute in A2.

In rare-earth (R)-bearing epidotes, the substitution of R^{3+} for Ca^{2+} in the A2 site requires the presence of divalent cations in the octahedral positions, in which the R-free members are occupied exclusively by trivalent cations. The coupled substitutions $Ca+(Fe^{3+}, Mn^{3+}, Al^{3+}) \Leftrightarrow R^{3+} + (Fe^{2+}, Mn^{2+}, Mg^{2+})$ can describe the complex isomorphous relationship occurring among the epidote-group of silicates counting R elements [94B1]. The dominant octahedral divalent cation is Fe^{2+} in allanite [60R1, 63K1, 71D1] and Mg in both dissakisite [91G1, 93R1] and dollaseite [88P1]. Minerals of this group with Mn^{2+} prevailing in the M3 site have also been found [91S2, 93B1]. An additional mechanism that could balance the entry of R^{3+} is the heterovalent substitution $OH^- \Leftrightarrow O^{2-}$ as suggested for the structure of dissakisite-(Ce) [93R1].

The hypothesis that the composition of allanite may extend toward the oxy-allanite component was suggested [91G1]. These authors reported that the variation in Ca does not correlate with the variation in M^{3+} (i.e. Al^{3+} + Fe^{3+}) content. This was tentatively attributed to an additional substitutional mechanism such as $(Fe^{2+}, Mg^{2+}) + OH^- \Leftrightarrow (Fe^{3+}, Al^{3+})+O^{2-}$, which leads to an ideal oxyallanite end member, $CaR(Al^{3+}, Fe^{3+})_3Si_3O_{13}$. The fact that allanite may be lacking in H is difficult to be verified [94B1]. The allanite-oxyallanite transformation was analyzed by ^{57}Fe NGR studies on natural samples [73D1]. According to this study, the reaction, which appears to be more temperature-dependent than time-dependent, starts above 400ºC and is essentially completed at ~ 700ºC. The Fe^{3+}-Fe^{2+}ratio can be varied continuously by increasing temperature and reversed to the original value by treatment under H_2 atmosphere. According to [64K1], by heating allanite, slight changes are induced in structure, which becomes more like that of epidote. The annealing experiments on allanite with different degree of

metamictization showed variations of the cell parameters due to restoring the crystallinity [93J1]. In [94B1] was shown that the presence of R^{3+} ions substituting for Ca requires the entry of divalent cations (Fe^{2+}, Mn^{2+}, Mg^{2+}) in the octahedral sites. Upon heating allanite and R-bearing piemontite in air, Fe^{2+} and Mn^{2+} oxidize. The charge balance is maintained by a corresponding H loss. The effect of heat treatment of allanite and R-bearing piemontite crystal structures were studied [94B1]. The oxidation-dehydrogenation process caused variations in the unit cell parameters. In particular, a shortening of ***b*** (which is parallel to the octahedral chains) was observed in the heat treated allanite crystal. In the sample of R-bearing piemontite, the increase of Mn^{3+}, due to the oxidation of Mn^{2+}, caused a strong Jahn-Teller effect on the M3 octahedron, resulting in a shortening of the octahedron along ***a***-axis. Therefore, the *a* parameter decreased more than *b* for increasing annealing temperature. In both allanite and R-piemontite, the relaxing of the H bond, directed along the ***c***-axes, resulted in a lenghtening of the *c* parameter. As the oxyallanite component increased, a corresponding increase in the value of β was observed [94B1].

The dissakisite-(Ce) is an Mg analogue of allanite-(Ce) with an ideal formula $CaCeMgAl_2Si_3O_{12}(OH)$. Allanites with $x_{Mg} = Mg/(Fe^{2+} + Mg) = 0.50…0.85$ were reported [41H1, 51K1, 61K1, 68K1, 87T1]. Then, the presence of $CaCeMgAl_2Si_3O_{12}(OH)$ was evidenced [74M1]. Later, the name of dissakisite-(Ce) was proposed for this Mg analogue of allanite [91G1]. The silicate crystallizes in a monoclinic structure having space group $P2_1/m$.

The analytical data for dollaseite-(Ce) lead to an apparent formula $CaR^{3+}Mg_2AlSi_3O_{11}(OH)F$, with two cations of charge (+2) and Al occupying the three octahedrally coordinated sites. The resulting charge unbalance is made up by substitution of R^{3+} for Ca as in allanite and by substitution of OH or F for the O atom not coordinated by Si. The dollaseite-(Ce) represents the probable limit of substitution of octahedrally coordinated M^{2+} cations in members of the epidote group [88P1]. Mg is ordered over two equipoints. Ca and R are each ordered over two different sites and F and OH are each ordered over two different sites. The R substitution occurs in the A2 site because that site has the larger radius in epidote-type structures that contain only Ca. In addition, A2 and M3 are linked through O8 and particularly O2. As Fe^{2+} substitutes in M3 of allanite and that substitution is balanced by that of R^{3+} for Ca, substitution of R in A2 provides a more satisfactory local charge balance for O2 and O8 [71D1]. The data are consistent with complete order of Mg in M1, Al (and presumably Fe^{3+}) in M2 and Mg+ Fe^{2+} in M3. This distribution gives rise to the most satisfactory local charge balance. It is also in agreement with the preferred distribution of Al in M2, other cations in M1 and M2 and Fe^{2+} in M3 [71D1]. The substitution relations in dollaseite-(Ce) imply that there may be a coupled substitution of $(F,OH)+Mg^{2+}$ for $O4+Al^{3+}$ (M1) [88P1]. Piemontite is the equivalent epidote in which iron is substituted by Mn^{3+} [79K1]. Mukhinite, having composition $Ca_{2.0}(Al_{2.1}V_{0.8}Fe_{0.1})Si_{3.1}O_{12\cdot0}(OH)$ may be obtained from clinozoisite with 1/3 of the Al replaced by V [69S1].

In epidotes, the intracrystalline distribution of Fe shows higher disorder than expected from the theoretical model [80B1]. Crystals synthesized at 600ºC have more Fe in the M1 than predicted; crystal synthesized at 700ºC have Fe also in the M2 site, which was not taken into account in the model. The experimental data of [73D1] do not show Fe in M2. Later on, [99G1] has shown that the crystals formed at 600ºC (0.65…0.73 Fe apfu) do not have any Fe in M2. Crystals formed at 700ºC (0.88…1.08 Fe apfu) have some Fe in the M2 site, its amount increasing with iron content in the sample. The dependence of the cell parameters on iron content is given in Fig. 4 [99G1]. The *b* parameter increases markedly with the Fe content, whereas the *a* and *c* parameters increase slightly; the β angle in turn decreases somewhat. Although the synthetic and natural samples are characterized by very different degree of Fe ordering, they both lie on the same trends. This suggests that the unit cell volume is not affected by the Al-Fe intracrystalline distribution.

According to [69D1], in piemontite, all the (Mn,Fe) substitution for Al occurs in one of the two nonequivalent chains of the edge-sharing octahedra. In the substituted chain, which is topologically identical with that found in the olivine structure, the larger M3 site (symmetry m) lying on the edge of the chain contains most of the (Mn,Fe) with lesser amounts in the smaller M1 site (symmetry $\bar{1}$) which forms the core of the chain.

From crystal chemical arguments, the existence of a hydrogen bond parallel to the crystallographic ***c***-axis was suggested [68D1].

There are two known polymorphs in the epidote group of minerals as mentioned above: orthorhombic zoisite (Pnma) and monclinic clinozosite ($P2_1/m$). The above polytypes can be interconverted by introduction of a shear between the different stacking modules [68D1, 86R1]. Thus, clinozoisite and zoisite structures are polytypes which can be described by stacking clinozoisite unit cell modules in the [100] direction [86R1]. The

displacement between each succesive stacking module of clinozoisite produces the twin orientation of the structure. The displacement is of an amount (1/4) [100] on (100) planes. The same displacement between every other stacking module creates the zoisite structure. In both cases reshuffing or synchroshear of the M3 and Ca^{2+} cations on the shear planes is required to create a stable cation arrangement. The observed stacking faults in zoisite can be interpreted as layers of clinozoisite within the zoisite structure. The displacement accross stacking faults are consistent with a displacement of the (1/4) [001] on each module boundary. Stacking faults in zoisite can be produced by the propagation of partial dislocations of the type [100] → (1/4) [001] + (3/4) [001] - Fig. 5. Within a given part of the crystal, the movement of each type of partial dislocation will create each of the twin orientation of the clinozoisite structure. Thus, if zoisite was to transform to clinozoisite by the propagation of both types of partial dislocations, then a multiply twinned clinozoisite structure would result. The partial dislocations move predominantly on (100) planes to produce planar stacking faults. In zoisites the partials are not constrained to the (100) planes and may migrate onto irregular planes at high angles to (100). Twinning in clinozoisite and stacking disorder in both clinozoisite and zoisite can be produced both by the propagation of partial dislocations and by growth. The propagation of partial dislocations in zoisite will be enhanced by deformation and by annealing within the clinozoisite stability field [86R1].

The crystal structure of zoisite, as above mentioned, consists of endless octahedral chains which are parallel to the ***b***-axis and which are formed by two types of Al–O octahedra sharing edges [55F1]. These chains are cross-linked by isolated tetrahedrally SiO_4 and Si_2O_7 groups and two types of CaO_7 polyhedra. The aluminium atoms occur in two crystallographically different sites. The first Al1, is in eightfold general position 8d with point symmetry 1, while the second, Al2, is a fourfold special position 4c, with point symmetry group m. The hydrogen atoms occur in a fourfold special position 4c, with point symmetry group m. Each Al1 is coordinated by one OH group.

According to [71H1, 87B2], the Fe^{3+} and Cr^{3+} are substituted in the larger Al2 sites of the zoisite structure. No local relaxation for Fe^{3+} was evidenced [87B2]. The crystal structure data predict a negative sign of B_2^o. For Cr^{3+}, significantly larger differences between observed and calculated zero field splitting patterns were found, suggesting relaxation effects due to the non-spherical electron distribution in the ground state of this ion [87B2].

Chevkinite - perrierite group

In early studies, the structures of naturally occurring chevkinite [64P1] and perrierite [60G1] were refined in space group C2/m and were shown to be similar. Later on, [71I1] confirmed the suggestion [59B2] that perrierite has a primitive cell and indexed the power patterns of the synthetic silicates in space group $P2_1/a$. The unit cells of these silicates are related [66B1]. These minerals can be represented as $A_4^{3+}B^{2+}C_2^{3+}Ti^{4+}(Si_2O_7)_2O_8$ where A = R, Th, Ca, Sr, Na, K in 10-fold coordination, B = Fe^{2+}, Mg, Mn, Ca in 6-fold coordination, C = Ti, Mg, Mn, Fe^{3+}, Fe^{2+}, Al in 6-fold coordination [71I1]. In [74C1] was stated that 9-fold coordination occurs in the A position. The chevkinite structure is stabilized relative to perrierite by temperature, as well as by A ions with smaller radii and by B and C ions with larger radii [67I1, 71I1, 74C1, 78S1].

The main structural features of the two minerals are essentially the same, consisting of sheets of octahedrally coordinated C1, C2 atoms in perrierite and C1, C2A and C2B in chevkinite running parallel to the (001) plane and separated by ***c***-axis translation -Fig. 6. Referring to compositions given in Table 2b,c, these sheets are interleaved with a layer consisting of a double thickness of Si_2O_7 groups and MgO_6 and CoO_6 octahedra (in Co-chevkinite). For conveniency Mg and Co were designated as B ions. Each disilicate group is joined to six MgO_6 octahedra, forming a layer with the composition n $[Mg(Si_2O_7)_2]$. The rare-earth ions lie between the disilicate ions and the sheet of octahedra. The disilicate ions in the two structures are bent significantly at the bridging oxygen atom. The anions have nearly m symmetry. The pseudo-mirror plane is defined by the two silicon ions and O6, O7 and O8. The bridging oxygen atom is shared with R1 in each structure. Each structure had a B ion on the center of symmetry. The octahedra show a large tetragonal distortion with B-O6 bond length contracted by more than 0.15 Å. The Mg and Ti are non randomly distributed among the remaining cation sites. Site C2 has 0.884 Ti in perrierite and shows high distortion. Adjacent $C2O_6$ octahedra are generated by the 2_1 axis and C2 octahedra share edges which are nearly normal to the ***a***-axis. Analogous to that of C2 in perrierite are the C2A and C2B octahedral sites in chevkinite, each of which has $\bar{1}$ site symmetry and contains 0.81 and 0.83 mol % Ti, respectively. These octahedra are more regular than in perrierite. The C1 site in perrierite contains 0.62 mol % Ti

and in Mg-chevkinite 0.68 mol % Ti - see also Table 2. The structures of these silicates are related [66B1], that is, with the ***a***-axes antiparallel and the ***c***-axis of chevkinite parallel to the $a + 2c$ direction of perrierite. If the origin of the mirror image - Fig. 6b - is superimposed upon the $x = 1$, $z = 1/2$ position of Fig. 6a, the structures nearly superimpose. In natural chevkinites and perrierites, titanium predominates in the C positions, particularly C2, Fe^{2+} predominates in the B sites and the larger rare-earth (primarily La and Ce) are mainly located in the A positions.

Certain compositions (e.g. $Pr_4Mg_2Ti_3Si_4O_{22}$ and $Pr_4Ni_2Ti_3Si_4O_{22}$) can exist in both structural states [71I1]. It was concluded that the dimorphism occurs, but only within fairly narrow chemical limits and that perrierite transforms to chevkinite with increasing temperature. According to [78S1] the phase change chevkinite-perrierite is controlled primarily by composition. As before mentioned, both structures consist of alternating layers - Fig. 6c - in which one layer consists of C atoms in octahedral coordination with oxygen and the other layer of $B(Si_2O_7)_2$ groups. Because the layers are firmly linked by shared oxygens, the size of the B and C cations exerts a strong control over the size of the unit cell. In the chevkinite structure, very large cations can therefore only be accommodated in the A sites either by increasing the average size of B and C cations to open up the structure or by distorting it to give the perrierite structure.

Strontio-chevkinite crystallizes in a monoclinic lattice having space group $P2_1/a$ [83H1, 84D1]. The name is from the chemical and crystallographic relation to chevkinite.

Karnasurtite is an amorphous silicate [59V1]. After being heated at 900ºC it gives a pattern close to that of huttonite.

Vesuvianite

The crystal structure of vesuvianite was solved in the space group P4/nnc [31W1]. This symmetry was assumed to be correct until the work of [69A1]. By using precession photography, these authors showed that one or more of the glide plane extinction criteria for P4/nnc symmetry are violated. Vesuvianite sample from several localities have P4/nnc symmetry; for other samples the symmetry is reduced. The crystal structure of vesuvianite was refined [70C1, 75R1, 83G1, 86F1, 86Y1, 92A1, 92O1]. A full discussion concerning the crystal structures of vesuvianite was given by [00A1]. A simplified formula of tetragonal vesuvianite taking into account the various cation coordinations and its domain structure may be written as $X_{18}X'Y_{12}Y'Si_{18}O_{69}(OH,F)_9$, where X and X' are seven to nine-fold-coordinated, Y has octahedral coordination, Y' has square pyramidal coordination and Si has tetrahedral coordination. X and X' are commonly occupied by Ca. Y and Y' are host elements with an average valence 2.85 (e.g. 11Al and 2Mg). X' and Y' occupy strings along the fourfold axes. In the space group P4/nnc these strings have the sequence Y'X'X'Y', but due to short X'X' and Y'X' distances, occupied sites always alternate with vacancies (□). Thus, a string along a fourfold axis has locally either Y' □ X' □ or □ X' □ Y' arrangement. Each string itself is fully ordered (short range ordering), however, adjacent strings are either long-range disordered (space group P4/nnc) or they follow some specific ordering patterns leading to decreased symmetry [83G1, 86F2, 92A1, 98P1]. Subgroups of space group P4/nnc allowing for long-range string ordering are P4/n, centric, and P4nc, acentric [83G1, 86F2, 92A1]. In [92A1] was argued that the long-range ordered space groups are characteristic at low temperatures (<300ºC), whereas high-temperature (400…800ºC) vesuvianites are long-range disordered in agreement with P4/nnc symmetry. String ordering takes place during crystal growth rather than by ordering transformation on cooling [00A1].

The structural and chemical studies on long-range disordered P4/nnc vesuvianite [86F1, 86Y1, 92G1, 92G2, 92O1, 93G1, 94G1, 94G2, 95G1] addressed various substitution mechanisms like boron incorporation and F-OH replacement and provided information on the local configurations of cations and OH,F sites. A boron rich vesuvianite has been defined [98G1]. Deviations from P4/nnc symmetry were either analysed in terms of glide plane violating reflections in single crystal diffraction patterns or by the presence of a slight piezoelectric or second harmonic generation (SHG) effect [69A1, 83G1, 86F2, 92A1, 93G1]. Three types of glide violating reflections were distinguished: (1) hk0 with h+k = 2n+1; (2a) 0kl with k + l = 2n + 1; (2b) hhl with l = 2n + 1. Type (1) violates the n glide plane perpendicular to the fourfold axis, type (2a) violated the n glide plane in (100) and type (2b) violates *c* glide plane in (110). Occurrence of type (1) reflection excludes space group P4/n and P4/nnc and suggest P4nc. Observation of reflections of the type (2a, 2b) excludes P4nc and P4/nnc leading to space group P4/n. The piezoelectric or SHG effect is only possible in the acentric space group P4nc. Frequently, all three types of weak glide violating reflections were observed or only types (2a, 2b) were present but the

piezoelectric effect was also observed [00A1]. Thus, it had to be assumed that such vesuvianites have a complex domain structure assembled of individual P4nc and P4/n domains [85V1, 86F1, 92A1]. Electron microscope studies [91V1, 93G1] show that the symmetry of some vesuvianites is non-tetragonal but monoclinic P2/n, leading to pseudomerohedral twins. Non-tetragonal symmetry may also be caused for deviations from uniaxial optical behaviour found in many vesuvianites [93G1]. It has been suggested that there is a continuous ferroelastic phase transition between a high-temperature P4/nnc structure and low-temperature P2/n or Pn structures [93G1]. In [00A1] was shown that low-temperature vesuvianites crystallize in two space groups P4/n and P4nc, due to different arrangements of Ca-dodecahedra and $M^{2+,3+}$ square pyramids that form strings along the fourfold axes - Fig. 7 [00A1]. Long-range ordered vesuvianites of acentric P4nc symmetry may have the same diffraction symmetry as centrosymmetric disordered P4/nnc ones. As pointed out by [00A1], a string arrangement according to space group P4nc (apices of the square pyramids pointing in the same direction) does not lead to glide violating reflections (hk0) with h + k = 2n + 1, which were commonly used to distinguish space group P4/nnc from P4nc. In contrast P4/n long-range ordered vesuvianites exhibits glide plane violating reflections. The square pyramidal Y'3a site (string A) occupied by Mn and Cu displays a characteristic 4 + 1 coordination (4 × Y'3a-O6a and 1 × Y'3a-O10a). In contrasdt Y'3b is more regular (string B) with 4 × Y'3b-O6b and 1 × Y'3b-O10b. The studies performed on some vesuvianites crystals [00A1] reported that the untwinned sample[75)] having Cu^{2+} and Mn^{2+}, Mn^{3+} forming the square pyramid, exhibits an acentric ordering pattern with 85 % string A and 15 % string B (space group P4nc) - Table 2. The P4/n vesuvianite[76)] is composed of a merohedral twin with a close to 1:1 twin ratio and has mainly Fe^{3+} in square pyramidal coordination. In this centric structure, string A is 84 % and string B is 16 % occupied. In P4/nnc structure was noted [70C1, 86F1, 86Y1] that O10 and O11 were associated with H atoms. Preferred occupation of string A in P4nc vesuvianite determines a favorable orientation of the OH vector at O10. If O10a is part of the square pyramid, the OH group is at O10b and forms a hydrogen bond to O10a - Fig. 7c . The H11a and H11b positions are given in Fig. 8 [96G1, 99L1, 00A1]. In P4/n structure the hydrogen positions forming the OH groups are at O11a and O11b [98P1, 00A1] - Fig. 8. Acceptors of weak hydrogen bonds are O7a, O7b, O11a and O11b. The atomic positions for P4nc and P4/n structures are listed in Table 2.

The EXAFS method was used to investigate the local environments of Cu and Mn ions in natural vesuvianites as well as the site occupancy [92O1]. As above mentioned one of peculiar feature of vesuvianite is the 5-fold coordinated square-pyramidal site Y' (in some papers is denoted by B) , located on the 4-fold symmetry axis. This site, having 4mm (C_{4v}) symmetry, strongly deviating from octahedral symmetry, is preferently occupied by Jahn-Teller ions Cu^{2+} [86F1, 92D2] or Mn^{3+} [95P1]. In [92G1, 92G2] was supposed that small amounts of Mn^{2+} may be located also in Ca1-Ca3 sites. According to [76M1] insignificant amounts of Fe^{3+} may occupy antiprismatic positions.

Wiluite - Table 1 - is a boron-rich vesuvianite group of silicates [98G1].

For crystal structure of P4/nnc vesuvianite see also [75R1].

Danburite

The crystal structure of danburite, $CaB_2Si_2O_8$, was firstly analysed by [31D1] and later studied by [59B1, 59J1]. The refinement of the structure was performed by [74P1]. The asymmetric unit of danburite contains two tetrahedrally coordinated cations (T = B and Si), one calcium and five oxygen atoms - Table 2. The O1, O2 and O3 are bonded to both Si and B, whereas O4 and O5 are the bridged oxygens of the Si_2O_7 and B_2O_7 groups. The structure can be thought of as a continuous framework of alternating B_2O_7 and Si_2O_7 groups with the Ca atoms in either 9-fold coordination or 7-fold coordination. According to [74P1] the 7-fold coordination model appears to be more consistent with structurally similar anorthite, reedmergnerite and albite (see volume on tectosilicates) as evidenced by the linear relationship between the mean Na/Ca-O bond lengths and the mean isotropic temperature factors of Na and Ca in these structures. The high-temperatrure analysis of the crystalline structure [85S1] seems to support a nine-coordination, rather than seven for the Ca atom. A portion of the structure viewed down ***c***, showing the 4- and 8-membered rings formed by the alternating B and Si – containing tetrahedra is plotted in Fig. 9. The danburite contains double-crankshaft chains which consist of 4-membered rings of tetrahedra. Within these rings two adjacent tetrahedra have apical oxygen atoms that point up and two that point down. The 4-membered rings are tilted with respect to the chain axis, which is parallel to ***c***. The silicon and boron tetrahedra within a 4-membered ring are always linked to like tetrahedra in mirror-related rings directly above and below in the chain, forming Si–O–Si and B–O–B linkages.

The crystal structure of danburite has been studied at temperatures up to 900ºC. The temperature dependences of the lattice constants are given in Fig. 10 [85S1]. The thermal response of the structure is basically characterized by an unusual expansion of a specific bond, B-O2 of the borate tetrahedron, the thermal expansion coefficient of the bond being $1.6 \cdot 10^{-5}$ °C^{-1} in the temperature range 400…900ºC. In accordance with such expansion, the Ca-O2 bond shows a relative contraction with an increase of temperature.

The compressibilities of danburite has been determined between 0 and 5 GPa [92H1]. The dependences of lattice parameters on pressure are plotted in Fig. 11. The bulk modulus is K = 113.6 (2.9) GPa and K' = 4.

The electrostatic potential, total electron density and its Laplacian distribution, $\nabla^2\rho(\boldsymbol{r})$, in danburite have been analysed [92D1]. The topology of the Laplacian distribution and the fact that $\nabla^2\rho > 0$ at the bond critical points indicates the Ca–O, B–O and Si–O interactions to be mainly closed shell in nature. The pattern of oxygen valence shell charge depletion, as revealed in maps of $\nabla^2\rho(\boldsymbol{r})$, indicates that the oxygen valence shell is less locally depleted near bond paths and more depleted between bonds. This pattern of local charge concentration and depletion appears consistent with features in the electrostatic potential around bridging oxygens.

Ruizite, macfallite, orientite, sursassite, ardennite

Macfallite crystallizes in a monoclinic-type structure having space group $P2_1/m$ [79M1, 85M1]. According to [77W1] ruizite crystallizes in space group $P2_1/c$. Later on, the monoclinic structure was indexed in space group C2/m [85M1]. Different structure models have been proposed for this group of silicates, particularly orientite [82M1, 85M1, 86M1]. A comprehensive appraisal of the chemical and structural relationship within the family of 6x9 Å modular sheet structure was presented [85M1]. All of them have lattice parameters that are 6 and 9 Å long, while the third parameter varies from silicate to silicate. All these structures can be build starting from $^{2}_{\infty}\left[M^{3+}_{2}\varphi_2(SiO_4)_2\right]$ sheet where M is an octahedrally coordinated cation and φ is usually hydroxyl (OH). Successive sheets sandwich variable intersheet material, which consists of both octahedral and tetrahedral coordination polyhedra. For example, the intersheet compositions are $Ca_2(H_2O)_2Si_2O_3(OH)_2$ for ruizite, $Ca_2Mn^{3+}(OH)SiO_3$ for macfallite and $Ca_2(H_2O)_2SiO_2$ for orientite. On the basis of this approach for orientite was proposed a structural model in which adjacent $^{2}_{\infty}\left[M^{3+}_{2}\varphi_2(SiO_4)_2\right]$ sheets are connected through additional SiO_4 tetrahedra and this connection give rise to Si_3O_{10} groups - Fig. 12a [85M1, 86M1]. The authors were aware of the disordered nature of orientite and assumed that the central tetrahedral site had only partial occupancy, the corresponding SiO_4 sheets in the structure being partially substituted by sheets of half occupied manganese octahedra [85M1]. This model involves space group Ccmm in the unit cell setting of Fig. 12a (the ***c***-axis indicating the direction along which the sheets are stacked and the ***b***-axis indicating the direction of the edge sharing octahedral chains). A different setting was assumed by [85M1], with the space group Bbmm which transforms to Ccmm by the [100/001/010] matrix. In this model the ideal unit cell was $Ca_8Mn^{3+}_8(Si_3O_{10})_4(OH)_8 \cdot 8H_2O$.

A different structure model was proposed by [82M1], who developed it starting from the structural relationship existing between sursassite and pumpellyite - see section 8.1.2.8. Surssasite, $Mn^{2+}_4Al_6[(OH)_6(SiO_4)_2(Si_2O_7)_2]$, and pumpellyite, $Ca_4Al_6[(OH)_6(SiO_4)_2(Si_2O_7)_2]$, apart from the different chemical contents are built up from identical structural layers repeated according to different stacking sequences [86M1]. The distinctive feature in the two structures lies in the different ways by which successive layers connect with each other through the octahedral sheets. Whereas in pumpellyite similar silicate groups (ortho-ortho and diortho-diortho) face each other, in sursassite different groups (ortho and diortho) face each other on the two sides of the octahedral sheets [84M1, 86M1]. Similarly, end member ardennite, $Mn^{2+}_8Al_{12}[(AsO_4)_2(SiO_4)_4(Si_3O_{10})_2(OH)_{12}]$ is characterized by orthosilicate and trisilicate groups, with different groups facing each other - Fig. 12b [86M1]. By analogy with sursassite-pumpellyite structures, a different structural modification for orientite was envisaged in the [82M1] model, with similar groups facing each other - Fig. 12c. It has the space group Pcmm, whereas Pnmn is the space group for ardennite. The ideal unit cell content for orientite was $Ca_8Mn_{12}[(SiO_4)_6(Si_3O_{10})_2(OH)_{12}]$.

The [82M1] and [85M1] models differ only in the structural slabs between $z = 0.18$ and $z = 0.32$ and between $z = 0.68$ and $z = 0.82$. In the model [85M1] these slabs consist of silicate tetrahedra and water molecules, whereas in the model [82M1] they contain edge-sharing Mn^{3+} octahedra with silicate tetrahedra attached on the two sides of the octahedral chains. As a consequence, the two models differ also in chemical composition with [85M1] and [82M1] models containing respectively eight and twelve octahedral cations per unit cell.

The recalculation of chemical analysis of natural orientite pointed out the presence of ten octahedral cations per unit cell [79M1]. As a result a third model was developed - Fig. 12d [86M1]. This model involves the space group P2mm and is characterized by regular alternation of [82M1] and [85M1] structural slabs. Correspondingly, its ideal chemical formula is intermediate between the models [82M1] and [85M1], the end composition being $Ca_8Mn_{10}^{3+}(SiO_4)_2(Si_3O_{10})_3(OH)_{10}\cdot 4H_2O$. As mentioned by [86M1], the three models present the same scaffolding of oxygen atoms and differ only in the location of tetrahedral and octahedral cations in the slabs between $z = 0.18$ and $z = 0.32$ and $z = 0.82$. Therefore, the three models are expected to produce the same X-ray diffraction pattern, as all of them simulate a common Ccmm supersymmetry.

The crystal structure of orientite is described in Fig. 12d in terms of the main constituent unit, according to the model of [86M1]. The main structural units are chains of edge-sharing Mn^{3+} octahedra which run along [010] and are connected by (SiO_4) orthosilicate and (Si_3O_{10}) trisilicate groups. The orthosilicate and trisilicate groups are stippled in Figs. 12 by different tones of gray to indicate their different y levels. Four independent calcium cations Ca1 and Ca3 on the mirror plane at $y = 0$ and Ca2 and Ca4 on the mirror planeat $y = 1/2$ are linked to seven oxygen atoms. The three independent tetrahedral sites - Table 2h - possess a common distortion which is due to the marked Jahn-Teller effect for high spin Mn^{3+} cations: the coordination is a tetragonal bipyramid with four shorter and two longer Mn^{3+}-O distances. The mean distance for the four short bonds is 1.93 and 1.94 Å for the Mn1 and Mn3 as found in ruizite and macfallite [85M1] and 2.04 Å for the Mn2 site.

The projections of the ruizite and macfallite structures on the plane (010) and of orientite on plane (001) are given in Fig. 13 [85M1]. The tetrahedral interlayer links for these structure are plotted in Fig. 14, while in Table 2 the atomic positions are listed.

As above mentioned, sursassite is isostructural with macfallite having $P2_1/m$ space group [84M1]. Its microstructure displays varying degrees of disorder and structural defects. The dominant defect consists of stacking faults parallel to (001). The structure of ardennite is characterized by chains of edge sharing ($Al,Mg.Fe^{3+}$) octahedra, connected by orthosilicate and trisilicate groups. A slightly larger tetrahedron is occupied by As^{5+} (and V^{5+}) cations. Mn^{2+}, Ca^{2+} and Mg^{2+} occur in the cavities of the structure in six- and seven-fold coordinations [68D2, 71A1, 91P1]. In the model of [85M1], as for the ruizite, macfallite and orientite, both structures are based on the same fundamental building block, a sheet of $^2_\infty\left[M_2^{3+}\square\varphi_2(TO_4)_2\right]$ where φ is an anion not associated with a tetrahedron and □ is a vacancy. In sursassite, the fundamental building block is $Al_2(OH)_2(SiO_4)_2$ and the intersheet is $Mn_2^{2+}Al(OH)SiO_3$. In ardennite the building block is $2Al_2(OH)_2(SiO_4)_2$ and the intersheet is $Mn_4^{2+}Mg_2(OH)_2SiO_2AsO_4$ [85M1]. The structure of ardennite has been discussed also in terms of the OD-theory [79D1, 91P1]. The occurrence of complex polytypes intergrown within the ardennite matrix was shown [91P1].

Kittatinnyite crystallizes in a hexagonal-type structure having space group $P6_3/mmc$, $P6_3mc$ or $P\bar{6}2c$ [83D1].

$Mg_5Al_5Si_6O_{21}(OH)_7$

The high pressure phase, $Mg_5Al_5Si_6O_{21}(OH)_7$, was named initially MgMgAl-pumpellyite [86S1], in analogy to the phase MgAl-pumpellyite $Ca_4(MgAl)Al_4[Si_6O_{21}(OH)_7]$ [80S1]. The lattice parameters were determined on the basis of the A2/m space group as in MgAl-pumpellyite [86S1, 91S1]. Later on, [99A1] investigated the phase having the composition $Mg_5Al_5Si_6O_{21}(OH)_7$ and modeled it in terms of the pumpellyite structure, by using the space group $P2_1/m$. In addition, extensive stacking disorder along [001] was reported with a statistical cation distribution on the octahedral and tetrahedral sites. In [00G1], the crystal structure of the high-pressure phase $Mg_4(MgAl)Al_4[Si_6O_{21}(OH)_7]$, referred as MgMgAl pumpellyite, was found to be isostructural with *sursassite* rather than pumpellyite. This phase was considered as slightly modified Mg-analogue of sursassite $Mn_4^{2+}Al_2Al_4[Si_6O_{22}(OH)_6]$ with Mg- for Mn and one Al replaced by Mg + H. For a sample synthesized at 5

GPa and 600ºC a monoclinic $P2_1/m$ space group was reported [00G1]. The HRTEM investigations did not suggest any stacking disorder along [001] or sursassite-pumpellyite intergrowth.

The bulk modulus is K_T = 116.0 (1.3) GPa and K' = 4. The variation with temperature of the bulk modules is $(\partial K_T/\partial T)_p$ = –0.011 (4) GPa K^{-1} [01G1].

8.1.2.7.2 Magnetic properties

Ardennite

In the ardennite structure the Fe^{3+}, Cu^{2+} and Cr^{3+} are widely separated, so that their magnetic contributions can be assumed to be paramagnetic in character. The Mn atoms occupy two 4-fold sites (4f) with point symmetry m. In the M1 site only manganese atoms are located. In the M2 site, calcium atoms may substitute for manganese. The Mn1-Mn1 and Mn2-Mn2 exchange interactions take place through their shared oxygen atoms. When both sites are occupied by Mn atoms, local exchange will take place as for the Mn1-Mn1 case. If a calcium atom substitutes for one of the manganese atoms in the M2 site, the remaining Mn contributes a paramagnetic component to the total susceptibility. In the ground state (0 K) the spins of the pair of ions (Mn,Mn) separated by the mirror plane parallel to the [010] direction are in opposite direction [69T1]. The magnetic properties were analyzed considering the Hamiltonian $\mathbf{H} = 2\mu_o MgH_s = 2J\boldsymbol{S}_1\boldsymbol{S}_2$, where J is the exchange integral, g the spectroscopic splitting factor, H_s is the magnetic field in the [010] direction and M is the magnetic moment. In the direction perpendicular to y, J is small.

The temperature dependences of the magnetic susceptibilities ∥ and ⊥ to [010] direction are plotted in Fig. 15 [69T1]. The data were fitted with the relation $\chi = [A + 3kG(\Theta)]\frac{1}{T} + N(\alpha)$ [60E1], where $A = \frac{NM^2\mu_o}{3k_B}$; $k = \frac{g^2NM^2}{3k_B}$, $N(\alpha)$ is a temperature independent term, N the number of paramagnetic atoms and $G(\Theta)$ is a function of $-J/k_BT = \Theta/T$. Values A = 16.90·10^{-4} emuK/g, $3k$ = 45.7·10^{-4} emuK/g, $\Theta_\parallel$ = 1.50 K, $\Theta_\perp$ = 1.55 K and $N(\alpha)$ = 8.7·10^{-6} emu/g were determined [69T1].

8.1.2.7.3 Nuclear gamma resonance (NGR) data

Epidote

The first ^{57}Fe NGR study of epidote [67B2] showed that Fe^{3+} preferentially occupies the distorted M3 site. This result was confirmed by neutron diffraction measurements [78N1, 88K1] as well as other ^{57}Fe NGR studies [73D1, 83P1, 88B1, 91P2, 95A1, 97F1, 01G2]. Fe^{3+} on the M1 site has not been detected in epidotes with iron content below ~ 0.75 Fe pfu [73D1, 97F1], but in iron rich epidotes, small amounts of Fe^{3+}may enter into the M1 position, where the intracrystalline exchange Al ⇔ Fe^{3+} between the M1 and M3 sites may be described by a nonconvergent ordering process [80B1].

The ^{57}Fe NGR spectrum of epidote, at room temperature - Fig. 16a - exhibits two peaks. In addition, iron rich samples (> 0.75 Fe pfu) may exhibit an inner shoulder, indicating the presence of a second Fe^{3+} doublet [01G1]. While the isomer shifts (δ = 0.36 mm/s) for both doublets are similar and characteristic for Fe^{3+}, their quadrupole splittings, ΔQ, are different. The spectra have ΔQ = 1.89…2.06 mm/s for the dominant doublet. This component has been assigned to Fe^{3+} ions in more distorted M3 site [67B2, 73D1, 80B1, 91P2, 95A1, 97F1]. Such a quadrupole splitting is unusually large for a high spin ferric iron in approximately octahedral coordination. The quadrupole splitting of the less intense doublet, in iron rich epidotes, attributed to Fe^{3+} in more regular M1 site, varies considerably between 0.80…1.00 mm/s [91P2], 0.97 mm/s [95A1], 1.33 mm/s [71D1] and 1.50…1.62 mm/s [97F1]. The different values may be attributed to uncertainties in the position of the doublet, since of the low concentration of iron in M1 site. Minor amounts of Fe^{2+} have been also observed - Table 4.

The electronic structure of Fe-rich epidotes has been analyzed by cluster molecular orbital calculations in local spin density approximation [01G1]. Calculated quadrupole splitting for Fe^{3+} at both M1 and M3 sites are in quantitative agreement with experimental values. It was concluded that a strong tetragonal compression of the

M3 octahedron may be responsible for the unusually large value of ΔQ for Fe^{3+} (M3). The corresponding electric field gradient (EFG) is dominated by the anisotropy of the valence shell of iron, whereas the ligands contribute only to about 15 % to EFG. The calculations emphasize that rather large clusters, extending beyond the second coordination sphere of iron, are necessary for a reliable description. Small clusters including only the first coordination sphere of iron generally yield misleading results due to unsaturated oxygen bond and relatively large cluster charges [91G1].

At 4.2 K, the ^{57}Fe NGR spectrum was interpreted as corresponding to three symmetric doublets resulting from quadrupole interactions [75P1]. No conclusive explanation was given for the appearance of three different sites at low temperature. Below 10 K, the character of the spectra shows a strong temperature dependence - Fig. 16b. The quadrupole doublet becomes asymmetric at about 8 K and below 4 K a well defined magnetic hyperfine structure is observed. Only one site was shown above and below the transition region [83P1]. The temperature evolution of the spectra is characteristic for the presence of relaxation of the electronic spin resulting in a time dependent hyperfine field. The high-temperature spectra result from the fast relaxation times, where the magnetic hyperfine field averages to zero. At low temperatures, the relaxation times are long in comparison with the nuclear precession time of the nuclear levels. By using a stochastic model [68B1], the spectra were analyzed [83P1]. The temperature dependence of the relaxation frequency suggests that a single relaxation process is involved, characteristic of spin-lattice interaction. The presence of the magnetic hyperfine structure at low temperatures in epidote is the result of a freezing of paramagnetic moment of Fe^{3+}. The hyperfine field is constant at 2K and 3K which eliminates the possibility that a magnetic transition occurred. Thus, the structure observed by [75P1] may be associated with the presence of paramagnetic hyperfine structure rather than the appearance of additional sites.

Chevkinite

The ^{57}Fe NGR spectra of chevkinite consist of two Fe^{2+} doublets and two Fe^{3+} doublets - Fig. 17 [92L1]. The sites occupied by the iron ions are given in Table 4 together with hyperfine parameters.

Vesuvianite

In low-Ti content vesuvianite more than 90 % of the total iron is Fe^{3+} on octahedral Al/Fe sites, but in crystals in which the TiO_2 concentration exceeds 1 wt %, most of the iron is in ferrous state [75M2] - Table 4. According to [75M2], at low iron content (< 3.5 wt %) in Ti-rich vesuvianites, ferrous ions occupy preferentially the square pyramidal 5-coordinated sites, but at higher concentrations these sites are saturated and ferrous ions then favour the octahedral Al/Fe positions. A sample having 3.65 wt % FeO and 0.95 % TiO_2 has Fe^{2+} in square pyramidal 5-coordinated site (44 %), on octahedral Al/Fe site (31 %), and Fe^{3+} on octahedral Al/Fe site (13 %), Fe^{2+} in Ca-site (1 %). Approximately 10 % of the Fe has not been assigned. Titanium ions as Ti^{4+} were reported to be predominantly on octahedral Al/Fe sites, with smaller amount in 8-coordination and possibly in 5-coordination [75M2]. Since of overlapping absorptions, accurate determinations of the hyperfine parameters were not possible [75M2].

8.1.2.7.4 Nuclear magnetic resonance (NMR) data

Zoisite

The ^{27}Al NMR spectrum of zoisite $Ca_2Al_3Si_3O_{12}(OH)$, is plotted in Fig. 18 [69B1]. The spectrum is the result of contributions from two Al unequivalent sites. The determinated parameters are given in Table 5. The high difference between the coupling constants for the two Al sites, having the same number of nearest neighbors, reflects the excessive distortion of the aluminium-oxygen octahedra at the site Al2. The directions of the maximum and intermediate field gradients, at the site Al2, are nearly parallel to the directions of the shortest and largest Al–O bond length, respectively. This suggests that in a highly distorted Al–O octahedron, the electric field gradient tensor is predominantly determined by the octahedron itself.

The second moments of the ^1H resonance line of zoisite are given in Table 5 [69B1]. A comparison with calculated values confirms the hydrogen position as determined by X-ray study, namely that hydrogen atoms occur in fourfold special position 4c – see also section 8.1.2.7.1.

Vesuvianite

The ^{27}Al NMR spectrum of a vesuvianite[103)] is plotted in Fig. 19a. Accurate isotropic chemical shifts can be obtained from satellite sidebands and are 41.1(5) ppm for the 5-coordinated site and 9.0(1.0) and 2.5(1.0) ppm for octahedrally coordinated Al and Al/Fe sites, respectively. The ^{27}Al NMR data show that some Al occupies the pentahedrally coordinated Y' site in Mg-rich vesuvianite. In addition, because the amount of Al found in the Y' site does not fill a statistically half-occupied site, the assignment of other cations (e.g. Fe in more Fe-rich vesuvianites) is also supported [87P1]. For sample[104a,b)] having high iron content it is not possible to observe well resolved satellite sideband spectra. Thus, precise chemical shift measurements is not possible [87P1]. For ^{27}Al NMR see also [96Z1].

The ^{29}Si NMR spectrum of a vesuvianite sample having low iron content[103)] consists of a broad featureless peak - Fig. 19b. This peak must contain signals from all the three silicon sites [87P1].

Danburite

The danburite $CaB_2Si_2O_8$, was analysed by ^{11}B NMR [64B1]. For each rotation along the three principal crystallographic axes, one central line and two pairs of satellites were observed. This confirms the presence of a center of symmetry in the structure, as evidenced by X-ray studies. The narrow widths of the ^{11}B central line and the satellites, and the fact that ^{11}B spectrum can be completely explained by assuming boron atoms occupying only one type of site, indicate that there is virtually no disordering of the boron atoms. The value of quadrupole coupling constant - Table 5 - falls within the range of BO_4 tetrahedra in closed-ring polyions [64B1]. The thermal experiments indicate that B-Si order persists up to the decomposition temperature (~ 1000ºC) [64B1].

8.1.2.7.5 Electron paramagnetic resonance (EPR) data

Zoisite

The EPR studies were performed on zoisite[105)] doped with VO_2^{2+}, Cr^{3+} and Fe^{3+} [71H1]. The vanadyl ion, VO_2^{2+} is formed when a V^{4+} ion is bonded to a ligand oxide ion by a strong double covalent bond. The EPR data were obtained by fitting the spectrum with the Hamiltonian $\mathbf{H} = \mu_B \boldsymbol{BgS} + \boldsymbol{IAS}$. There are four inequivalent sets of substitutional sites for vanadium. The principle axes directions and spin Hamiltonian parameters suggest that correlation can be made between these substitutional sites and the Al^{3+} sites:

Site 1: vanadium substitutes into four magnetically equivalent and symmetry related sites, the four groups of site 1 lines coalescing into pairs in the (001), (100) and (010) planes and into one group parallel to the crystal axes. The site 1 EPR spectra were attributed to the vanadyl ion VO^{2+} ($3d^1$) substituted into $Al1^{3+}$ with the V-O axis along the short bond direction of the distorted Al–O octahedra.

Site 2: Here vanadium substitutes into two magnetically equivalent and symmetry related sites. They have a common magnetic ***y***-axis parallel to ***b*** and the ***x***- and ***z***-axes 11° from ***c***- and ***a***-axes, are related by reflection in the (100) plane. The spectra were attributed to VO^{2+} substituted into $Al2^{3+}$.

Site 3: The spectra were attributed to V^{4+} ions in site Al2, the octahedral distortions determining the principle axes and values.

Site 4: At low temperatures, the spectrum revealed the presence of sites similar to site 2 with interchanged ***y***- and ***x***-axes. The differences were attributed to differing charge compensations.

The EPR data obtained analysing the spectra are given in Table 6. The EPR spectra of Cr^{3+} and Fe^{3+} were typical for ions in very distorted octahedral sites. The magnetic axis directions show that these impurities substitute into site Al2 with axes in the (010) plane, approximatelly along the bond directions for Cr^{3+} and between the bond directions for Fe^{3+}. The spectra were fitted with the Hamiltonian $\mathbf{H} = \mu_B \boldsymbol{BgS} + \frac{1}{3} DO_2^o + EO_2^2$. The determined parameters are listed in Table 6. We note that according to [71H1], the data on EPR in zoisite reported by [71T1] were misinterpreted.

Vesuvianite

A typical spectrum of vesuvianite[106)] (see Table 3 for composition) is shown in Fig. 20 [92D2]. An asymmetrical signal of axial symmetry shows a well pronounced hyperfine structure (HFS) in parallel region, but the perpendicular HFS remained completely unresolved. The spectrum was described by the Hamiltonian $\mathbf{H} = \mu_B[g_{\|}B_zS_z + g_{\perp}(B_xS_x + B_yS_y)] + A_{\|}S_zI_z + A_{\perp}(S_xI_x + S_yI_y)$. The computed spectrum with parameters given in Table 6 describes well the experimental one - Fig. 20. The nature of chemical bonding of copper in the crystal lattice was determined. The Cu^{2+}-O bonding has a noticeable covalent contribution and the electron density is delocalized over both the copper and the oxygen orbitals.

An EPR study of Fe-rich vesuvianite shows that a prevailing part of Fe^{3+} is located at the Y' site [95R1].

8.1.2.7.6 Dielectric properties

The dielectric constants for some silicates are given in Table 7. The dielectric polarizabilities calculated with the Clausius-Mossotti relation differ for epidote and zoisite with 10.1 % and 11.7 %, respectively [92S1].

For dielectric constants see also [81O1].

8.1.2.7.7 Heat capacity

$Mg_5Al_5Si_6O_{21}(OH)_7$, Mg-sursassite

The temperature dependence of the specific heat for $T > 50$ºC is plotted in Fig. 21 [01G1]. According to [01G1], the heat capacity over the entire studied temperature range can be expressed by a four term equation [85B1]: $C_p = 1571.104 - 10560.89\ T^{-0.5} - 26217890.0\ T^{-2} + 1798861000.0\ T^{-3}$ $JK^{-1}\ mol^{-1}$, where T is in K.

8.1.2.7.8 EXAFS and XANES data

Epidote

The L_{III} extended X-ray absorption fine structure (EXAFS) spectra of R = Gd, Er and Lu was used to analyse their local environment in synthetic epidotes on compositions $CaLa_{0.9}R_{0.1}Al_2MgSi_3O_{13}H$ [88C1]. The Fourier transforms of the Gd-, Er- and Lu-EXAFS are different from one another. Three different sites are involved in the accommodation of the R ions in the epidote structure. The site preference is a function of the rare-earth ionic size. Gd is located in A2-type sites, whereas the atomic environment of Er is consistent with the A1 site occupancy and the Lu environment has been modelled on an M3-type octahedral site - Table 8 [88C1].

We note that by X-ray studies has been shown that La^{3+} and Ce^{3+} ions having larger ionic radius than Ca^{2+} enter only the Ca (A2) sites [71D1]. In addition, it was also shown later that the larger R ions are preferentially positioned in the epidote structure relative to R having smaller ionic size [81B1].

Epidote, clinozoisite, vesuvianite

The silicon K-edge X-ray absorption near-edge structure (XANES) spectra of epidote, clinozoisite and vesuvianite have been measured using synchroton radiation [95L1]. The peak assigned to the transition of Si 1s electrons to the antibonding 3p-like state (Si-K edge) is very strong and located at 1846.3(1) eV, 1846.3(1) eV and 1845.9 eV in epidote[107)], clinozoisite[108)] and vesuvianite[109)] , respectively. The analysis by XANES method of a large number of silicates [95L1] show that the Si K-edge shifts to higher energy with increasing polymerization of SiO_4^{4-} clusters. The substitution of Al for Si in tetrahedral sites shifts the Si K-edge to lower energy.

8.1.2.7.9 Optical properties

Epidote, zoisite, clinozoisite

Infrared absorption spectra between 4000 and 400 cm^{-1} on natural zoisite and epidote have been analyzed [62M1]. These spectra differ mainly in the low energy part (< 500 cm^{-1}), thus providing the possibility of

distinguishing between orthorhombic and monoclinic polymorphs of zoisites and epidotes. In [64S1] absorption spectra between 4000 and 650 cm^{-1} of $Ca_2(Al_{1-x}Fe^{3+}_x)Al_2O(OH)(SiO_4)[Si_2O_7]$ were measured with x = 0.55 ÷ 0.85 and it was concluded that the spectra obtained were nearly identical. In the range 1102…884 cm^{-1} there is a slight shift when increasing the iron content. In [70L1] a band at 3160 cm^{-1} was assigned to the stretching vibration of the hydrogen bridge and the orientation of the OH dipole parallel to the crystallographic ***c***-axis was confirmed. A detailed analysis of the IR absorption spectra in the range 5000 to 250 cm^{-1} of epidotes ($0.00 < x < 0.89$), zoisites and clinozoisites ($0.00 < x < 0.11$) has been made by [74L1]. From their IR-spectra, both polymorphs can be distinguished by the position of the main OH-valence vibration (3260 cm^{-1} for zoisite, clinozoisite (x = 0) - epidote (x = 0.89): 3326…3365 cm^{-1}), by a band at 2160 cm^{-1} present only in zoisite and by different band shapes in the range 820…700 cm^{-1} and 540…320 cm^{-1}. Appreciable shifts of the above bands were found to be a function of Fe^{3+} content. These shifts can be represented by the linear relation $\tilde{\nu} = A(x=0) + Bx$ where A and B are (3325.8 cm^{-1}; 48.3 cm^{-1}); (1045.6 cm^{-1}; –12.4 cm^{-1}); (741.7 cm^{-1} ; –25.7 cm^{-1}); (419.4 cm^{-1}; –27.2 cm^{-1}); (364.2 cm^{-1}; –13.2 cm^{-1}). The deuteration experiments showed that the band at 2160 cm^{-1} is also connected to a hydrogen bond and related it to the stretching vibration of a second unusually strong, unspecified hydrogen bridge [74L1, 80L1]. In [89W1] the influence of pressure on the OH-stretching vibration of zoisite single crystals was studied by high-pressure infrared spectroscopy. The band related to the OH-stretching vibration displayed a linear shift from 3170 cm^{-1} at 1 bar to 2795 cm^{-1} at 116 kbar. The half-band width increased linearly with respect to pressure from 60 cm^{-1} at 1 bar to 500 cm^{-1} at 116 kbar. The strength of the absorption of this band is strongly frequency dependent. The high-energy shift of the band at around 2200 cm^{-1} on pressure increase indicates that this band is not due to a second order OH-stretching vibration as suggested by [80L1].

Piemontite

The polarized electronic absorption spectra of $Ca_2(Al_{3-x}Mn^{3+}_x)[OH|O|SiO_4|Si_2O_7]$ piemontites for ***E*** ∥ ***X***, ***E*** ∥ ***Y*** and ***E*** ∥ ***Z*** in the spectral range 35000…5000 cm^{-1} are given in Fig. 22a [02L1]. The crystallographic orientations of the optical indicatrix axes ***X***, ***Y***, ***Z*** are given in Fig. 3. The spectra are dominated by three strongly polarized absorption bands ν_1 at 12000…13000 cm^{-1} (***E*** ∥ ***Y***), ν_2 at 18000…19000 cm^{-1} (***E*** ∥ ***Y*** and ***Z***, ***Z*** > ***Y***) and ν_3 at 22000…24000 cm^{-1} (***E*** ∥ ***X***). These bands are typical spin allowed dd transitions of Mn^{3+} in M3 octahedra of the piemontite structure [67B3, 76L2, 82S1]. These three bands shift slightly to lower energies on increasing the M3 site fraction of Mn^{3+} ($x_{Mn^{3+}}$ (M3)). The polarization behaviour was interpreted by assuming a $C_{2v}(C_2")$ pseudo-symmetry of the M3 sites, a super-group of their site symmetry C_s. Evaluation of the energies of ν_1, ν_2 and ν_3 on the basis of the energy level diagram for Mn^{3+} - Fig. 22b - with the above pseudosymmetry yields the crystal field parameter $10Dq$ = 13540 cm^{-1} for $x_{Mn^{3+}}$ (M3) = 0.931. The $10Dq$ values increase slightly by 30 cm^{-1} per $-0.1\, x_{Mn^{3+}}$ (M3). Such values and the Jahn-Teller splitting of the octahedral crystal field ground state of Mn^{3+}, $\delta = \nu_1$, yield a crystal field stabilization energy (CFSE) of Mn^{3+} (M3) of 14080 cm^{-1} for $x_{Mn^{3+}}$ (M3) = 0.931. The CFSE increases slightly by 28 cm^{-1} per $-0.10\, x_{Mn^{3+}}$ (M3).

In [02L1] was stated that no clear decision can be made for the spin allowed dd bands of Mn^{3+} in the compressed M1 octahedra of the clinozoisite type although about half of these polyhedra in the most Mn^{3+}-rich synthetic piemontites are occupied by Mn^{3+}. The reasons are strong band overlap in the complex spectra and low intensities of the Mn^{3+}(M1)-bands due to the centrosymmetry of the M1 site. Presumably, two bands at ≅ 20000 cm^{-1} (broad ***E*** ∥ ***Y*** and ***Z***) and at 21590…21870 cm^{-1} (narrow ***E*** ∥ ***Z*** > ***Y***) are the ν_2 and ν_3 band of Mn^{3+} and they strongly gain intensity on increasing the Mn^{3+}(M1) site fraction.

In [02L1], one of the natural piemontites was shown to contain Mn^{2+} substituting for about 10 % of the Ca in A1, A2 sites. In this case no Mn^{2+} - Mn^{3+} charge transfer band, which should be strongly polarized parallel to ***c*** (i.e. closely parallel to ***X*** direction) could be identified with certainty in the optical absorption spectrum.

Vesuvianite

Optical spectroscopic investigations on vesuvianites [75M1, 75M2, 76M1, 77M1, 92D1, 95P1] have shown that these studies may be useful in solving the question of $3d^n$ ions site population. The absorption spectra were described by envelopes at 9000 cm^{-1} and 12000 cm^{-1} and a prominent peak at 11000 cm^{-1} [75M2] - Fig. 23. The 11000 cm^{-1} band was assigned to $Fe^{2+} \rightarrow Fe^{3+}$ charge transfer between ions on Al/Fe and Ca3 sites. This band is missing from some natural vesuvianites. The 9000 cm^{-1} band was considered as determined by octahedrally bonded Fe^{2+} ions. The component at 12200 cm^{-1} may arises from 5-coordinated Fe^{2+}. Bands caused by $Fe^{2+} \rightarrow Ti^{4+}$ charge transfer process have been observed at 23000 cm^{-1} and 26750 cm^{-1} [75M1].

In the Cu-bearing vesuvianite [106], the $\boldsymbol{E} \perp \boldsymbol{c}$ optical absorption spectrum shows an intense absorption band at 15600 cm^{-1} (640 nm) and a weak band at 12500 cm^{-1} (800 nm). In the $\boldsymbol{E} \parallel \boldsymbol{c}$ spectrum there is a distinct band at 16700 cm^{-1} (600 nm) and a very weak broad band close to 12500 cm^{-1} - Fig. 24a [92D2]. The colour of the sample is determined by the 15600 cm^{-1} and 16700 cm^{-1} band. The optical absorption spectrum can be best explained assuming that Cu^{2+} ions occupy irregular fivefold sites. Thus, the most intense absorption band in the $\boldsymbol{E} \perp \boldsymbol{c}$ spectrum, at 15600 cm^{-1}, corresponds to the electronic transition $^2B_{1g} \rightarrow E_g$ while the 12500 cm^{-1} band corresponds to the transition $^2B_{1g} \rightarrow {}^2B_{2g}$ - Fig. 24b. In the $\boldsymbol{E} \perp \boldsymbol{c}$ spectrum, the absorption band at 16700 cm^{-1} was attributed to the transition $^2B_{1g} \rightarrow {}^2A_{1g}$ [92D2].

In the near IR range very weak and narrow absorption bands connected with the OH overtones were detected at 7800, 7550 and 7050 cm^{-1} [92D2].

The absorption spectra in the natural sample[110] (lilac) show an intense broad band at 18500 cm^{-1} in the $\boldsymbol{E} \perp \boldsymbol{c}$ polarization and weak bands at 23100 cm^{-1}, 18500 cm^{-1} and 12500 cm^{-1} in the $\boldsymbol{E} \parallel \boldsymbol{c}$ polarization - Fig. 25a [95P1]. The spectra of versuvianite[111] (yellow) have a strong $\boldsymbol{E} \perp \boldsymbol{c}$ polarized band near 23600 cm^{-1} and weak bands at 23900 cm^{-1}, 22700 cm^{-1} and 20100 cm^{-1} in the $\boldsymbol{E} \parallel \boldsymbol{c}$ polarization - Fig. 25b [95P1]. It was concluded that the spectra of vesuviante[111] (yellow) are due to Mn^{3+} ions occupying the fivefold-coordinated Y'(B)-site (C_{4v} - 4mm) symmetry. The dominating absorption band at 23600 cm^{-1} was assigned to the only symmetry allowed transitions $^5B_1 \rightarrow {}^5E$ in Mn^{3+} ions. The spectra of vesuvianite[110] (lilac) were assigned to Mn^{3+} ions in the distorted Al/Fe octahedra and also in Y'(B) sites which have different Y'- O10 distances.

The IR absorption spectra in the OH stretching region show some differences in positions and intensities of absorption bands. In the spectrum of vesuvianite[111] - Fig. 25d - a rather strong and sharp band at 3172 cm^{-1} appears, while in vesuvianite[110] this band is weak and broad (Fig. 25c). Since the character of the band near 3200 cm^{-1} reflects the state of ordering and temperature of formation [92A1], it was supposed that sample[110] represents a less ordered and a higher temperature variety in comparison with vesuvianite[111] [95P1].

Danburite

The non-polarized IR spectrum of a (100) crystal plate of danburite shows one very sharp absorption band at 3540 cm^{-1} [87B1]. Using polarized IR radiation, strong pleochromism of this band was observed. The absorption band at 3540 cm^{-1} has a maximum absorption when the polarized radiation vibrates parallel to [010] in both (100) and (001) sections. This requires an orientation of the OH dipole parallel to the ***b***-axis ([010]).

For refractive indices see Table 9.

Tables and figures

Table 1. Silicate minerals from groups VIIIB15 – VIIIB19 [91N1].

Silicate	Ideal composition	Group
Epidote	$Ca_2FeAl_2(Si_2O_7)(SiO_4)(O,OH)_2$	VIIIB15
Zoisite	$Ca_2Al_3(Si_2O_7)(SiO_4)(O,OH)_2$	VIIIB15
Clinozoisite	$Ca_2Al_3(Si_2O_7)(SiO_4)(O,OH)_2$	VIIIB15
Piemontite	$Ca_2(Mn,Fe)Al_2(Si_2O_7)(SiO_4)(O,OH)_2$	VIIIB15
Hancockite	$CaPbAl_3(Si_2O_7)(SiO_4)(O,OH)_2$	VIIIB15
Mukhinite	$Ca_2Al_2VSi_3O_{12}(OH)$	VIIIB15
Allanite-(La)	$(La,Ca)_2(Al,Fe)_3(SiO_4)_3(OH)$	VIIIB15
Allanite-(Ce)	$Ca(Ce,La)(Al,Fe)_3(SiO_4)_3(OH)$	VIIIB15
Allanite-(Y)	$Ca(Y,La,Ce)(Al,Fe)_3(SiO_4)_3(OH)$	VIIIB15
Dissakisite-(Ce)	$CaCe(MgAl_2)(SiO_4)_3(OH)$	91G1
Dollaseite-(Ce)	$Ca(Ce,La,Nd)Mg_2AlSi_3O_{11}(OH)F$	VIIIB15
Chevkinite-(Ce)	$(Ce,La)_4(Ti,Fe)_5O_8(Si_2O_7)_2$	VIIIB16
Strontio-chevkinite	$(Sr,Ce,La)_4Fe(Ti,Zr)_4O_8(Si_2O_7)_2$	VIIIB16
Perrierite	$(Ca,Ce,Th)_4(Mg,Fe)_2(Ti,Fe)_3O_8(Si_2O_7)_2$	VIIIB16
Karnasurtite-(Ce)	$(Ca,La,Th)(Ti,Nb)AlSi_2O_7(OH)_4\cdot 3H_2O$	VIIIB16
Vesuvianite	$Ca_{19}Fe(Mg,Al)_8Al_4(SiO_4)_{10}(Si_2O_7)_4(OH)_{10}$	VIIIB17
Wiluite	$Ca_{19}Fe(Al,Mg,Fe,Ti)_{13}(B,Al)_5Si_8O_{68}(O,OH)_{10}$	98G1
Danburite	$CaB_2Si_2O_8$	VIIIB18
Macfallite	$Ca_2Mn_3(SiO_4)(Si_2O_7)(OH)_3$	VIIIB19
Sursassite	$Mn_2Al_3(SiO_4)(Si_2O_7)(OH)_3$	VIIIB19
Mg-sursassite	$Mg_5Al_5Si_6O_{21}(OH)_7$	00G1
Orientite	$Ca_2Mn_3Si_3O_{10}(OH)_4$	VIIIB19
Ruizite	$Ca_2Mn_2Si_4O_{11}(OH)_4\cdot 2H_2O$	VIIIB19
Kittatinnyite	$Ca_2Mn_2Si_2O_8(OH)_4\cdot 9H_2O$	VIIIB19
Ardennite	$Mg_{1+x}Mn_4Al_{5-x}(AsO_4)(SiO_4)_2(Si_3O_{10})(OH)_6$	VIIIB19

Table 2. Atomic coordinates and isotropic temperature factors.

(a) Epidote[1)] having monoclinic-type structure, space group $P2_1/m$ [71D1].

Atom	*x*	*y*	*z*	B_{eq} [Å^2]
A1	0.7562(2)	0.75	0.1510(2)	0.76
A2	0.6042(2)	0.75	0.4241(2)	0.92
Si1	0.3396(3)	0.75	0.0473(2)	0.41(4)
Si2	0.6851(3)	0.25	0.2744(2)	0.48(4)
Si3	0.1844(3)	0.75	0.3189(2)	0.42(4)
M1	0	0	0	0.51(6)
M2	0	0	0.5	0.43(7)
M3	0.2946(2)	0.25	0.2245(1)	0.42
O1	0.2339(5)	0.9923(11)	0.0410(4)	0.70(7)
O2	0.3040(4)	0.9809(10)	0.3554(4)	0.63(7)
O3	0.7957(5)	0.0152(11)	0.3382(4)	0.79(7)
O4	0.0528(7)	0.25	0.1294(6)	0.6(1)
O5	0.0417(7)	0.75	0.1471(6)	0.6(1)
O6	0.0683(7)	0.75	0.4078(6)	0.5(1)
O7	0.5164(7)	0.75	0.1825(6)	0.6(1)
O8	0.5281(7)	0.25	0.3099(6)	0.9(1)
O9	0.6265(7)	0.25	0.0990(7)	1.0(1)
O10	0.0838(7)	0.25	0.4298(6)	0.7(1)

[1)] for composition see footnote in Table 3.

b) Synthetic perrierite, $Mg_4La_8Ti_6Si_8O_{44}$, having space group $P2_1/a$ [74C1].

Atom	*x*	*y*	*z*	B [Å^2] · 10^4
La1	0.23756(5)	0.0198(1)	0.26687(6)	78(3)
La2	0.04897(5)	0.0265(1)	0.7432(6)	87(3)
Si1	0.4123(2)	–0.0001(5)	0.7322(3)	57(6)
Si2	0.1624(2)	0.0027(5)	0.5489(3)	69(6)
O1	0.0794(6)	–0.2597(14)	0.1864(7)	91(14)
O11	0.0652(6)	0.2556(14)	0.1858(7)	103(14)
O2	0.2899(6)	0.2606(15)	0.1229(7)	128(15)
O21	0.2875(6)	–0.2401(14)	0.1225(7)	105(15)
O3	0.3736(6)	–0.2511(14)	0.4058(7)	123(15)
O31	0.3920(6)	0.2862(15)	0.4066(8)	139(15)
O4	0.0957(7)	0.0077(14)	0.9894(8)	114(15)
O5	0.4067(7)	–0.0041(14)	0.0089(8)	110(15)
O6	0.4932(7)	0.0328(15)	0.6667(8)	150(16)
O7	0.2884(7)	–0.0337(16)	0.6366(8)	176(17)
O8	0.1384(6)	–0.0036(14)	0.4042(7)	115(15)
Mg	0	1/2	1/2	47(9)
C1[1)]	–0.0039(2)	0.2385(6)	0.0004(3)	105(6)
C2[1)]	0.2749(2)	0.0071(4)	0.017(2)	68(4)

[1)] Site C1 contains 0.616(6) Ti and 0.384 Mg and C2 contains 0.884 Ti and 0.116 Mg. All atoms are in sites of type 4e except Mg which lies in a site of type 2c.

Table 2 (continued)

c) Mg-chevkinite, $Mg_4Nd_8Ti_6Si_8O_{44}$, having space group $P2_1/a$ [74C1].

Atom	*x*	*y*	*z*	B [Å^2] · 10^4
Nd1	0.35442(4)	0.02260(7)	0.23312(4)	95(1)
Nd2	0.07127(4)	–0.03662(7)	0.24017(4)	94(2)
Si1	0.2015(2)	0.4972(3)	0.2306(2)	69(4)
Si2	0.3596(2)	0.5019(3)	0.0470(2)	76(4)
O1	0.2393(5)	–0.2098(9)	0.3133(5)	75(10)
O11	0.2170(5)	0.2527(9)	0.3130(5)	81(10)
O2	–0.0247(5)	–0.2527(9)	0.3742(5)	85(10)
O21	–0.0214(5)	0.2448(10)	0.3736(5)	93(10)
O3	0.4131(5)	–0.2493(10)	0.0946(5)	93(10)
O31	0.4437(5)	0.2947(10)	0.0931(5)	107(11)
O4	0.1457(6)	–0.0104(10)	0.4757(5)	106(11)
O5	0.1511(6)	0.5044(10)	0.5099(5)	105(11)
O6	0.0866(6)	0.5469(10)	0.1686(5)	113(11)
O7	0.2741(6)	0.4477(10)	0.1307(6)	151(12)
O8	0.3132(6)	0.4892(9)	0.0985(5)	74(10)
Mg[1)]	0	1/2	0	78(7)
C1[1)]	0.2434(2)	0.2466(3)	0.5000(2)	82(3)
C2A[1)]	0	1/2	1/2	111(5)
C2B[1)]	1/2	1/2	1/2	93(4)

[1)] Mg, C2A and C2B lie in sites 2d, 2b and 2b, respectively. C2A contains 0.807(7) Ti and C2B contains 0.834(9) Ti with the remainder being Mg. Site C1 contains 0.680 Ti and 0.320 Mg.

d) Vesuvianite[75)] having space group P4nc [00A1].

Atom	*x*	*y*	*z*	B [Å^2]
Si1	1/2	0	0.0002(2)	0.66(2)[f)]
Si2a	0.56994(8)	0.20863(8)	–0.1293(1)	0.53(1)[f)]
Si2b	–0.70928(8)	0.06815(8)	0.1292(1)	0.53(1)[f)]
Si3a	0.40063(8)	0.33032(8)	–0.6340(1)	0.55(1)[f)]
Si3b	0.33580(8)	0.40100(9)	0.1360(1)	0.55(1)[f)]
Al1	0.2502(1)	0.2482(1)	0.5008(2)	0.61(1)
Al2a	0.36212(9)	0.12802(9)	–0.6263(2)	0.57(1)
Al2b	–0.36191(9)	0.13014(9)	0.1269(2)	0.57(1)
Ca1[a)]	1/2	0	0.2507(2)	0.80(2)
Ca2a	0.43951(7)	0.20435(7)	0.12082(8)	0.740(8)
Ca2b	–0.43939(6)	0.20737(7)	–0.62028(9)	0.740(8)
Ca3a	–0.56939(7)	0.35056(7)	–0.1111(1)	1.137(8)
Ca3b	0.85241(7)	0.06941(7)	0.1081(1)	1.137(8)
O1a	0.5320(2)	0.0779(2)	0.0860(3)	0.67(2)
O1b	–0.5320(7)	0.0777(2)	–0.5853(3)	0.67(2)
O2a	0.5927(2)	0.1325(2)	–0.2215(4)	0.73(2)
O2b	–0.6336(2)	0.0891(2)	0.2233(3)	0.73(2)
O3a	0.4720(2)	0.2003(2)	–0.0772(3)	0.67(2)

Table 2 (continued)

Atom	*x*	*y*	*z*	*B* [Å^2]
O3b	–0.4705(2)	0.2006(2)	–0.4229(3)	0.67(2)
O4a	0.6884(2)	0.1439(2)	–0.5280(3)	0.64(2)
O4b	–0.6866(2)	0.1422(2)	0.0299(3)	0.64(2)
O5a	–0.4208(2)	0.2368(2)	0.1776(3)	0.75(2)
O5b	0.4187(2)	0.2322(2)	–0.6783(3)	0.75(2)
O6a	0.5222(2)	0.3727(2)	0.0573(3)	1.04(3)
O6b	–0.5209(2)	0.3647(2)	–0.5596(3)	1.04(3)
O7a	0.1938(2)	0.0770(2)	0.1782(3)	1.10(3)
O7b	–0.6939(2)	–0.5776(2)	–0.1785(3)	1.10(3)
O8a	0.6603(2)	0.3110(2)	–0.5663(3)	0.68(2)
O8b	–0.6578(2)	0.3099(2)	0.0664(3)	0.68(2)
O9	0.3953(3)	0.3939(3)	0.2524(3)	0.80(3)
O10b	0	0	0.1336(3)	1.20(4)
H10b	0	0	0.220(4)	2.37[f]
O10a	0	0	–0.6373(3)	1.20(4)
O11a	0.2553(2)	0.1866(2)	–0.6346(3)	0.64(2)
H11a	0.211(3)	0.191(3)	–0.706(4)	2.37[f]
O11b	–0.2555(2)	0.1887(2)	0.1376(3)	0.64(2)
H11b	–0.259(3)	0.220(3)	0.201(4)	2.37[f]
Y'3a[b]	1/2	1/2	0.0605(1)	0.60(2)
X'4a[c]	1/2	1/2	0.3522(2)	0.97(3)
Y'3b[d]	0	0	–0.048(1)	0.39[f]
X'4b[e]	1/2	1/2	0.148(1)	0.98[f]

[a] 0.88Ca+0.12Na; [b] 0.852(5)(Mn+Cu); [c] 0.852(5)Ca; [d] 0.148(5)(Mg+Na); [e] 0.148(5)Ca;
[f] atoms refined isotropically;
[75] for compositon see footnote in Table 3.

e) Vesuvianite[76] having space group P4/n (origin at $\bar{1}$) [00A1].

Atom	*x*	*y*	*z*	B_{eq} [Å^2]
Si1a	–1/4	1/4	0	0.53(3)
Si1b	–1/4	1/4	1/2	0.67(3)
Si2a	–0.0404(1)	0.3187(1)	0.1300(1)	0.55(2)
Si2b	–0.0417(1)	0.1801(1)	0.3727(1)	0.48(3)
Si3a	0.08662(9)	0.3490(1)	–0.1339(1)	0.56(2)
Si3b	0.0804(1)	0.15049(9)	0.6367(1)	0.53(2)
Al1a	0	0	0	0.55(4)
Al1b	–1/2	0	1/2	0.48(4)
Al2a[a]	–0.1135(1)	0.1201(1)	0.1254(1)	0.62(3)
Al2b	–0.3887(1)	0.1225(1)	0.3733(1)	0.51(3)
Ca1	–1/4	1/4	0.2501(1)	0.63(1)
Ca2a	–0.04524(8)	0.18824(8)	–0.11935(8)	0.64(2)
Ca2b	0.19023(8)	–0.04298(8)	0.62120(8)	0.65(2)
Ca3a	0.09914(8)	0.17886(8)	0.12047(8)	1.02(2)
Ca3b	–0.39629(8)	–0.18512(8)	–0.39542(8)	0.98(2)
O1a	–0.2213(2)	0.1723(2)	0.0863(3)	0.61(6)

Table 2 (continued)

Atom	*x*	*y*	*z*	B_{eq} [Å^2]
O1b	–0.2816(2)	0.1724(2)	0.4144(3)	0.70(6)
O2a	–0.1173(3)	0.3386(3)	0.2235(3)	0.62(6)
O2b	–0.1175(3)	0.1581(2)	0.2813(3)	0.79(6)
O3a	–0.0478(2)	0.2216(2)	0.0762(3)	0.66(6)
O3b	–0.0489(2)	0.2775(2)	0.4246(3)	0.68(6)
O4a	–0.0618(2)	0.3936(2)	0.0324(3)	0.66(6)
O4b	–0.0624(2)	0.1062(2)	0.4723(3)	0.66(6)
O5a	–0.0107(2)	0.3274(2)	–0.1768(3)	0.91(6)
O5b	–0.0178(2)	0.1682(2)	0.6801(3)	0.73(6)
O6a	0.1249(2)	0.2720(2)	–0.0570(3)	1.02(6)
O6b	0.1146(2)	0.2284(2)	0.5621(3)	0.96(6)
O7a	0.0559(2)	0.3255(2)	0.1824(3)	0.91(6)
O7b	0.0556(2)	0.1708(2)	0.3266(3)	0.82(6)
O8a	0.0924(2)	0.4389(2)	–0.0647(3)	0.67(7)
O8b	0.0899(2)	0.0609(2)	0.5687(3)	0.76(6)
O9	0.1484(8)	0.3585(8)	–0.2495(3)	0.77(7)
O10a	1/4	1/4	0.1265(5)	0.92(9)
O10b	–1/4	–1/4	–0.3579(6)	1.3(1)
O11a	–0.0046(2)	0.0603(7)	0.1361(0)	0.84(6)
H11a	–0.018(3)	0.027(3)	0.203(4)	2.37 [f]
O11b	–0.4954(2)	0.0627(2)	0.3659(3)	0.81(6)
H11b	–0.528(3)	0.054(4)	0.3162(4)	2.37[f]
X'4a[b]	1/4	1/4	0.6507(2)	0.73(3)
Y'3a[c]	1/4	1/4	–0.0329(2)	0.69(3)
X'4b[d]	1/4	1/4	–0.149(1)	0.79[f]
Y'3b[e]	1/4	1/4	0.5388(8)	0.79 [f]

[a] 0.5Mg+0.5Al; [b] 0.840(7)Ca; [c] 0.840(7)(Fe+Ti+Mn); [d] 0.160(7)Ca; [e] 0.160(7)(Fe+Ti+Mn); [f] atoms refined isotropically.;
[76] for composition see footnote in Table 3.

f) Danburite, $CaB_2Si_2O_8$, having orthorhombic structure, space group Pnma [92D1].

Atom	*x*	*y*	*z*	$\beta_{ij} \cdot 10^4$					
				β_{11}	β_{22}	β_{33}	β_{12}	β_{13}	β_{23}
Ca	0.38555(3)	0.07653(2)	0.25	74.9(6)	64.8(6)	67.5(6)	–1.8(6)	0	0
B	0.25898(9)	0.41935(10)	0.42074(10)	43(2)	53(2)	52(2)	–2(2)	–0(2)	1(2)
Si	0.05330(2)	0.19256(2)	–0.05584(3)	39.9(6)	38.4(6)	36.3(6)	–0.6(3)	0.1(5)	–6(6)
O1	0.19282(10)	0.06781(10)	–0.00332(11)	75(2)	49(2)	92(2)	25(2)	–22(2)	–15(2)
O2	0.12650(10)	0.36484(9)	–0.04248(10)	66(2)	44(2)	72(2)	–17(2)	–20(2)	5(2)
O3	0.39967(9)	0.31355(10)	0.07837(9)	50(2)	67(2)	57(2)	11(2)	13(2)	10(2)
O4	0.51380(16)	0.66360(16)	0.25	96(3)	96(4)	31(3)	23(3)	0	0
O5	0.18391(14)	0.42812(17)	0.25	51(3)	120(4)	42(3)	17(3)	0	0

Table 2 (continued)

g) Ruizite[88] having monoclinic structure, space group C2/m [85M1].

Atom	Equipoint rank	*x*	*y*	*z*
Mn	4	0.2500	0.2500	0.000
Ca	4	0.2054(2)	0.5000	0.2599(1)
Si1	4	0.0355(2)	0.0000	0.1513(2)
O1	8	0.1328(4)	0.2165(6)	0.1291(3)
O2	4	0.3748(6)	0.5000	0.0921(5)
O3	4	–0.0063(6)	0.0000	0.2857(4)
Si2	4	0.1042(2)	0.0000	0.3951(2)
O4	8	0.2056(8)	0.2150(9)	0.3954(5)
O5	2	0.0000	0.0000	0.5000
O6	4	0.3674(6)	0.0000	0.0459(5)
O7	4	0.4437(8)	0.0000	0.2781(7)

O4 = $O^{2-}_{1/2} + OH^{-}_{1/2}$; O6 = OH^{-}; O7 = H_2O.

[88] for composition see footnote in Table 3.

h) Orientite[89] having orthorhombic structure, space group Pcmm [86M1].

Atom	*x*	*y*	*z*	B_{eq} [Å^2]	Site occupancy	Site multiplicity
Ca1	0.2876	1/2	0.1608(4)	0.39(11)	1.0	0.5
Ca2	0.8136(7)	0	0.1569(4)	0.75(12)	1.0	0.5
Ca3	0.7093(8)	1/2	0.6571(4)	1.38(13)	1.0	0.5
Ca4	0.1836(7)	0	0.6578(4)	0.36(11)	1.0	0.5
Mn1	0.2560(3)	0.2511(6)	0.0018(2)	0.19(5)	1.0	1.0
Mn2	0.5507(5)	0.2488(11)	1/4	0.06	0.84	0.5
Mn3	0.7511(3)	0.2591(7)	–0.0028(2)	0.47(6)	1.0	1.0
Si1	–0.0256(11)	1/2	0.0934(6)	1.12(17)	1.0	0.5
Si2	0.4763(9)	0	0.1006(5)	0.06	1.0	0.5
Si3	–0.1026(16)	1/2	1/4	0.06	0.84	0.25
Si4	0.1949(14)	0	1/4	0.37(20)	0.84	0.25
Si5	0.0454(9)	1/2	0.5963(4)	0.06	1.0	0.5
Si6	0.5258(9)	0	0.5971(5)	0.25(14)	1.0	0.5
Si7	0.1197(11)	1/2	3/4	0.42(16)	1.0	0.25
Si8	0.6029(40)	0	3/4	4.38(79)	0.68	0.25
Mn2A	0.0691(40)	0.2295(79)	1/4	1.41(67)	0.16	0.5
Si3A	0.3929(82)	0	1/4	0.06	0.16	0.25
Si4A	0.6936(72)	1/2	1/4	0.06	0.16	0.25
Mn2B	0.4615(15)	0.2534(31)	3/4	0.49(23)	0.32	0.5
Si4B	0.7956(42)	0	3/4	1.00(63)	0.32	0.25
O1	0.3788(15)	0.2143(27)	0.0791(8)	0.62(26)	1.0	1.0
O2	0.8691(14)	0.2886(24)	0.0781(7)	0.30(24)	1.0	1.0
O3	0.1394(26)	1/2	0.0616(13)	1.25(42)	1.0	0.5
O4	0.6301(21)	0	0.0579(11)	0.06	1.0	0.5
O5	0.2932(25)	0.2383(53)	1/4	1.64(42)	1.0	0.5

Table 2 (continued)

Atom	*x*	*y*	*z*	B_{eq} [Å^2]	Site occupancy	Site multiplicity
O6	0.7910(22)	0.2840(40)	1/4	0.74(38)	1.0	0.5
O7	0.5599(23)	0	0.1779(11)	0.36(37)	1.0	0.5
O8	0.0110(26)	1/2	0.1810(13)	1.02(44)	1.0	0.5
O9	0.0694(28)	0	0.1799(14)	1.62(48)	1.0	0.5
O10	0.1301(23)	0	0.0247(11)	0.56(36)	1.0	0.5
O11	0.6409(21)	1/2	0.0292(11)	0.06	1.0	0.5
O12	0.5284(31)	1/2	0.1806(16)	2.14(55)	1.0	0.5
O13	0.6270(13)	0.2137(25)	0.5877(7)	0.19(23)	1.0	1.0
O14	0.1289(16)	0.2615(33)	0.5807(8)	1.07(27)	1.0	1.0
O15	–0.1165(25)	1/2	0.5604(13)	1.08(43)	1.0	0.5
O16	0.3778(22)	0	0.5515(12)	0.42(36)	1.0	0.5
O17	0.1954(23)	0.2537(48)	3/4	0.93(38)	1.0	0.5
O18	0.4813(22)	0	0.6834(11)	0.06	1.0	0.5
O19	0.0060(22)	1/2	0.6768(11)	0.40(37)	1.0	0.5
O20	0.8617(20)	0	0.5410(11)	0.06	1.0	0.5
O21	0.3773(26)	1/2	0.5268(13)	1.10(45)	1.0	0.5
O22	0.7054(20)	0.2104(35)	3/4	0.05(34)	1.0	0.5
O23	–0.0782(29)	0	0.6799(15)	2.01(43)	1.0	0.5
O24	0.4300(25)	1/2	0.6771(13)	0.72(42)	1.0	0.5

[89] for composition see footnote in Table 3

i) Macfallite[81] having monoclinic-type structure, space group $P2_1/m$ [85M1].

Atom	Equipoint rank	*x*	*y*	*z*	B_{eq} [Å^2]
Mn1[a]	2	0.0000	0.0000	0.0000	1.80(6)
Mn2	2	0.5000	0.0000	0.0000	2.36(4)
Mn3	2	0.0000	0.0000	0.5000	2.29(4)
Ca1	2	0.6817(4)	0.2500	0.7954(5)	2.85(6)
Ca2	2	0.3128(4)	0.2500	0.6687(5)	2.93(6)
Si1	2	0.8107(5)	0.2500	0.1905(6)	1.79(7)
O1	2	0.6519(13)	0.2500	0.0560(15)	1.98(18)
O2	2	0.9045(15)	0.2500	0.0778(16)	2.63(22)
O6	4	0.8387(9)	0.0332(14)	0.3060(10)	2.25(13)
Si2	2	0.1956(5)	0.2500	0.2929(6)	1.76(7)
O3	2	0.1234(14)	0.2500	0.4279(14)	2.17(18)
O4	2	0.3648(13)	0.2500	0.3986(14)	2.10(17)
O7	4	0.1635(9)	0.0285(14)	0.1858(10)	2.21(13)
Si3	2	0.5029(5)	0.2500	0.3377(6)	1.82(7)
O5	2	0.6394(13)	0.2500	0.5173(15)	1.99(17)
O8	4	0.5010(9)	0.0219(13)	0.2426(10)	2.09(11)
OH1	2	0.3795(15)	0.2500	0.9394(15)	2.20(20)
OH2	2	0.9324(14)	0.2500	0.5860(15)	2.16(18)
OH3	2	0.0649(16)	0.2500	0.9036(6)	2.56(12)

[a] refined to 0.61(2) Mn^{3+} and 0.39 Al^{3+} occupancy;
[81] for composition see footnote in Table 3.

Table 3. Crystal structures and lattice parameters.

Silicate	*T* [K]	Space group	Lattice parameters				Refs.
			a [Å]	*b* [Å]	*c* [Å]	β	
Epidote[1)]	RT	$P2_1/m$	8.914(9)	5.640(3)	10.162(9)	115.4(2)°	71D1
Epidote[1)]	RT	$P2_1/m$	8.96	5.63	10.30	115.4 °	50I1
Epidote[2)]	RT	$P2_1/m$	8.8877(14)	5.6275(8)	10.1517(2)	115.383(14)°	73G1
Epidote[3)]	RT	$P2_1/m$	8.8802(10)	5.6043(8)	10.1511(13)	115.455(12)°	73G1
Epidote[4)]	RT	$P2_1/m$	8.877(2)	5.602(1)	10.149(2)	115.46(1)°	92S1
Zoisite[5)]	RT	Pnma	16.212(8)	5.559(6)	10.036(4)		68D1
Zoisite[6)]	RT	Pnma	16.199(1)	5.5520(6)	10.0423(8)		92S1
Zoisite[7)]	RT	Pnma	16.198(1)	5.5483(5)	10.0330(7)		92S1
Zoisite[8)]	RT	Pnma	16.2051(37)	5.5488(12)	10.0229(18)		02L1
Zoisite[9)]	RT	Pnma	16.185(2)	5.550(1)	10.034(2)		88S1
Clinozoisite[10)]	RT	$P2_1/m$	8.879(5)	5.583(5)	10.155(6)	115.50(5)°	68D1
Piemontite[11)]	RT	$P2_1/m$	8.878(10)	5.692(5)	10.201(10)	115.40(2)°	69D1
Piemontite[12)]	RT	$P2_1/m$	8.85(1)	5.68(1)	10.20(2)	115° 35(8)′	79K1
Piemontite[13)]	RT	$P2_1/m$	8.86(1)	5.70(1)	10.19(2)	115° 33(8)′	79K1
Piemontite[14)]	RT	$P2_1/m$	8.87(1)	5.71(1)	10.18(2)	115° 40(8)′	79K1
Piemontite[15)]	RT	$P2_1/m$	8.85(1)	5.69(1)	10.19(2)	115° 40(8)′	79K1
Piemontite[16)]	RT	$P2_1/m$	8.87(1)	5.70(1)	10.21(2)	115° 48(8)′	79K1
Piemontite[16)]	RT	$P2_1/m$	8.87(1)	5.70(1)	10.19(2)	115°48(8)′	79K1
Piemontite[17)]	RT	$P2_1/m$	8.85(1)	5.68(1)	10.22(2)	115°48(8)′	79K1
Piemontite[18)]	RT	$P2_1/m$	8.839(3)	5.644(2)	10.166(4)	115.61(3)°	76L1, 77A1
Piemontite[19)]	RT	$P2_1/m$	8.847(2)	5.674(1)	10.170(1)	115.56(1)°	02L1
Piemontite[20)]	RT	$P2_1/m$	8.844(1)	5.677(1)	10.167(1)	115.54(1)°	02L1
Piemontite[21)]	RT	$P2_1/m$	8.855(1)	5.713(1)	10.208(1)	115.62(1)°	02L1
Hancockite[22)]	RT	$P2_1/m$	8.958(20)	5.665(10)	10.304(20)	114.4(4)°	71D1
Allanite[23)]	RT	$P2_1/m$	8.927(8)	5.761(6)	10.150(9)	114.77(5)°	71D1
Allanite[24)]	RT	$P2_1/m$	8.906(2)	5.659(2)	10.142(4)	114.77(2)°	88C1
Allanite[25)]	RT	$P2_1/m$	8.907(3)	5.665(3)	10.135(6)	114.67(2)°	88C1
Allanite[26)]	RT	$P2_1/m$	8.904(2)	5.668(2)	10.151(4)	114.62(1)°	88C1
Dissakisite-(Ce)[27)]	RT	$P2_1/m$	8.916(20)	5.700(8)	10.140(25)	114.72(14)°	91G1
Dollaseite-(Ce)[28)]	RT	$P2_1/m$	8.934(18)	5.721(7)	10.176(22)	114.31(12)°	88P1
Chevkinite[29)]	RT		13.44	5.72	11.10	100.20°	67I1
Chevkinite[29)]	RT		13.26	5.75	11.06	100.7°	67I1
Chevkinite[30)]	RT		13.43(2)	5.74(1)	11.07(1)	100.58(12)°	78S1
Chevkinite[31)]	RT		13.44(4)	5.73(2)	11.04(3)	100.61(25)°	78S1
Chevkinite[32)]	RT		13.40(2)	5.72(1)	11.09(1)	100.53(12)°	78S1
Mg-chevkinite[33)]	RT	$P2_1/a$	13.328(10)	5.727(4)	10.971(8)	100.91(6)°	74C1
Strontio-chevkinite[34)]	RT	$P2_1/a$	13.56	5.70	11.10	100.32°	83H1, 84D1
Co-chevkinite[35)]	RT	$P2_1/a$	13.325(4)	5.706(2)	10.998(2)	100.82(6)°	74C1
Chevkinite[36)]	RT		13.30	5.73	11.07	100.9°	67I1
Chevkinite[37)]	RT		13.24	5.68	10.98	100.8°	67I1
Chevkinite[38)]	RT		13.50	5.75	11.10	100.0°	67I1
Chevkinite[39)]	RT		13.28	5.72	11.05	100.8°	67I1
Chevkinite[40)]	RT		13.18	5.71	11.03	100.8°	67I1
Chevkinite[41)]	RT		13.24	5.73	11.05	100.6°	67I1
Chevkinite[42)]	RT		13.39	5.75	11.08	100.9°	67I1
Chevkinite[43)]	RT		13.14	5.68	10.96	100.8°	67I1
Chevkinite[44)]	RT		13.15	5.70	10.97	100.7°	67I1
Chevkinite[45)]	RT		13.12	5.68	10.95	101.0°	67I1
Chevkinite[46)]	RT		13.12	5.66	10.90	100.9°	67I1
Chevkinite[47)]	RT		13.22	5.71	11.00	101.0°	67I1

Table 3 (continued)

Silicate	T [K]	Space group	Lattice parameters				Refs.
			a [Å]	b [Å]	c [Å]	β	
$Mg_2Pr_4Ti_3Si_4O_{22}$ (Chevkinite)	RT	$P2_1/a$	13.376(2)	5.7074(7)	11.016(2)	100.71(1)°	71I1
$Ni_2Pr_4Ti_3Si_4O_{22}$ (Chevkinite)	RT	$P2_1/a$	13.362(3)	5.683(1)	11.008(3)	100.69(3)°	71I1
Perrierite[48)]	RT	$P2_1/a$	13.818(4)	5.677(2)	11.787(6)	113.85(3)°	74C1
Perrierite[29)]	RT		13.61	5.62	11.63	113.47°	78S1
Perrierite[49)]	RT		13.70(3)	5.66(2)	11.83(3)	113.79(18)°	78S1
Perrierite[29)]	RT		13.59	5.61	11.61	113.28°	67I1
Perrierite[29)]	RT		13.52	5.65	11.71	113.3°	67I1
Perrierite[50)]	RT		13.77	5.68	11.80	113.8°	67I1
Perrierite[51)]	RT		13.59	5.64	11.73	113.5°	67I1
Perrierite[52)]	RT		13.78	5.67	11.78	113.7°	67I1
Perrierite[53)]	RT		13.77	5.66	11.78	113.6°	67I1
Perrierite[54)]	RT		13.66	5.66	11.68	113.7°	67I1
Perrierite[55)]	RT		13.74	5.67	11.72	113.7°	67I1
Perrierite[56)]	RT		13.74	5.64	11.77	113.8°	67I1
Perrierite[57)]	RT		13.55	5.63	11.70	113.6°	67I1
Perrierite[58)]	RT		13.58	5.64	11.73	113.6°	67I1
Perrierite[59)]	RT		13.82	5.68	11.84	113.9°	67I1
Perrierite[60)]	RT		13.48	5.61	11.57	113.5°	67I1
Perrierite[61)]	RT		13.72	5.65	11.74	113.8°	67I1
Perrierite[62)]	RT		15.56	5.62	11.62	113.4°	67I1
Perrierite[63)]	RT		13.54	5.61	11.58	113.7°	67I1
Perrierite[64)]	RT		13.48	5.60	11.57	113.5°	67I1
Perrierite[65)]	RT		13.45	5.59	11.48	113.5°	67I1
Perrierite[66)]	RT		13.63	5.65	11.82	113.8°	67I1
Perrierite[67)]	RT		13.72	5.65	11.68	113.9°	67I1
$Mg_2La_4Ti_3Si_4O_{22}$ (Perrierite)	RT	$P2_1/a$	13.786(4)	5.6766(9)	11.791(3)	113.88(2)°	71I1
$Mg_2Pr_4Ti_3Si_4O_{22}$ (Perrierite)	RT	$P2_1/a$	13.57(1)	5.643(3)	11.66(1)	113.1(1)°	71I1
$Ni_2Pr_4Ti_3Si_4O_{22}$ (Perrierite)	RT	$P2_1/a$	13.57(1)	5.655(3)	11.70(1)	113.34(4)°	71I1
Vesuvianite[68)]	RT	P4/nnc	15.5232(4)		11.8167(4)		69A1
Vesuvianite[69)]	RT	P4/nnc	15.5333(2)		11.7778(2)		69A1
Vesuvianite[70)]	RT	P4/nnc	15.532(3)		11.776(3)		86F1
Vesuvianite[71)]	RT	P4/nnc	15.517(6)		11.781(4)		92O1
Vesuvianite[72)]	RT	P4/nnc	15.606(4)		11.825(4)		92O1
Vesuvianite[73)]	RT	P4/nnc	15.583(18)		11.801(17)		92O1
Vesuvianite[74)]	RT	P4/nnc	15.546(23)		11.828(14)		92O1
Vesuvianite[75)]	293	P4nc	15.487(2)		11.764(2)		00A1
Vesuvianite[76)]	293	P4/n	15.531(2)		11.817(2)		00A1
Danburite[77)]	RT	Pnma	8.01	8.75	7.72		64B1
Danburite[78)]	298	Pnma	8.037(1)	8.757(1)	7.7218(9)		85S1
Danburite[79)]	RT	Pnma	8.0456(7)	8.7629(4)	7.7341(7)		92D1
Macfallite[80)]	RT	$P2_1/m$	8.929(6)	6.045(5)	10.905(7)	119.10(3)°	79M1
Macfallite[81)]	RT	$P2_1/m$	10.235(3)	6.086(2)	8.970(5)	110.75(3)°	85M1
Sursassite[82)]	RT	$P2_1/m$	8.70(1)	5.79(1)	9.78(1)	108.9(1)°	84M1
Mg-sursassite[83)]	RT		8.5421(6)	5.7130(3)	9.6507(6)	108.272(4)°	01G1
Mg-sursassite[84)]	RT		8.5437(6)	5.7103(8)	9.6439(7)	108.334(4)°	01G1
Mg-sursassite[85)]	RT		8.5409(4)	5.7122(3)	9.6490(5)	108.288(1)°	01G1

Table 3 (continued)

Silicate	*T* [K]	Space group	Lattice parameters				Refs.
			a [Å]	*b* [Å]	*c* [Å]	β	
$Mg_4(MgAl)Al_4[Si_6O_{21}(OH)_7]$	RT	A2/m	8.544(1)	5.717(1)	18.491(2)	97.75(1)°	86S1, 91S1
$Mg_4(MgAl)Al_4[Si_6O_{21}(OH)_7]$ [86)]	RT	$P2_1/m$	8.5424(8)	5.7117(3)	9.6484(6)	108.298(4)°	00G1
Ruizite [87)]	RT	$P2_1/c$	11.95	6.17	9.03	91°22.5′	77W1
Ruizite [88)]	RT	C2/m	9.064(1)	6.171(2)	11.976(3)	91.38(2)°	85M1
Orientite [89)]	RT	Pcmm	9.044(10)	6.091(7)	19.031(2)		86M1
Orientite [90)]	RT	Bbmn	9.074(4)	19.130(7)	6.121(5)		85M1
Kittatinnyite [91)]	RT	$P6_3/mmc$, $P6_3mc$ or $P\bar{6}2c$	6.498(4)		22.78(2)		83D1
Ardennite [92)]	RT	Pnmn	8.7126(8)	5.8108(8)	18.5214(11)		68D2

[1)] $Ca_2Al_{2.15}Fe^{3+}_{0.31}Ti_{0.02}Mn_{0.04}Si_3O_{13}H$;
[2)] $Ca_2Al_{2.16}Fe_{0.84}Si_3O_{13}H$;
[3)] $Ca_2Al_{2.60}Fe_{0.40}Si_3O_{13}H$;
[4)] $Ca_{2.0}Al_{2.46}Fe_{0.52}Si_3O_{12}OH$;
[5)] $Ca_2Al_3Si_3O_{12}OH$ with 1.4 wt % Fe_2O_3, < 0.1 wt % Mn_2O_3;
[6)] $Ca_{1.99}Sr_{0.01}Al_{2.99}Mg_{0.01}V_{0.01}Si_{3.00}O_{12}OH$;
[7)] $Ca_{2.00}Al_{3.00}V_{0.02}Si_{2.98}O_{12}OH$;
[8)] $Ca_2Al_{2.87}Mn^{3+}_{0.03}Fe^{3+}_{0.10}[OH|O|SiO_4|Si_2O_7]$;
[9)] treated at 550°C (natural sample);
[10)] $Ca_2Al_{2.97}Fe_{0.03}Si_3O_{13}H$;
[11)] $(Ca_{1.78}Mn^{2+}_{0.13}Na_{0.10}K_{0.03})(Al_{1.73}Mn^{3+}_{0.76}Fe^{3+}_{0.51})Si_3O_{12.45}(OH)_{0.08}$;
[12)] $Ca_2Al_2MnSi_3O_{12}(OH)$, $T = 550°C$, $p_{fluid} = 2$ kbar;
[13)] $Ca_2Al_2MnSi_3O_{12}(OH)$, $T = 524°C$, $p_{fluid} = 2$ kbar;
[14)] $Ca_2Al_2MnSi_3O_{12}(OH)$, $T = 528°C$, $p_{fluid} = 2$ kbar;
[15)] $Ca_2Al_2MnSi_3O_{12}(OH)$, $T = 550°C$, $p_{fluid} = 8$ kbar;
[16)] $Ca_2Al_2MnSi_3O_{12}(OH)$, $T = 569°C$, $p_{fluid} = 2$ kbar;
[17)] $Ca_2Al_2MnSi_3O_{12}(OH)$, $T = 598°C$, $p_{fluid} = 2$ kbar;
[18)] $Ca_2Al_2MnSi_3O_{12}(OH)$, $T = 800°C$, $p_{fluid} = 15$ kbar;
[19)] $Ca_2Al_{2.17}Mn_{0.83}[OH|O|SiO_4|Si_2O_7]$;
[20)] $Ca_2Al_{2.02}Mn_{0.98}[OH|O|SiO_4|Si_2O_7]$;
[21)] $Ca_2Al_{1.53}Mn_{1.47}[OH|O|SiO_4|Si_2O_7]$;
[22)] $(Ca_{1.17}Mn^{2+}_{0.17}Pb_{0.47}Sr_{0.21})(Al_{1.95}Fe_{0.88}Mn_{0.10}Mg_{0.07})(Si_{2.95}Al_{0.05})O_{13}H$;
[23)] $(Ca_{1.20}Y_{0.02}La_{0.23}Ce_{0.48}Nd_{0.07})(Al_{1.65}Fe_{1.20}Ti_{0.06}Mn_{0.04}Mg_{0.04})Si_3O_{13}H$;
[24)] $CaLa_{0.9}Gd_{0.1}Al_2MgSi_3O_{13}H$;
[25)] $CaLa_{0.9}Er_{0.1}Al_2MgSi_3O_{13}H$;
[26)] $CaLa_{0.9}Lu_{0.1}Al_2MgSi_3O_{13}H$;
[27)] $Ca_{1.05}(Ce_{0.57}La_{0.33}Nd_{0.07}Pr_{0.03})Mg_{0.93}Fe_{0.14}Ti_{0.06}Al_{1.91}Si_{2.94}O_{12}(OH)_{0.94}F_{0.06}$;
[28)] $(Ca_{0.91}Ce_{0.45}La_{0.20}Nd_{0.20}Pr_{0.09}Sm_{0.08}Gd_{0.06})(Mg_{1.81}Fe_{0.25})Al_{0.97}Si_{3.00}(OH)_{1.25}F_{0.88}O_{10.99}$;
[29)] natural sample;
[30)] $Si_{3.992}Al_{0.024}Ti_{2.616}Fe_{1.565}Mn_{0.460}Mg_{0.027}Ca_{0.459}Sr_{0.034}Na_{0.058}K_{0.020}Th_{0.169}Y_{0.007}La_{1.832}Ce_{1.503}Pr_{0.180}Nd_{0.114}Tb_{0.012}Dy_{0.010}Ho_{0.004}Yb_{0.004}O_{22}$;
[31)] $Si_{3.973}Ti_{2.529}Fe_{1.870}Mn_{0.144}Mg_{0.040}Ca_{0.575}Na_{0.037}K_{0.018}Th_{0.143}Y_{0.041}La_{1.489}Ce_{1.692}Pr_{0.183}Nd_{0.232}Eu_{0.005}Tb_{0.014}Ho_{0.006}Yb_{0.009}O_{22}$;
[32)] $Si_{3.975}Al_{0.017}Ti_{2.569}Fe_{1.683}Mn_{0.171}Mg_{0.147}Ca_{0.686}Sr_{0.037}Na_{0.065}K_{0.017}Th_{0.074}Y_{0.031}La_{1.754}Ce_{1.411}Pr_{0.180}Nd_{0.166}Tb_{0.015}Yb_{0.004}O_{22}$;

Table 3 (continued)

33) $Mg_2Nd_4Ti_3Si_4O_{22}$;
34) $(Sr_2(LaCe)_{1.5}Ca_{0.5})(Fe^{2+}_{0.5}Fe^{3+}_{0.5})(Ti,Zr)_2Ti_2Si_4O_{22}$;
35) $Co_2Nd_4Ti_3Si_4O_{22}$;
36) $Ce_4Fe(FeTi)Ti_2Si_4O_{22}$;
37) $Pr_4Ni(NiTi)Ti_2Si_4O_{22}$;
38) $La_4Fe(FeTi)Ti_2Si_4O_{22}$;
39) $Pr_4Co(CoTi)Ti_2Si_4O_{22}$;
40) $Nd_4Fe(FeTi)Ti_2Si_4O_{22}$;
41) $Pr_4Fe(FeTi)Ti_2Si_4O_{22}$;
42) $(Ce_2La_2)Fe(FeTi)Ti_2Si_4O_{22}$;
43) $Nd_4Ni(NiTi)Ti_2Si_4O_{22}$;
44) $Nd_4Co(CoTi)Ti_2Si_4O_{22}$;
45) $Sm_4Co(CoTi)Ti_2Si_4O_{22}$;
46) $Sm_4Ni(NiTi)Ti_2Si_4O_{22}$;
47) $Nd_4Mg(MgTi)Ti_2Si_4O_{22}$;
48) $Mg_2La_4\ Ti_3Si_4O_{22}$;
49) $Si_{4.022}Al_{0.088}Ti_{2.807}Fe_{1.331}Mn_{0.281}Mg_{0.116}Ca_{0.823}Sr_{0.145}Na_{0.178}Th_{0.030}Y_{0.042}La_{1.511}Ce_{1.302}Pr_{0.153}Nd_{0.157}Tb_{0.009}Yb_{0.006}O_{22}$;
50) $La_4Co(CoTi)Ti_2Si_4O_{22}$;
51) $(La_2Nd_2)Ni(NiTi)Ti_2Si_4O_{22}$;
52) $La_4Mg(MgTi)Ti_2Si_4O_{22}$;
53) $Pr_4Mg(MgTi)Ti_2Si_4O_{22}$;
54) $(La_2Pr_2)Ni(NiTi)Ti_2Si_4O_{22}$;
55) $(La_3Pr)Ni(CoTi)Ti_2Si_4O_{22}$;
56) $La_4Ni(NiTi)Ti_2Si_4O_{22}$;
57) $(Ce_3Ca)Fe(AlTi)Ti_2Si_4O_{22}$;
58) $(Ce_3Sr)Fe(AlTi)Ti_2Si_4O_{22}$;
59) $(La_3Sr)Fe(GaTi)Ti_2Si_4O_{22}$;
60) $Pr_4FeAl_2Ti_2Si_4O_{22}$;
61) $(La_3Ca)Fe(AlTi)Ti_2Si_4O_{22}$;
62) $Pr_4Fe(AlTi)Ti_2Si_3AlO_{22}$;
63) $(Pr_3Ca)Fe(AlTi)Ti_2Si_4O_{22}$;
64) $Ce_4FeAl_2Ti_2Si_4O_{22}$;
65) $Nd_4FeAl_2Ti_2Si_4O_{22}$;
66) $Ce_4Fe(Fe_{0.5}AlTi_{0.5})Ti_2Si_4O_{22}$;
67) $Ce_4Fe(AlTi)Ti_2Si_3AlO_{22}$;
68) natural sample (Asbestos, Quebec);
69) natural sample (Sanford, Maine);
70) $2[(Ca_{18.28}Mn_{0.68})Al_4(Fe_{0.29}Cu_{0.71})(Al_{6.36}Mg_{0.56}Ti_{0.03}Zr_{0.97})(Si_{17.51}Al_{0.49})O_{68}(OH_{8.5}F_{1.5})$;
71) $Si_{18.02}Ti_{0.02}Al_{11.04}Fe_{0.08}Mn_{0.07}Mg_{1.30}Ca_{18.98}Na_{0.13}Cu_{0.37}F_{2.44}O_x$ (O content not mentioned);
72) $Si_{18.00}Ti_{0.68}Al_{9.08}Fe_{2.01}Mn_{0.09}Mg_{1.25}Ca_{18.87}Na_{0.02}K_{0.01}F_{2.04}O_x$;
73) $Si_{18.00}Ti_{0.01}Al_{10.19}Fe_{1.69}Mn_{0.23}Mg_{0.88}Ca_{18.94}Na_{0.06}F_{2.14}O_x$;
74) $Si_{17.75}Ti_{0.12}Al_{9.65}Fe_{1.09}Mn_{0.01}Mg_{2.36}Ca_{19.00}Na_{0.01}K_{0.01}F_{0.08}O_x$;
75) $Si_{18.00}Al_{11.560}Mn_{0.811}Mg_{0.164}Cu_{0.282}Ca_{18.661}Sr_{0.019}Na_{0.596}F_{0.627}O_x$;
76) $Si_{18.00}Ti_{0.214}Al_{10.535}Cr_{0.015}Fe_{0.913}Mn_{0.191}Mg_{0.629}Cu_{0.020}Ca_{17.817}Na_{0.051}K_{0.013}Cl_{0.077}O_x$;
77) natural sample; composition not mentioned;
78) natural sample (in wt %) CaO – 22.29; Al_2O_3 – 0.22; SiO_2 – 48.22; $Na_2O < 0.03$; Fe_2O_3 – 0.44; MgO – 0.11; B_2O_3 – 28.56; H_2O – 0.32;
79) $CaB_2Si_2O_8$;
80) $Ca_2(Mn^{3+},Al)_3(OH)_3[SiO_4][Si_2O_7]$;

Table 3 (continued)

81) $Ca_2Mn_3Si_3O_{11}(OH)_3$;
82) $Mn_2Al_3[(OH)_3(SiO_4)(Si_2O_7)]$;
83) $Mg_{4.93}Al_{5.15}Si_{5.92}O_{21}(OH)_7$ – 7.33 wt % H_2O;
84) $Mg_{4.65}Al_{5.39}Si_{5.88}O_{21}(OH)_7$ – H_2O not determined;
85) $Mg_{4.81}Al_{5.23}Si_{5.92}O_{21}(OH)_7$ – 7.11 wt % H_2O;
86) high pressure $Mg_4(MgAl)Al_4[Si_6O_{21}(OH)_7]$, referred as MgMgAl – pumpellyite [86S1, 91S1] was found to be isostructural with sursassite [00G1];
87) natural sample (Arizona): CaO – 20.57; Mn_2O_3 – 23.42; SiO_2 – 39.14; H_2O – 16; idealized formula $Ca_2Mn_2Si_4O_{11}(OH)_4{\cdot}2H_2O$;
88) $Ca_2Mn_2Si_4O_{11}(OH)_4{\cdot}2H_2O$;
89) $Ca_{8.5}(Mn^{3+}_{8.77}Al^{3+}_{0.45}Fe^{3+}_{0.49}Mn^{2+}_{0.28})Si_{11.60}O_{42}(OH)_9 \cdot 4.9H_2O$;
90) $Ca_2Mn_3Si_3O_{10}(OH)_4$;
91) $Ca_{4.04}Mn_{5.88}Zn_{0.05}Si_{3.97}As_{0.09}O_{16}(OH)_8{\cdot}18H_2O$;
92) $Mn^{2+}_2(Mn^{2+},Ca)_2(AlOH)_4[(Mg,Al,Fe^{3+})OH]_2(As,V)O_4Si_3O_{10}(SiO_4)_2$; SiO_2 – 28.14; Al_2O_3 – 23.22; MnO – 25.33; As_2O_5 – 9.85; V_2O_5 – 0.82; Fe_2O_3 – 1.50; MgO – 3.83; CaO – 1.50; CuO – 0.46; Cr_2O_3 – 0.12; F_2 – 0.14; H_2O^+ – 5.04; miscellaneous – 0.11;
93) $Ca_2(Al_{0.68}Fe_{0.32})_3Si_3O_{12}(OH)$;
94) natural sample, composition not mentioned;
95) $Ca_{3.93}Al_{4.34}Fe_{1.74}Mg_{0.02}Mn^{3+}_{0.02}Si_{5.96}O_{24}(OH)$;
96) $Ca_{3.99}Al_{4.34}Fe_{1.62}Mn^{3+}_{0.01}Si_{6.03}O_{24}(OH)$;
97) $Ca_{3.90}Al_{4.42}Fe_{1.54}Mg_{0.01}Mn^{3+}_{0.04}Ti_{0.01}Si_{6.06}O_{24}(OH)$;
98) $Ca_{4.05}Al_{4.75}Fe_{1.16}Mg_{0.03}Ti_{0.01}Mn^{3+}_{0.06}Si_{5.97}O_{24}(OH)$;
99) $(Ce_{1.622}La_{1.054}Ca_{0.398}Pr_{0.154}Nd_{0.359}Sm_{0.044}Y_{0.010}Gd_{0.024}R_{0.032}Mn_{0.118}Fe^{2+}_{0.185})Fe^{2+}_{1.0}(Fe^{2+}_{0.064}Fe^{3+}_{1.657}Mg_{0.082}Ti_{0.199})Ti_{2.0}[(Si_{3.842}Al_{0.130}Ti_{0.028})O_{14}]O_{7.634}OH_{0.366}$;
100) natural sample: 4.9 wt % FeO; 0.12 wt % TiO_2;
101) natural sample (in wt %): 0.98 – FeO; 2.41 – TiO_2; 3.39 – MgO; 37.46 – CaO; 16.60 – Al_2O_3; 36.88 – SiO_2;
102) natural sample (in wt %): 3.65 – FeO; 0.95 – TiO_2; 1.79 – MgO ; 37.51 – CaO; 16.95 – Al_2O_3; 37.02 – SiO_2;
103) $Si_{17.993}Ti_{0.004}Al_{11.128}Fe_{0.105}Mn_{0.016}Ca_{18.863}F_{0.137}OH_{10.361}O_{68.364}$;
104a) $Si_{17.874}Al_{10.785}Cr_{0.011}Fe_{0.408}Mn_{0.016}Mg_{1.862}Ca_{19.043}OH_{11.960}O_{67.496}$;
104b) $Si_{17.651}Ti_{0.004}Al_{10.604}Cr_{0.008}Fe_{0.354}Mn_{0.004}Mg_{2.593}Ca_{18.779}F_{0.365}OH_{10.556}O_{67.677}$;
105) $Ca_2Al_3Si_3O_{12}(OH)$ doped with Cr^{3+}, Fe^{3+}, VO^{2+}_2, V^{4+};
106) natural sample (in wt %) SiO_2 – 37.6; TiO_2 – 0.01; Al_2O_3 – 19.24; FeO – 0.66; MnO – 0.34; MgO – 1.77; CaO – 35.0; CuO – 0.64; Na_2O – 0.11;
107) $Ca_2Al_2Fe[SiO_4][Si_2O_7]O(OH)$;
108) $Ca_2Al_3[SiO_4][Si_2O_7]O(OH)$;
109) $Ca_{10}(Mg,Fe)_2Al_4[Si_2O_7]_2[SiO_4]_5(OH,F)_4$;
110) $Si_{18.02}Al_{10.56}Fe_{0.58}Mn_{0.47}Mg_{1.22}Ca_{18.81}Na_{0.04}O_{73}$;
111) $Si_{18.18}Al_{9.60}Fe_{1.08}Mn_{0.20}Mg_{1.79}Ca_{19.16}O_{73}$;
112) $[Ca_{18.15}Mn_{0.03}Mg_{0.12}]Al_{4.00}Fe_{1.00}(Al_{5.25}Mg_{1.64}Fe_{0.47}Ti_{0.80})Si_{18.00}O_{69.33}(OH)_{10}$;
113) $[Ca_{18.89}Mn_{0.04}Mg_{0.07}]Al_{4.00}Fe_{1.00}(Al_{5.79}Mg_{1.70}Fe_{0.60}Ti_{0.11})Si_{18.00}O_{69.03}(OH)_{10}$;
114) $Ca_{2.0}(Al_{2.1}V_{0.8}Fe_{0.1})Si_{3.1}O_{12.0}(OH)$.

Table 4. Hyperfine parameters and site population (A) determined by ^{57}Fe nuclear gamma resonance.

Silicate [c]	T [K]	Site	δ [a] [mm/s]	ΔQ [mm/s]	DH [mm/s]	A [%]	Refs.
Epidote[93]	77		0.46	–2.02	0.34		
	RT		0.46	–2.05	0.34		83P1
Epidote[94]	100	M3	0.44	2.00			75P1
	200	M3	0.45	2.02			
	300	M3	0.45	2.02			
Epidote[29]	RT		0.45	2.02	0.40		67B2
Epidote[95]	RT	Fe^{3+}(M3)	0.36	2.00	0.35	86	91P2
		Fe^{3+}(M1)	0.31	0.90	0.40	11	
		Fe^{2+}	1.11	1.80	0.34	3	
Epidote[96]	RT	Fe^{3+}(M3)	0.36	2.00	0.31	92	91P2
		Fe^{3+}(M1)	0.36	1.00	0.50	8	
Epidote[97]	RT	Fe^{3+}(M3)	0.36	1.99	0.34	95	91P2
		Fe^{3+}(M1)	0.34	0.90	0.40	5	
Epidote[98]	RT	Fe^{3+}(M3)	0.36	2.06	0.35	100	91P2
Neptunite[29]	RT		1.26[b]	2.65	0.42		67B1
Chevkinite[99]	83	Fe^{2+}(R)	1.40	2.37	0.46	11	92L1
		Fe^{2+}(Mg,Fe) octahedra	1.23	2.06	0.46	33	
		Fe^{3+}(C1)	0.46	0.77	0.58	36	
		Fe^{3+}(C2)	0.42	1.26	0.58	20	
	283	Fe^{2+}(R)	1.25	2.21	0.48	9	
		Fe^{2+}(Mg,Fe) octahedra	1.14	2.25	0.48	34	
		Fe^{3+}(C1)	0.43	0.57	0.52	36	
		Fe^{3+}(C2)	0.33	1.34	0.52	21	
Vesuvianite[100]	RT	Fe^{3+} oct Al/Fe site	0.35	0.42	0.43	90	75M2
		Fe^{3+} Ca site	0.62	0.89	0.43	10	
Vesuvianite[101]	RT	Fe^{3+} oct Al/Fe site	0.39	0.46	0.43	39	75M2
		Fe^{2+} square pyramidal (5-coord)	0.84	0.37	0.39	51	
		Fe^{2+} Ca site	1.32	3.44	0.22	9	
		Fe^{2+}	0.85	1.04	0.43	12	
Vesuvianite[102]	RT	Fe^{3+} oct Al/Fe site	0.39	0.48	0.39	13	75M2
		Fe^{2+} square pyramidal (5-coord)	0.82	0.39	0.48	44	
		Fe^{2+} Ca site	1.32	3.44	0.20	1	
		Fe^{2+}	0.87	1.55	0.54	11	
		$Fe^{2+}_{oct.}$ (Al/Fe) site	1.13	2.74	0.40	31	

[a] relative to α-Fe; [b] relative to the value of 0.16 mm/s for the isomer shift of sodium nitroprusside;
[c] for composition see footnotes in Table 3.

Table 5. Data obtained by NMR studies at room temperature.

Silicate	Nucleus	Site	ΔQ[a)] [MHz]	η[b)]	δ[c)] [ppm]	Direction of external field	Second moment of ^{1}H resonance line [G]		Refs.
							measured	calculated	
Zoisite $Ca_2Al_3Si_3O_{12}(OH)$	^{27}Al	Al1 Al2	8.05 18.50	0.46 0.16					69B1
Zoisite $Ca_2Al_3Si_3O_{12}(OH)$	^{1}H					$\parallel$ ***a*** $\parallel$ ***c***	1.8(2) 2.3(2)	1.50(15) 2.00(20)	69B1
Vesuvianite[103)]	^{27}Al	5-coord. octah. coord octah. coord			41.1(5) 9.0(1.0) 2.5(1.0)				87P1
Vesuvianite[103)]	^{29}Si				–80[d)]				87P1
Danburite $CaB_2Si_2O_8$			0.412(4)	0.45					64B1

[a)] quadrupole splitting;
[b)] asymmetry parameter;
[c)] chemical shift; for ^{27}Al relative to $Al(H_2O)_6^{3+}$ in the form of a 1M $AlCl_3$ solution
[d)] relative to tetramethylsilane;
[103)] for composition see footnote in Table 3.

Table 6. Data obtained by EPR measurements.

Sample[a)]	Site	g_z	g_y	g_x	$A \cdot 10^4$ [cm^{-1}]			D [cm^{-1}]	E [cm^{-1}]	Refs.
					A_z	A_y	A_x			
Zoisite[105)]: VO_2^{2+} V^{4+}	1	1.948(1)	1.968(1)	1.942(1)	163.4(2)	53.3(2)	49.2(2)			71H1
	2	1.938(1)	1.928(1)	1.944(6)	161.7(2)	52.5(2)	45.2(4)			
	3	1.876(1)	1.981(1)	–	155.5(2)	61.1(2)				
	4	1.934(1)	1.944(1)	–	163.7(1.0)	52.9(2)				
Zoisite[105)]: Cr^{3+}		$g_\parallel$ = 1.9705(5); $g_\perp$ = 1.975(1)						0.6360(3)	0.0277(3)	71H1
Zoisite[105)]: Fe^{3+}		$g_\parallel = g_\perp$ = 2.000(1)						0.787(4)	0.015(1)	71H1
Vesuvianite[106)]: Cu^{2+}		$g_\parallel$ = 2.3404; $g_\perp$ = 2.0625			$A_\parallel$ = 14.78 mT; $A_\perp$ = 2.5 mT					92D2

[a)] for composition see footnotes in Table 3.

Table 7. Single crystal dielectric constants.

Sample[a)]	f [MHz]	χ_a;	tg $\delta \cdot 10^4$	χ_b;	tg $\delta \cdot 10^4$	χ_c;	tg $\delta \cdot 10^4$	χ_{11}	χ_{22}	χ_{33}	Refs.
Epidote[4)]	1	9.49(8);	8	17.1(1);	9	9.26(10);	6	9.52	17.1	9.37	92S1
Epidote[29)]	7	10.79;		14.29;		7.51;					64W1
Epidote[29)]	0.5	10.11;		15.39;		7.69;					53T1
Epidote[29)]	RF	9.99(14);		15.36(4);		7.60(13);					66K1
Zoisite[6)]	1	10.49(4);	6	13.31(6);	8	9.51(6);	8				92S1
Zoisite[7)]	1	10.55(2);	11	15.45(5);	13	9.39(4);	8				92S1
Vesuvianite[113)]	1	10.02(6);	20			9.853(7);	30				92S1
Vesuvianite[112)]	1	9.931(80);	60			9.794(30);					92S1
Vesuvianite[29)]	1	8.64;		undef. orientation							81O1
Vesuvianite[29)]	1	8.2;	102	undef. orientation							
Vesuvianite[29)]	1	8.6;	134	undef. orientation							

[a)] for composition see footnotes in Table 3.

Table 8. Local environments in synthetic $CaLa_{0.9}R_{0.1}Al_2MgSi_3O_{13}H$ with R = Gd, Er, Lu [88C1].

Photoelectron emitting atom	Coordination number	Atom type	Shell radius [Å]	$2\sigma^2$ [Å^2]
Gd	3	O	2.39	0.006
	2	O	2.57	0.006
	2	O	2.66	0.012
	2	O	2.85	0.032
	3	Si	3.48	0.011
	3	Ca	3.57	0.014
Er	3	O	2.26	0.011
	2	O	2.40	0.009
	2	O	3.01	0.017
	3	Si	3.50	0.036
	3	Ca	3.58	0.030
Lu	4	O	2.26	0.009
	2	O	2.43	0.005
	2	Si	3.41	0.015
	3	Ca	3.56	0.014
	3	Si	3.61	0.018

Table 9. Refractive indices.

Silicate [a)]	n_α	n_β	n_γ	$2V$		Refs.
Mukhinite[114)]	1.723(2)	1.733(2)	1.755(2)	88° (meas)	biaxial, positive	69S1
Dissakisite-(Ce)[27)]	1.735(3)	1.741(3)	1.758(3)	64.2(3)°(meas) 62° (calc)		91G1
Dollaseite (Ce)[29)]	1.715	1.718	1733			27G1
Karnasurite[94)]	1.617(ω)		1.595(ε)		uniaxial, negative	59V1
Macfallite[80)]	1.773(5)	1.795(5)	1.815(5)			79M1
Ruizite[87)]	1.663	1.715(‖ [010])	1.734			77W1
Kittatinnyite[91)]	1.723(ω)		ε (not determined)		uniaxial, negative	83D1

For pilmantite see [64S1].

[a)] for composition see footnotes in Table 3.

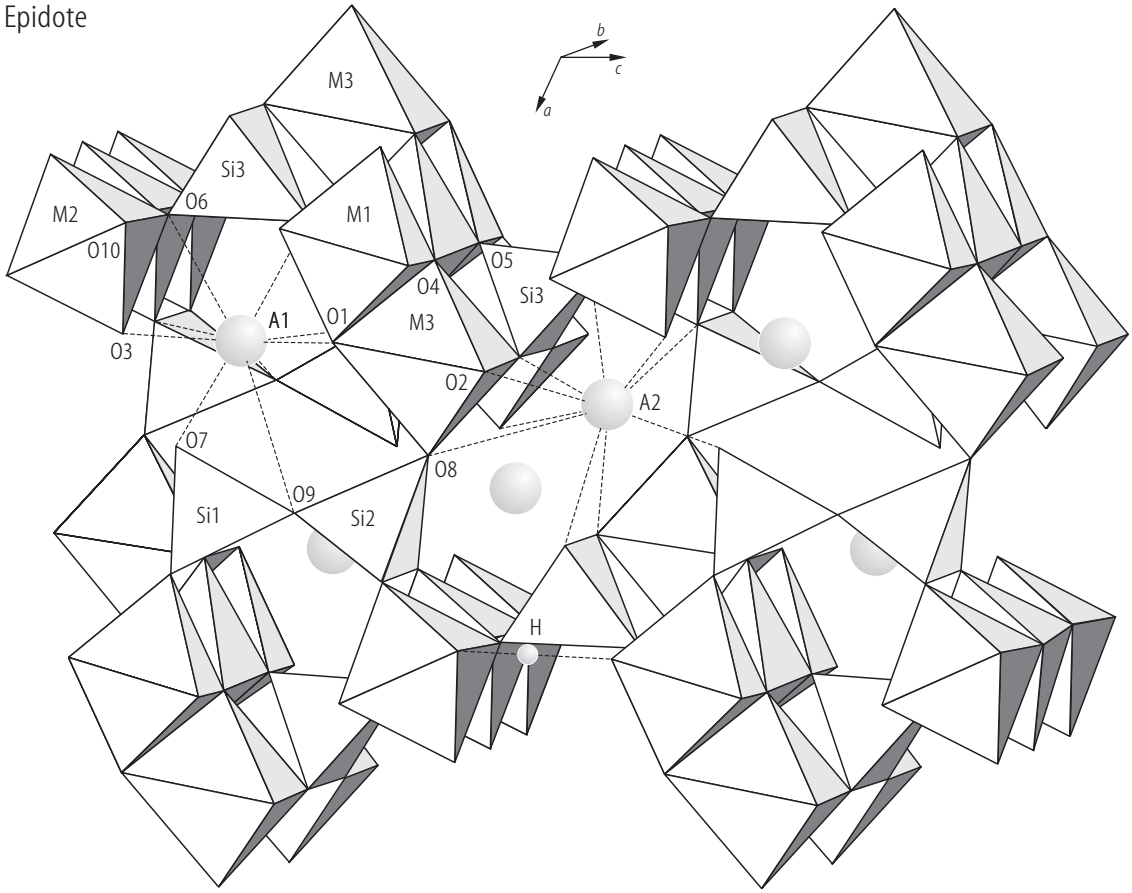

Fig. 1. Epidote. Polyhedral linkage [71D1].

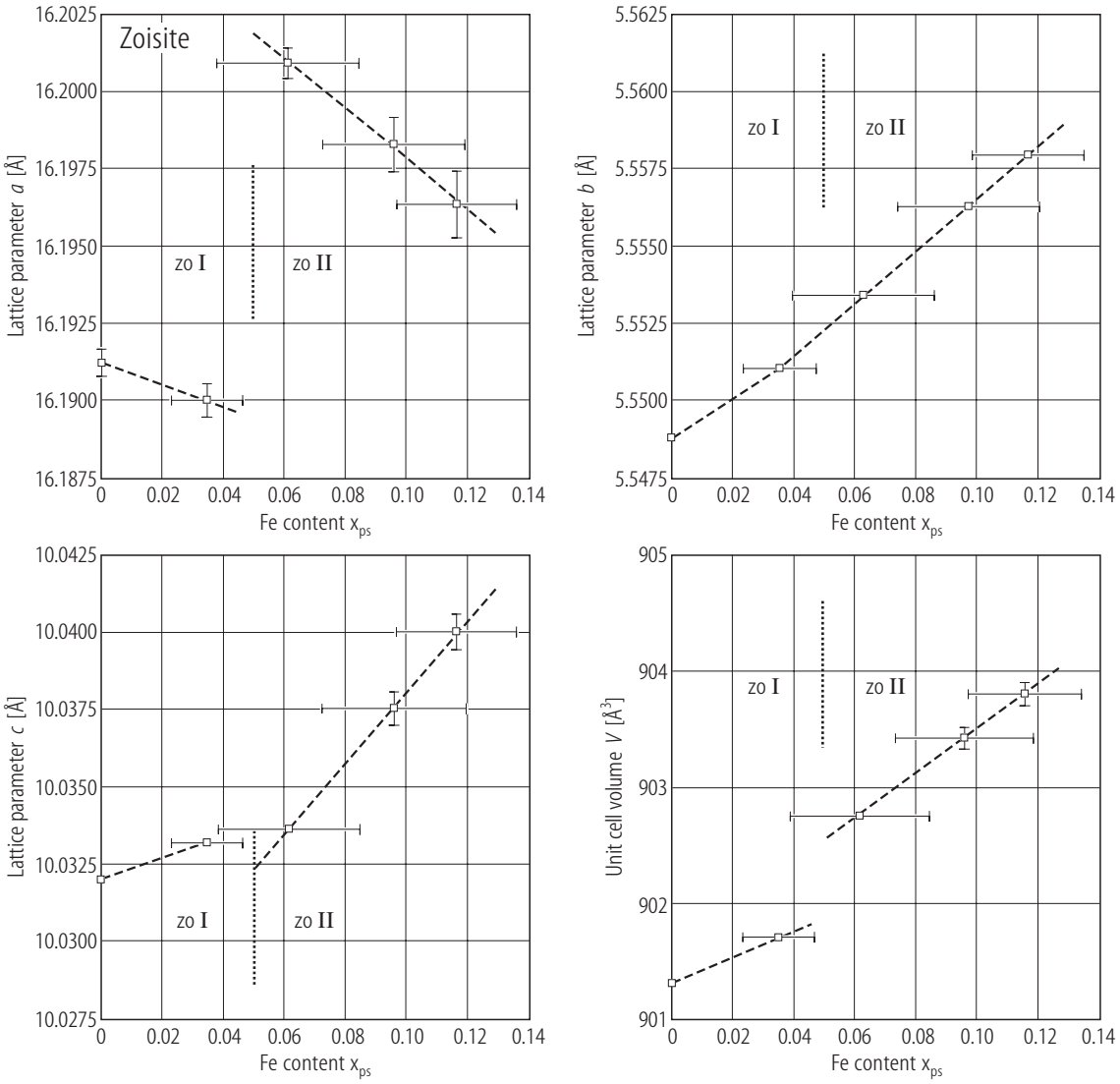

Fig. 2. Zoisite. Variation of lattice constants and cell volume with iron content. Discontinuities at ≅ 0.05 x_{ps} with a positive offset in *a*, *b* and *V* and a negative offset in *c*, point to the modifications zoisite I (zoI) and zoisite II (zoII) [02L2].

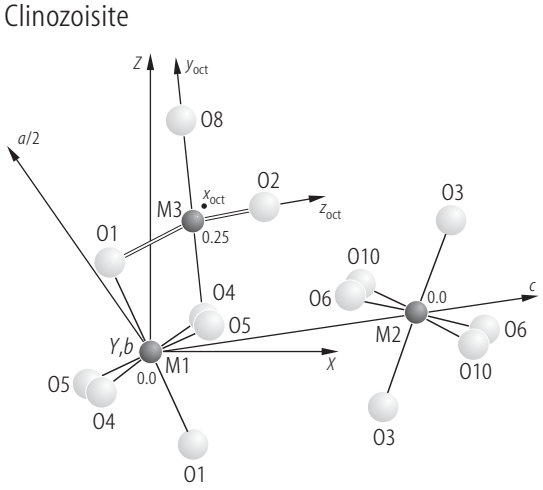

Fig. 3. Clinozoisite. The three different octahedra (M1, M2, M3) projected along the ***b***-axis onto the (010) plane. The orientations of the crystallographic ***a***- and ***c***-axes as well as that of the principal axes of the optical indicatrix ***X***, ***Y*** and ***Z*** and the internal octahedral axes of the M3 octahedron under the C_{2v} (C2") pseudo-symmetry applied in the assignment of spin-allowed dd-bands of Mn^{3+} (M3) are also shown [68D1, 02L1].

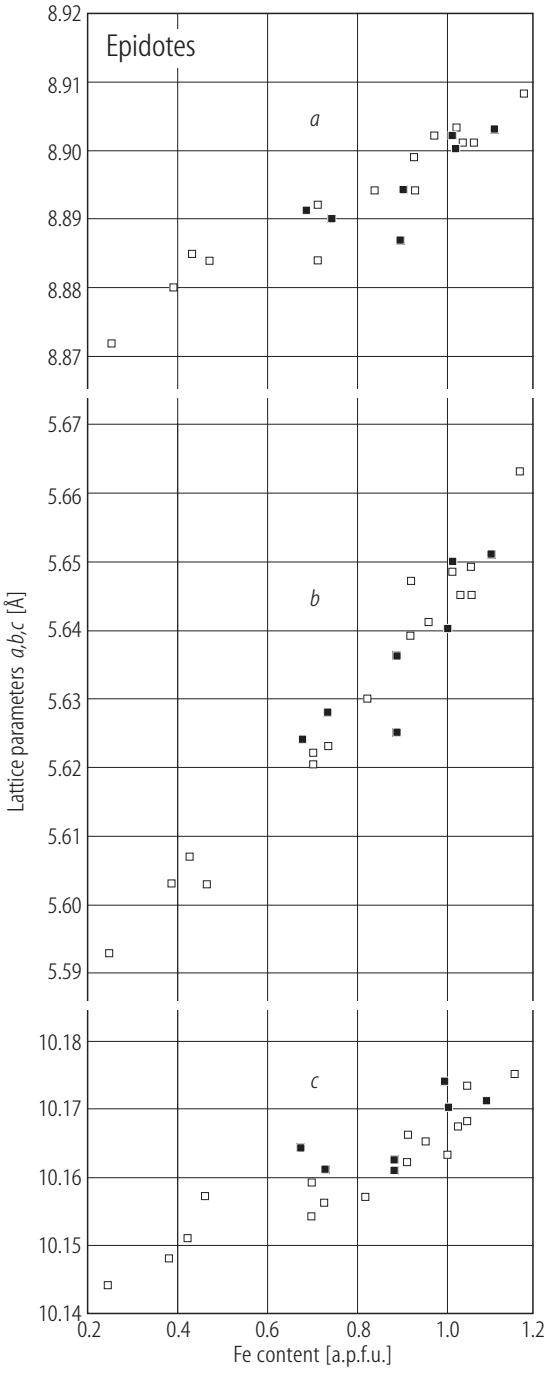

Fig. 4. Epidotes. Unit cell parameters versus total Fe content. Filled symbols are synthetic samples [99G1] and open ones are natural samples [95B1].

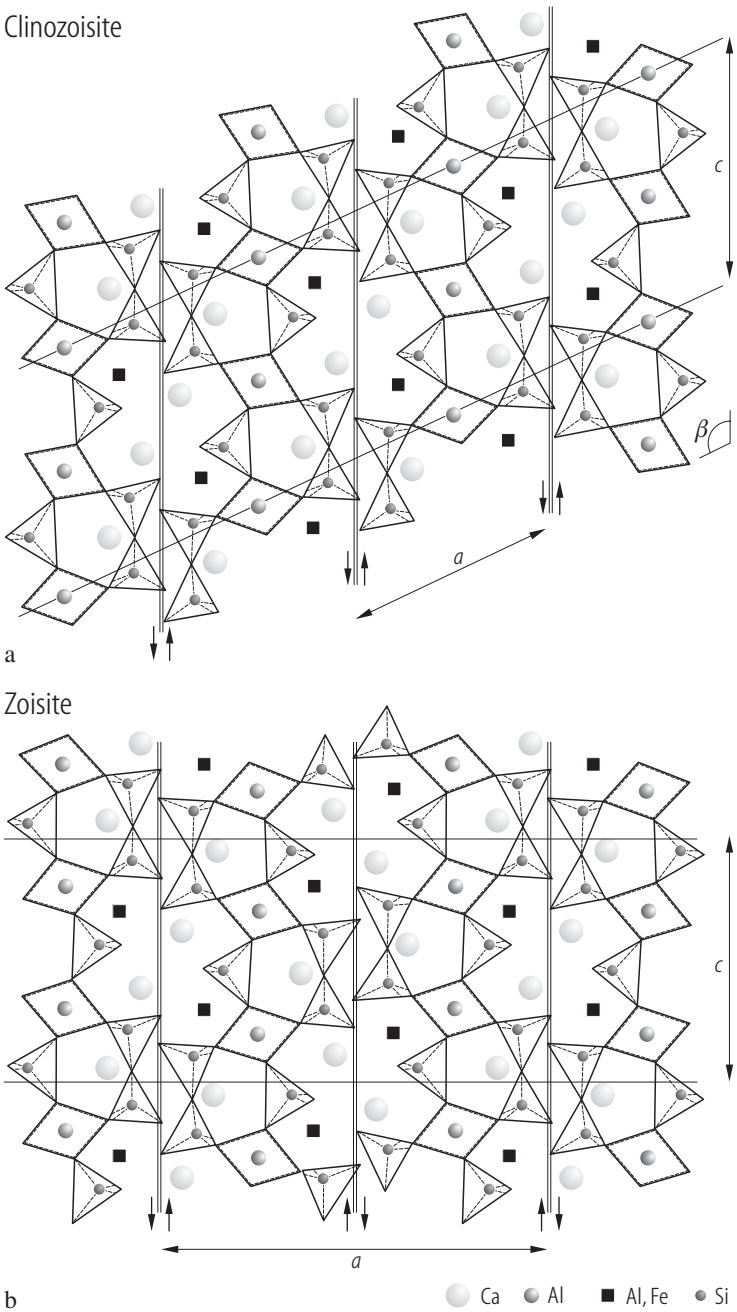

Fig. 5. Clinozoisite **(a)** and zoisite **(b)**. Structures projected down the ***b***-axis. Octahedral chain sites run parallel to the ***b***-axis and are linked by Si_2O_7 and SiO_4 tetrahedra. The boundaries to stacking modules are represented by double parallel lines on (100) planes. The zoisite structure is related to clinozoisite by a shear of (1/4) [001] on every other module boundary [86R1]. The origin of the clionozoisite unit cell has been moved by (1/2,0,0) from the coordinates given by [68D1].

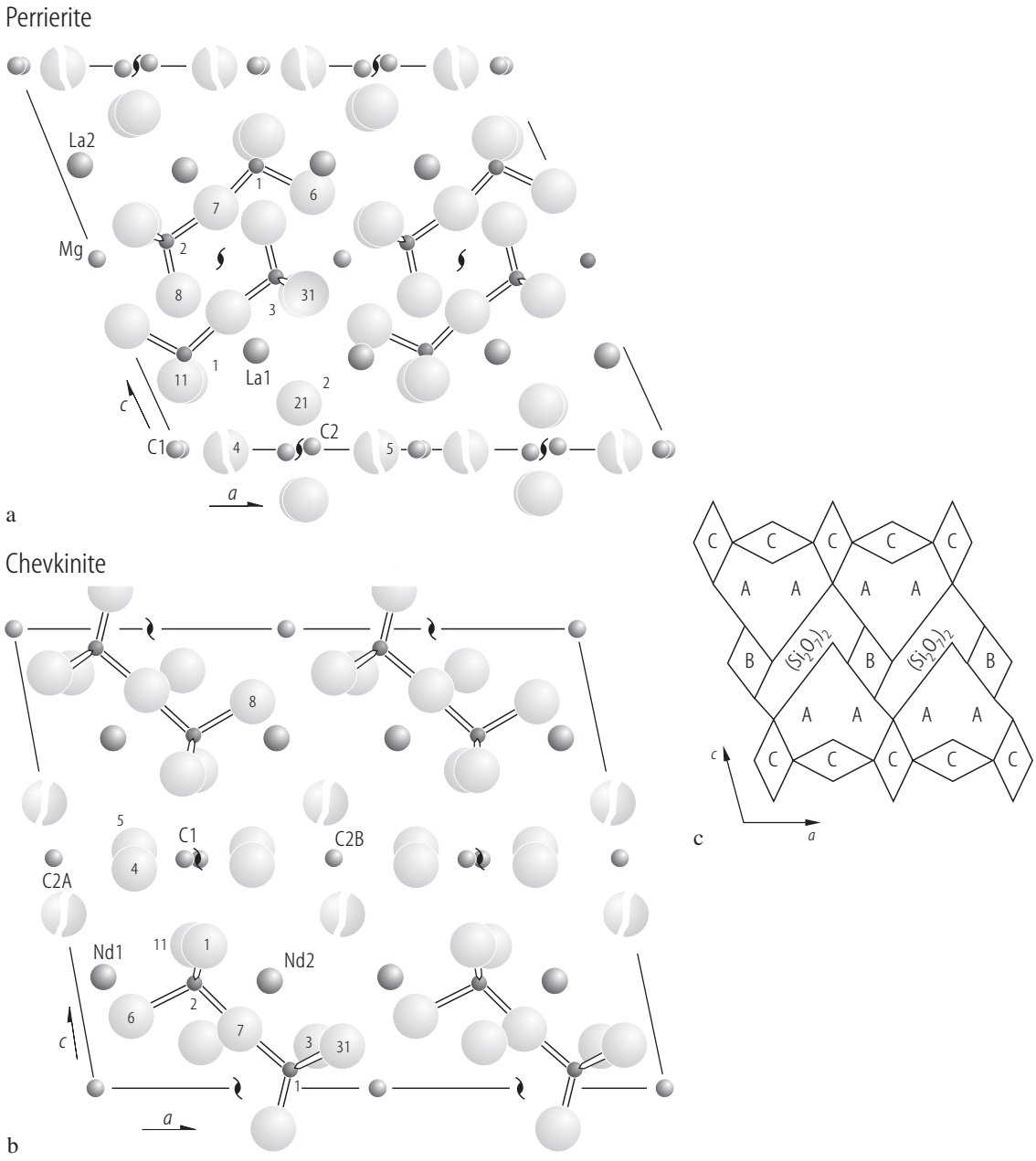

Fig. 6. Perrierite **(a)**, Chevkinite **(b)**. The 010 projection of the structures. The circles represent oxygen atoms, rare-earth ions, divalent metal ions and silicon atoms as their sizes decrease. The broken circles represent superimosed atoms [74C1]. **(c)** Diagrammatic 010 projection of the chevkinite-perrierite structure. A middle layer of $B(Si_2O_7)_2$ groups has octahedrally coordinated layers of C cations both above and below [71I1].

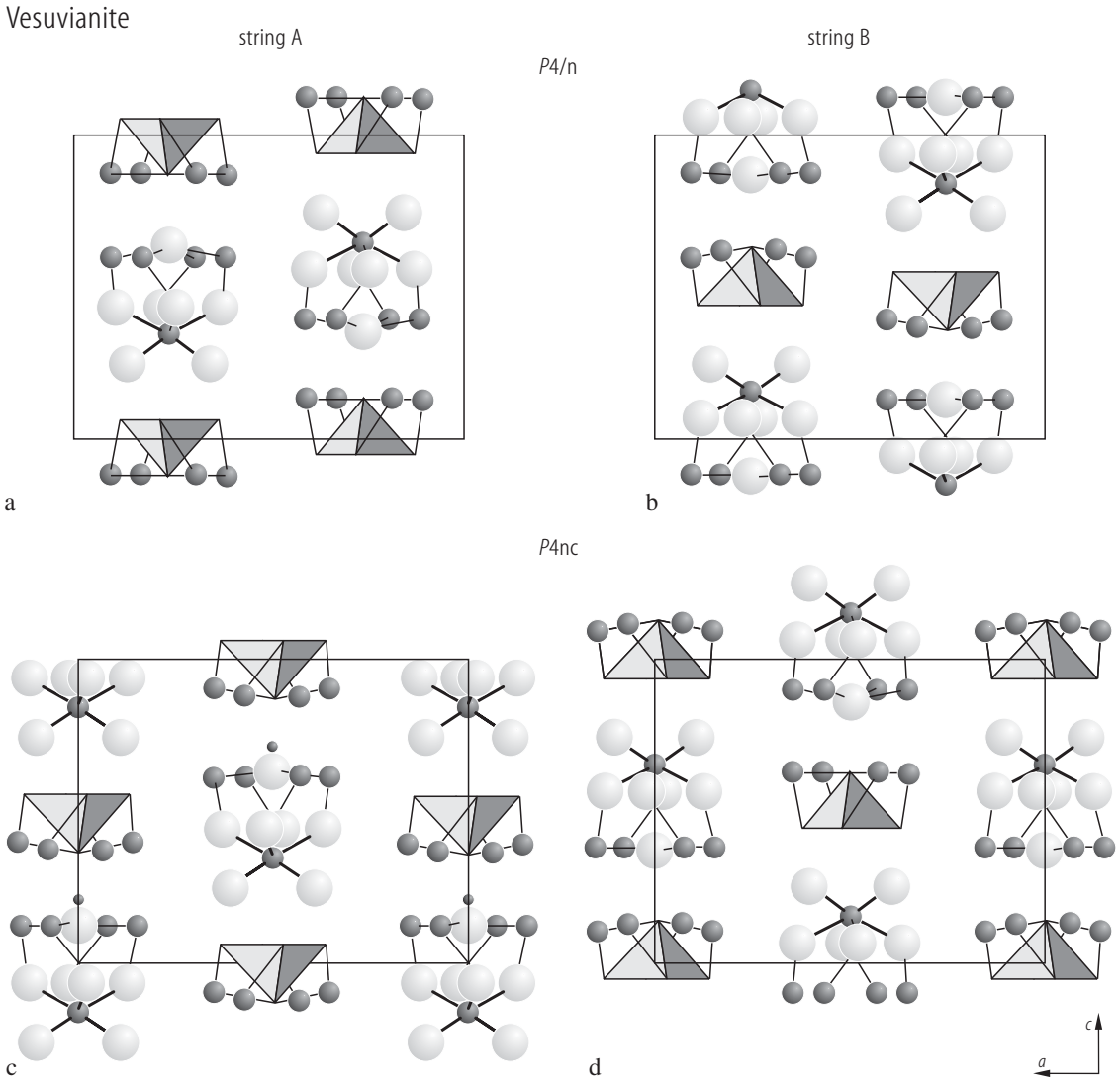

Fig. 7. Vesuvianites, long-range ordered. String arrangement along the fourfold axes. Large spheres represent O atoms, intermediate spheres are Ca, small spheres are hydrogen. For clarity the oxygen square pyramids around Y' sites are shown as polyhedra. **(a, b)** In the space group P4/n (origin at $\bar{1}$) the fourfold axes pass through x = 1/4, y = 1/4 and 3/4, 3/4. The two possible string arrangements have the apices of the square pyramids pointing in opposite directions along the two fourfold axes; **(c, d)** In the space group P4nc the fourfold axes pass through the origin and 1/2, 1/2. Each string type is characterized by apices of square pyramids pointing in the same direction [00A1].

Vesuvianite

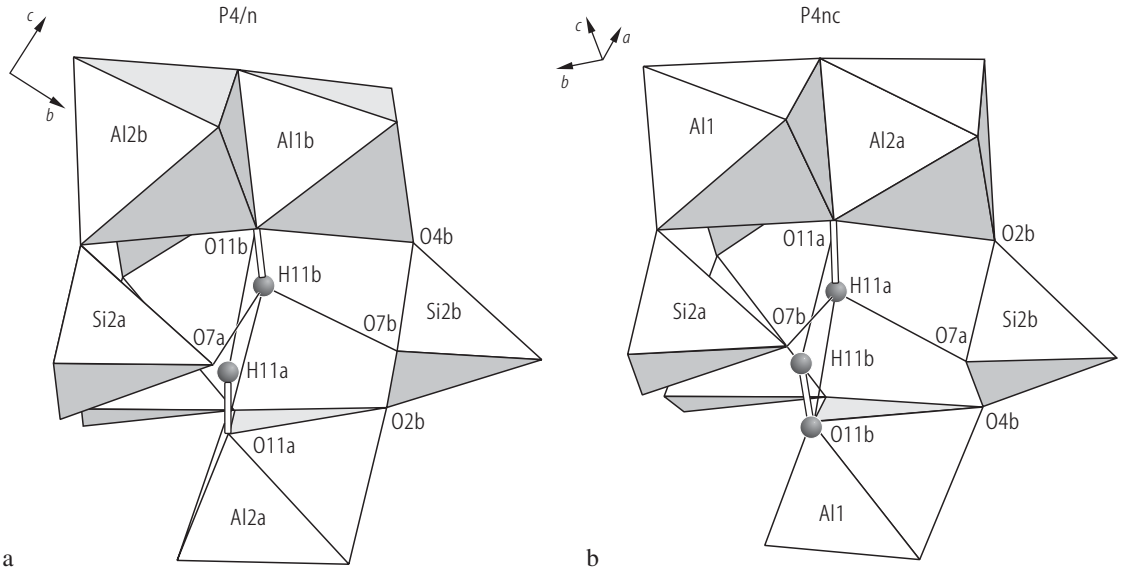

Fig. 8. Vesuvianites. Hydrogen bonding in low-temperature crystals. In P4/n sample **(a)** H11b has tri-furcated hydrogen bonds to O7a, O7b and O11a. H11a has its shortest hydrogen bond to O11b. In P4nc sample **(b)** H11a is tri-furcated and H11b is hydrogen bonded to O11a [00A1].

Danburite

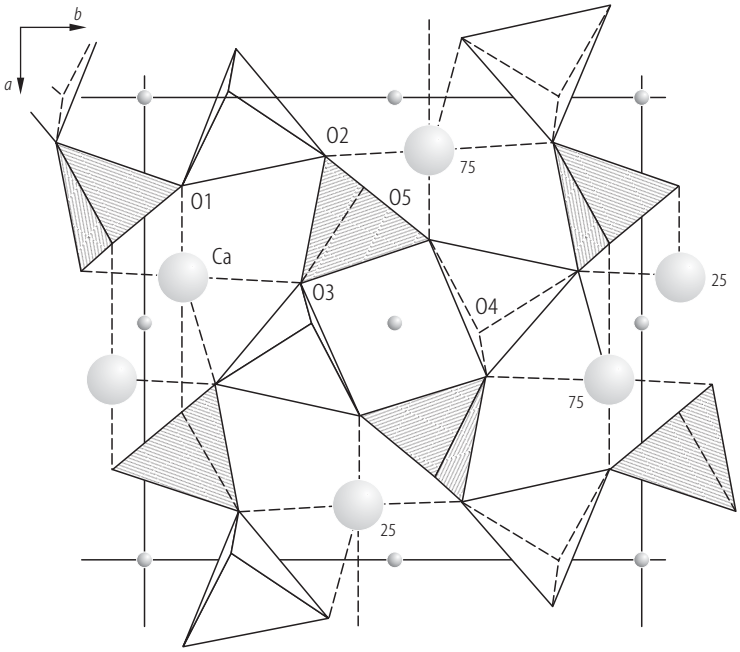

Fig. 9. Danburite. The structure viewed down ***c***-axis. Numbers indicate the heights of the Ca atoms in decimal fractions of the ***c***-axis. The BO_4 tetrahedra are shadowed. The apices of tetrahedra pointing up are in the mirror plane at *x*, *y*, 3/4 and those pointing down on the mirror plane at *x*, *y*, 1/4 [85S1].

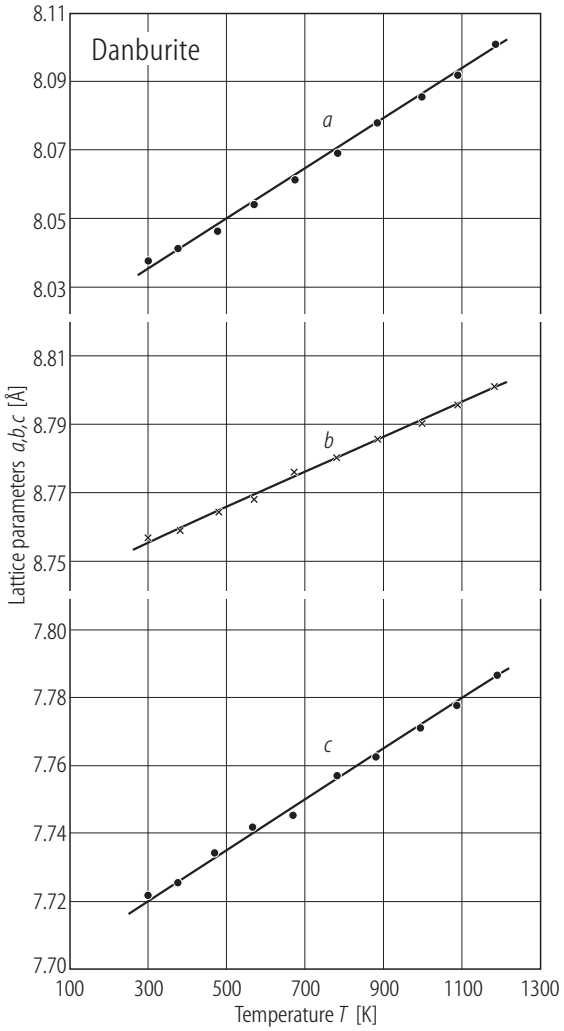

Fig. 10. Danburite. Temperature dependences of the lattice parameters [85S1].

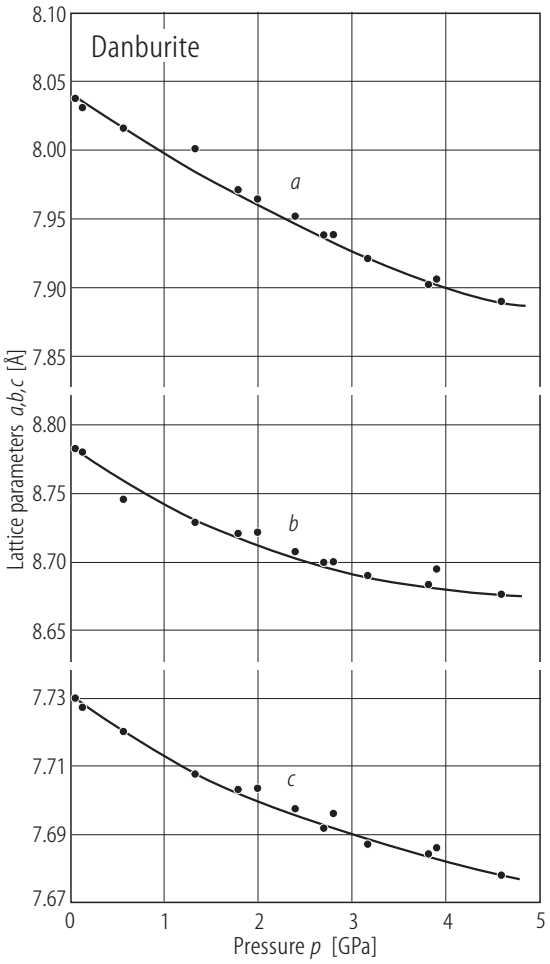

Fig. 11. Danburite. Pressure dependences of the lattice parameters [92H1].

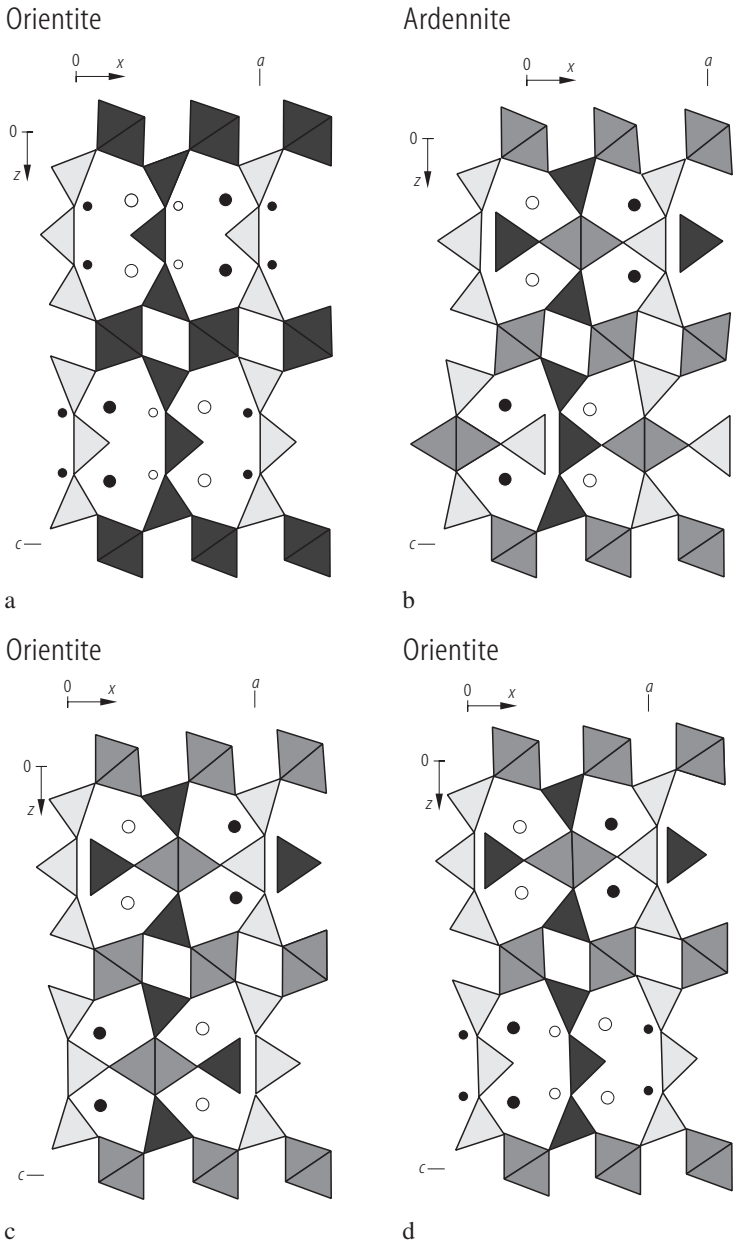

Fig. 12. Orientite, models for crystal structure: **(a)** [85M1] along [010]; **(c)** [82M1]; **(d)** [86M1]. In **(b)** ardennite is shown as seen along [010] [86M1]. Different grey tones indicate different y levels. Larger circles are Ca atoms, smaller circles are water molecules.

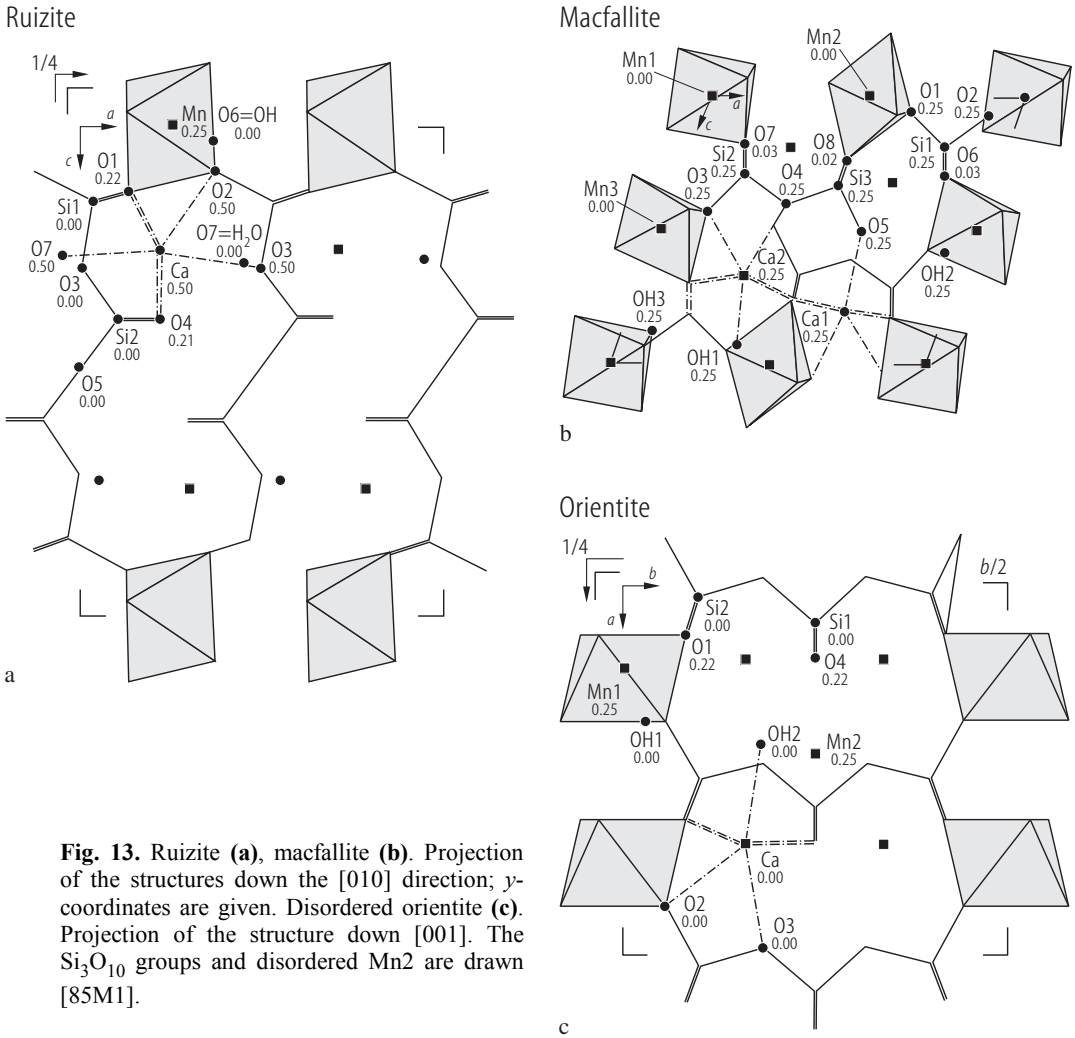

Fig. 13. Ruizite **(a)**, macfallite **(b)**. Projection of the structures down the [010] direction; *y*-coordinates are given. Disordered orientite **(c)**. Projection of the structure down [001]. The Si_3O_{10} groups and disordered Mn2 are drawn [85M1].

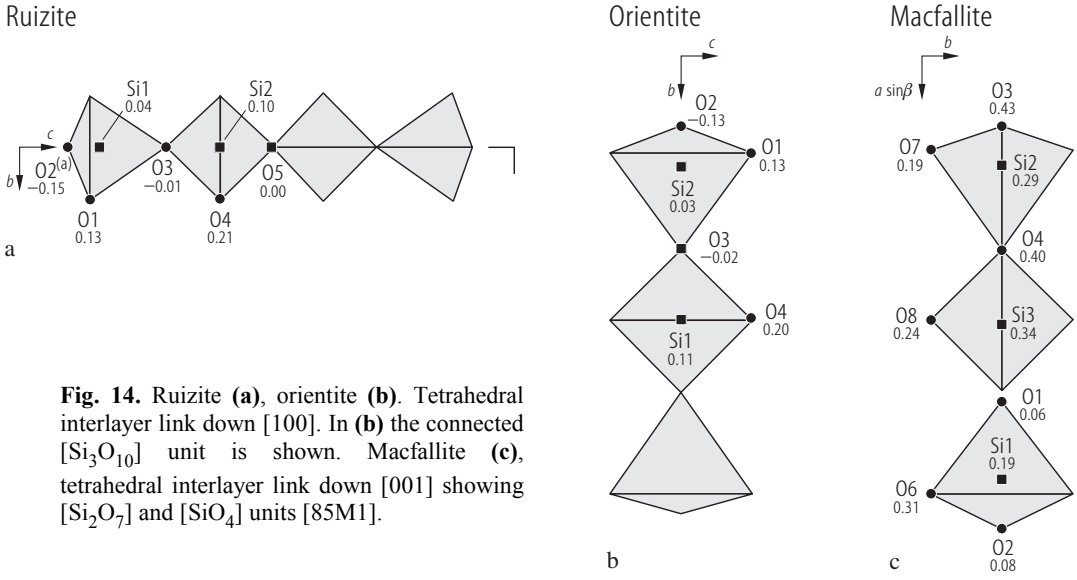

Fig. 14. Ruizite **(a)**, orientite **(b)**. Tetrahedral interlayer link down [100]. In **(b)** the connected $[Si_3O_{10}]$ unit is shown. Macfallite **(c)**, tetrahedral interlayer link down [001] showing $[Si_2O_7]$ and $[SiO_4]$ units [85M1].

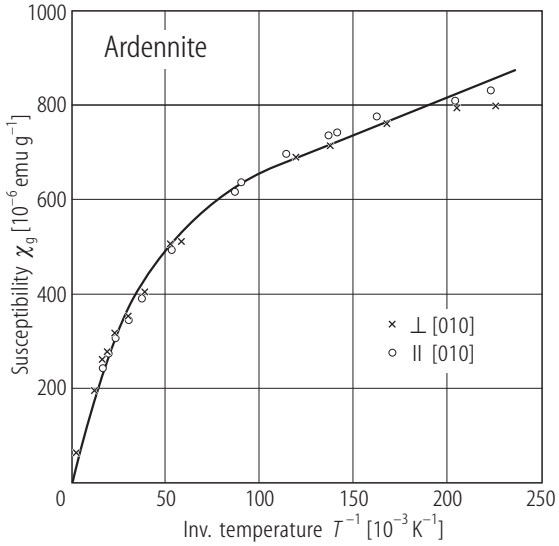

Fig. 15. Ardennite. Temperature dependences of the reciprocal susceptibilities perpendicular and parallel to the [010] direction [69T1].

For Figs. 16, 17 see next pages

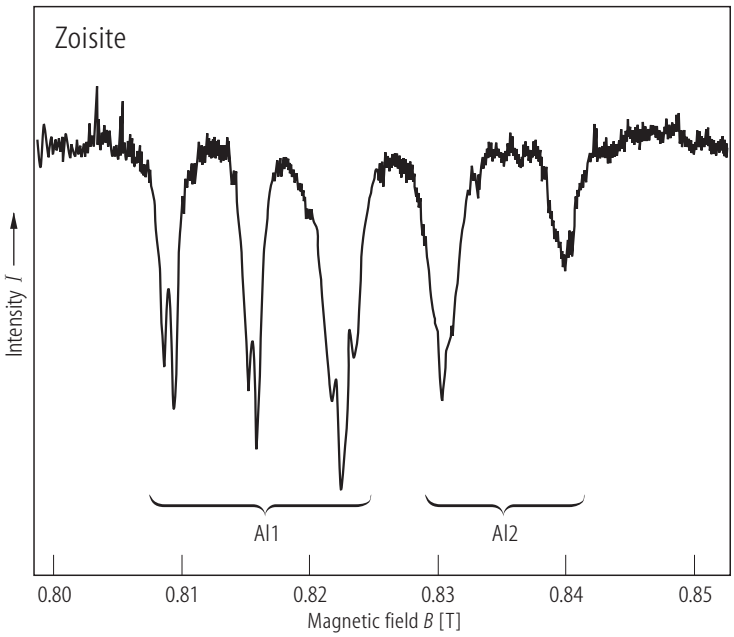

Fig. 18. Zoisite. ^{27}Al central lines of the NMR spectrum from the two inequivalent sites. The ***b***-axis is perpendicular to the magnetic field. Dispersion mode signals [69B1].

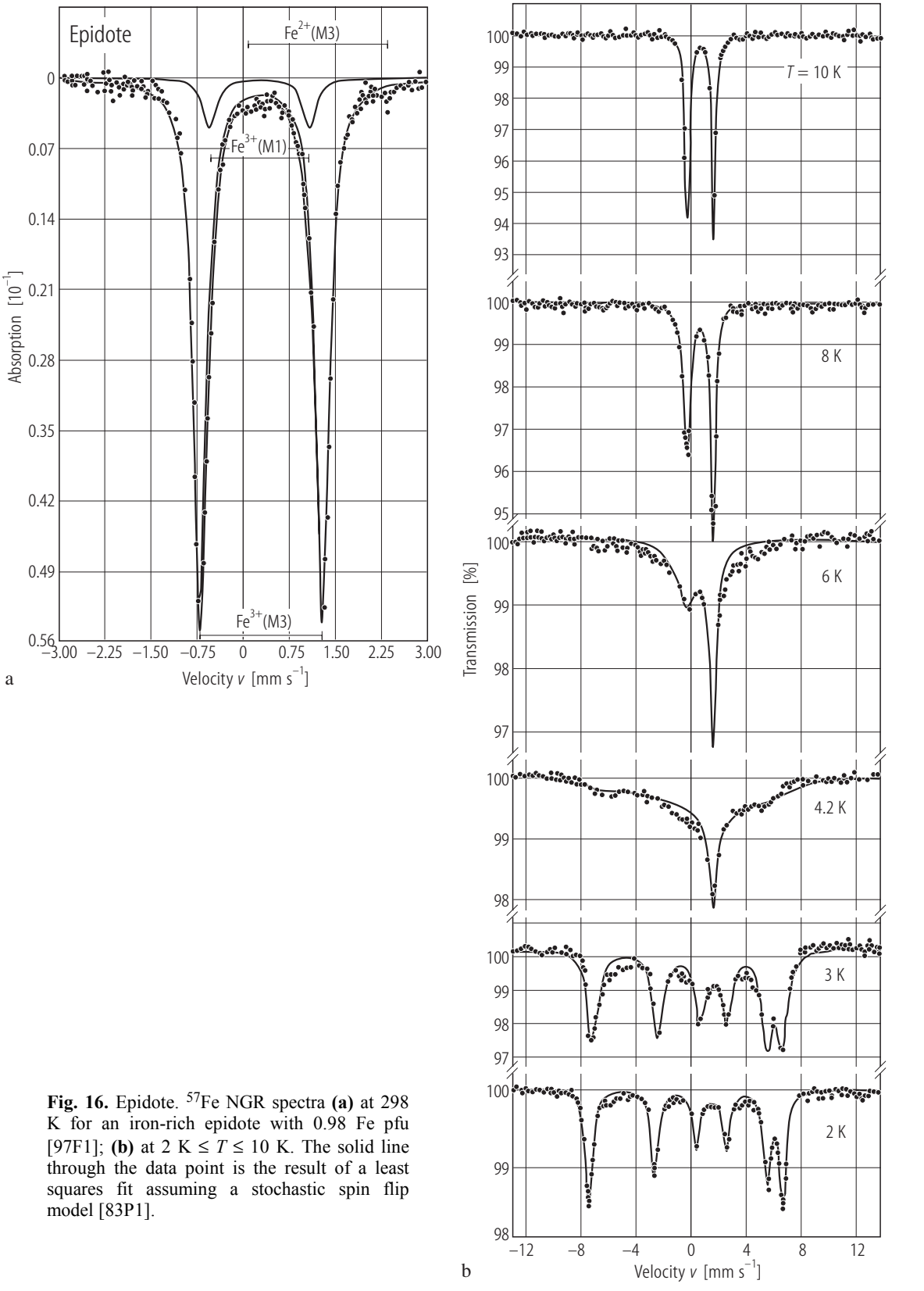

Fig. 16. Epidote. ^{57}Fe NGR spectra **(a)** at 298 K for an iron-rich epidote with 0.98 Fe pfu [97F1]; **(b)** at 2 K ≤ T ≤ 10 K. The solid line through the data point is the result of a least squares fit assuming a stochastic spin flip model [83P1].

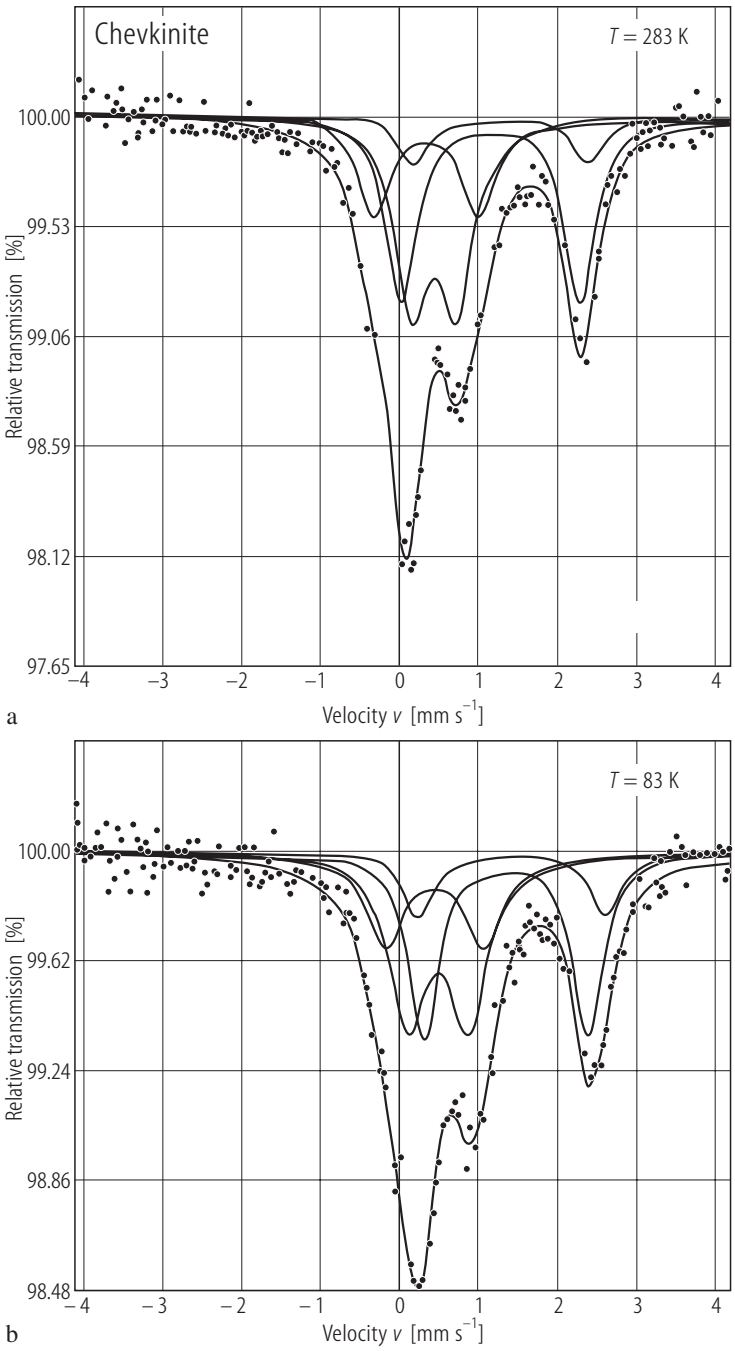

Fig. 17. Chevkinite. ^{57}Fe NGR spectra at : **(a)** 283K and **(b)** 83 K [92L1].

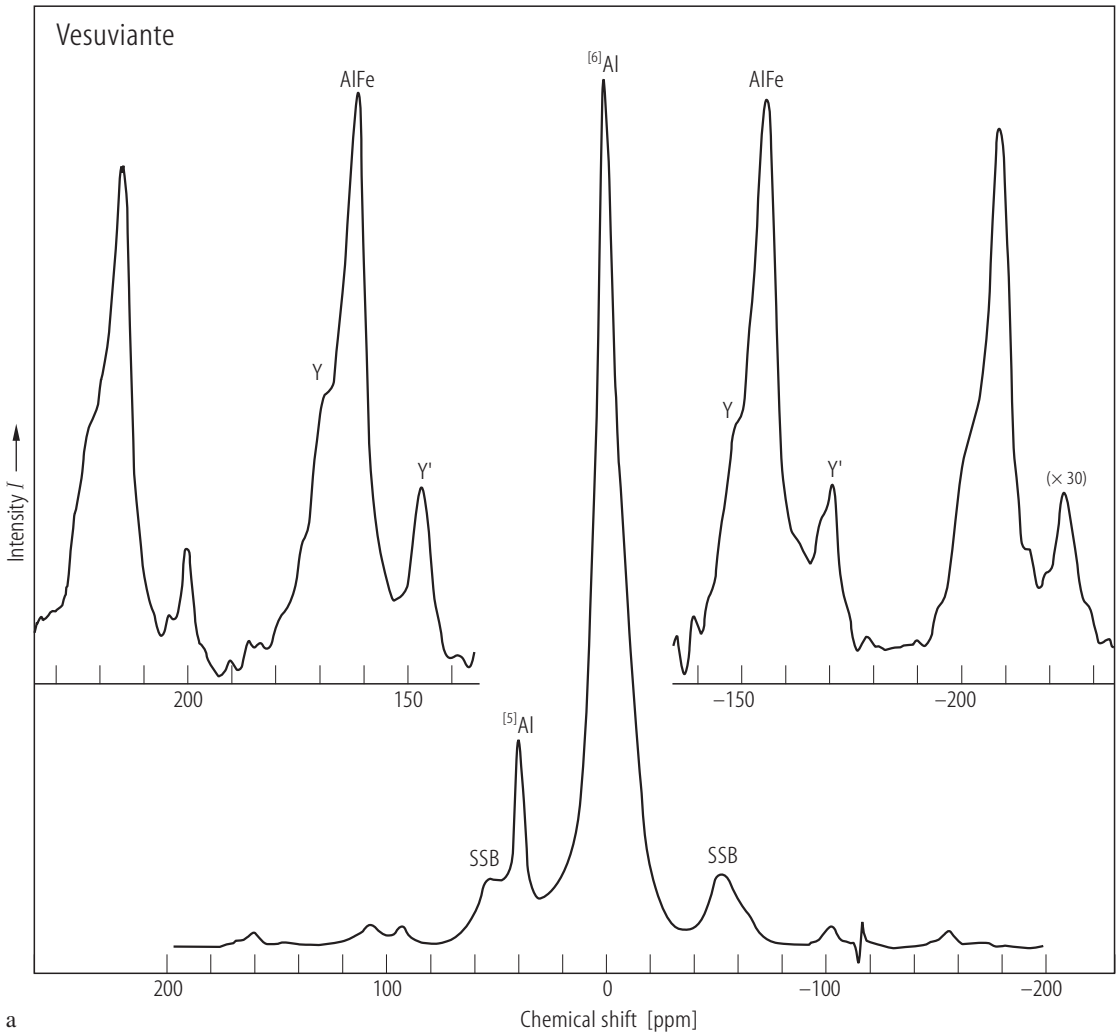

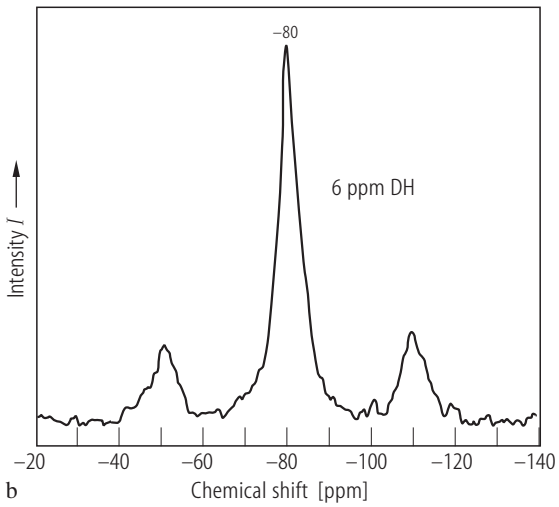

Fig. 19. Vesuvianite. **(a)** ^{27}Al NMR spectrum at 11.7 T and spinning speed of 7.1 kHz. The insets shown in expanded scale the spinning sidebands of the satellite ± (3/2,1/2) transitions. There is a signal present in the central transitions from octahedrally coordinated Al (Y) and pentahedrally coordinated Al (Y' site). The satellite sidebands show decreased linewidth relative to the central transitions allowing resolution of signal from the Y and AlFe sites. SSB are spinning sidebands of the central-transition peaks [87P1] **(b)** ^{29}Si NMR spectrum at 8.45 T and spinning at 20 kHz. The peaks for the three different Si sites cannot be resolved. By DH is denoted the full width at half height [87P1].

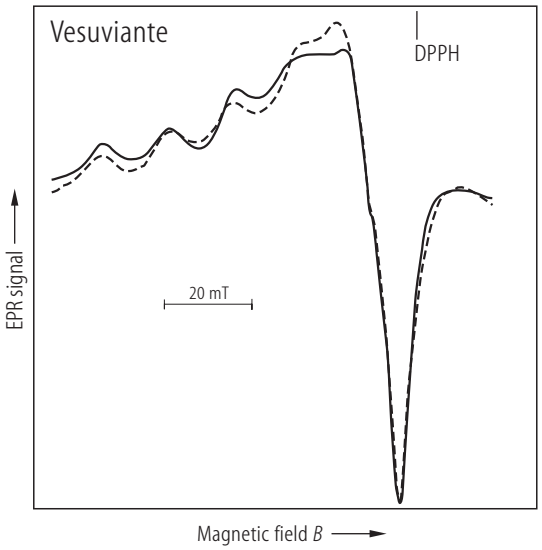

Fig. 20. Vesuvianite[106]. EPR spectrum of Cu^{2+}, at 77 K. Solid line-experimental, dashed line-simulated spectrum [92D2].

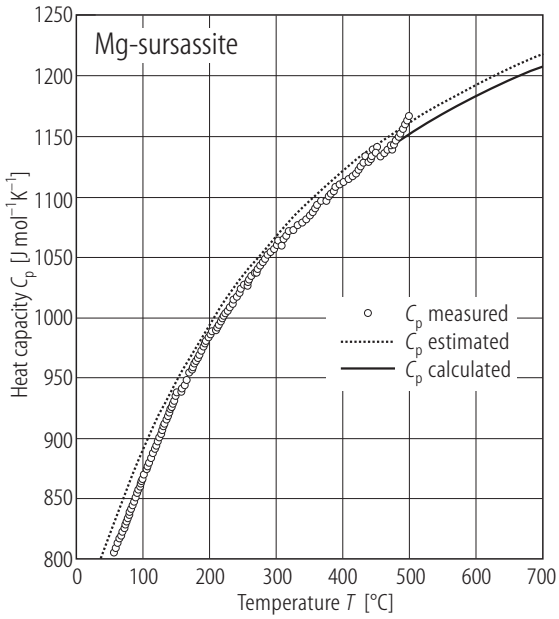

Fig. 21. Mg-sursassite. Temperature dependence of the heat capacity. The dashed curve shows the estimated C_p values obtained from the sum of its component oxides [85B1]. Calculated values are described by the relation given in text [01G1].

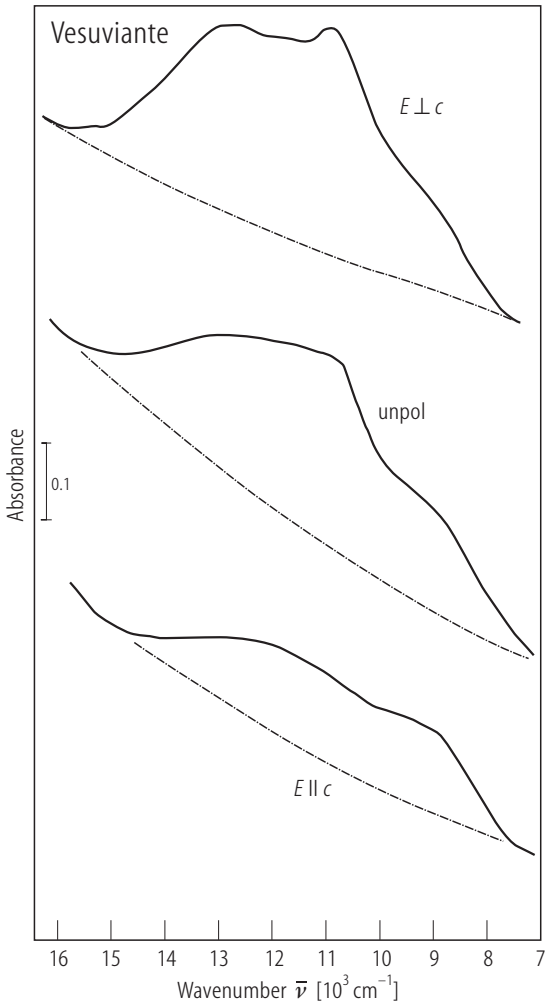

Fig. 23. Vesuvianite[102]. Optical absorption spectra (sample thickness $83 \cdot 10^{-5}$ m). ***E*** represents the polarization direction of incident light; dashed-dotted line represents estimated background [75M2].

For Fig. 22 see next page

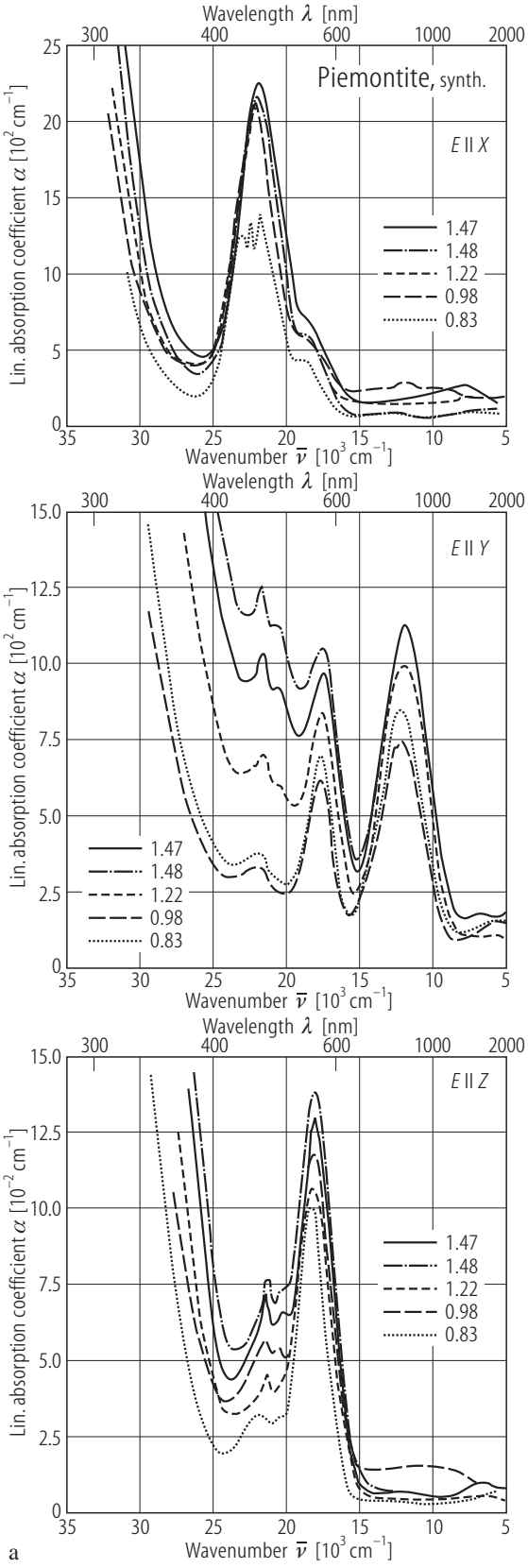

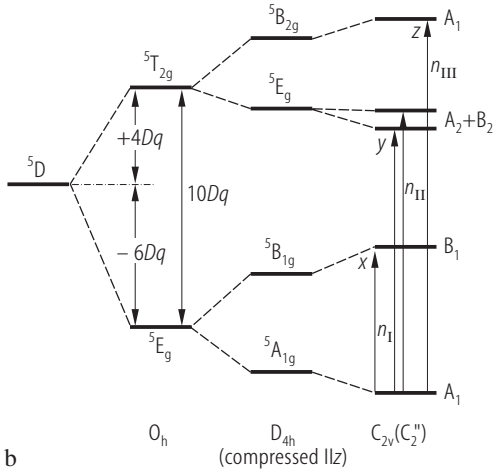

Fig. 22. Synthetic piemontites $Ca_2(Al_{3-x}Mn^{3+}_x)[OH|O|SiO_4|Si_2O_7]$. **(a)** Polarized single crystal absorption spectra $\boldsymbol{E} \parallel \boldsymbol{X}$ ($\cong \boldsymbol{c}$), $\boldsymbol{E} \parallel \boldsymbol{Y}$ ($\boldsymbol{b}$) and $\boldsymbol{E} \parallel \boldsymbol{Z}$ ($\angle \boldsymbol{a} \cong 30^o$). The ordinates are thickness normalized linear absorption coefficients [02L1]. **(b)** Schematic energy level diagram of $3d^4$ configurated Mn^{3+} in axially compressed octahedral coordination of descending symmetry. The polarizations of the symmetry allowed transitions as calculated using group theoretical methods and given for the pseudosymmetry C_{2v} (C_2") refer to the internal axes of $M3O_6$ in this point group [02L1].

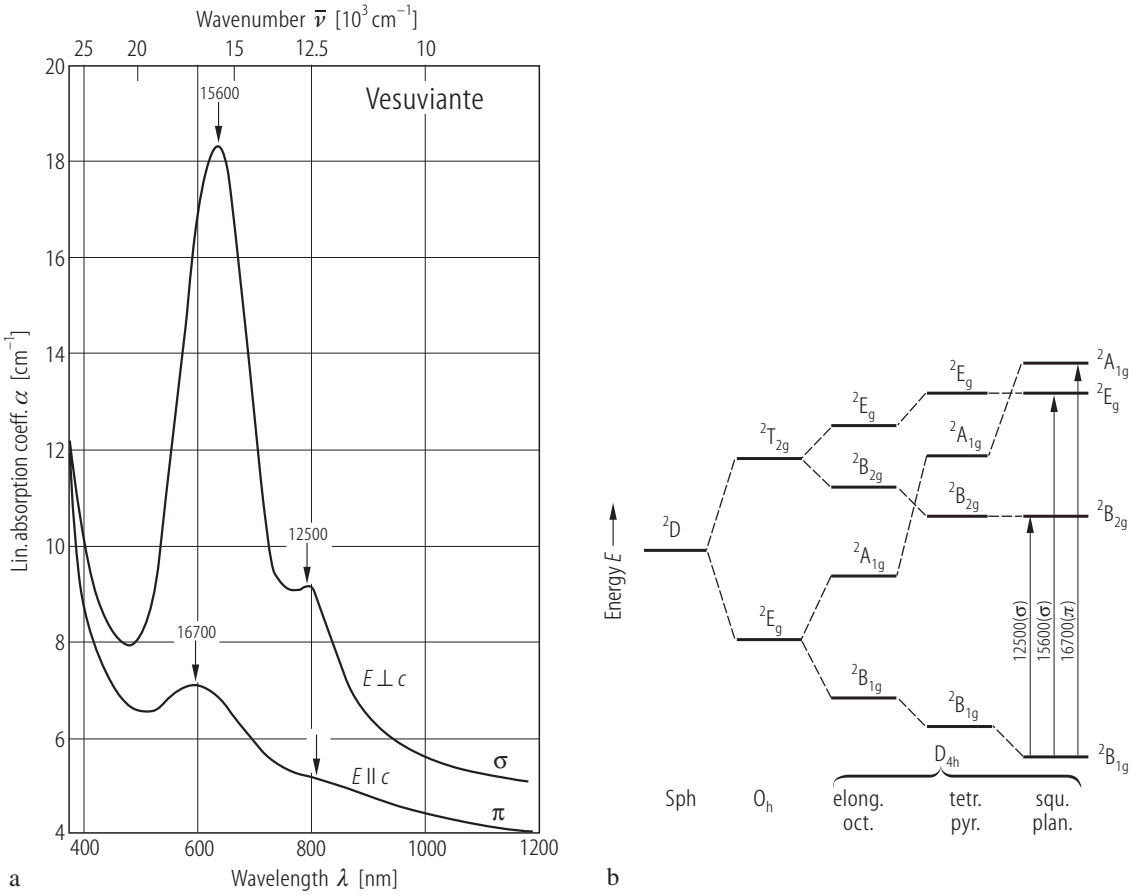

Fig. 24. Cu-bearing vesuvianite[106]. **(a)** Polarized optical absorption spectrum (α is the linear absorption coefficient). **(b)** Scheme of energy level splitting of Cu^{2+} ion in crystal fields of various symmetry [92D2]. Sph: spheric.

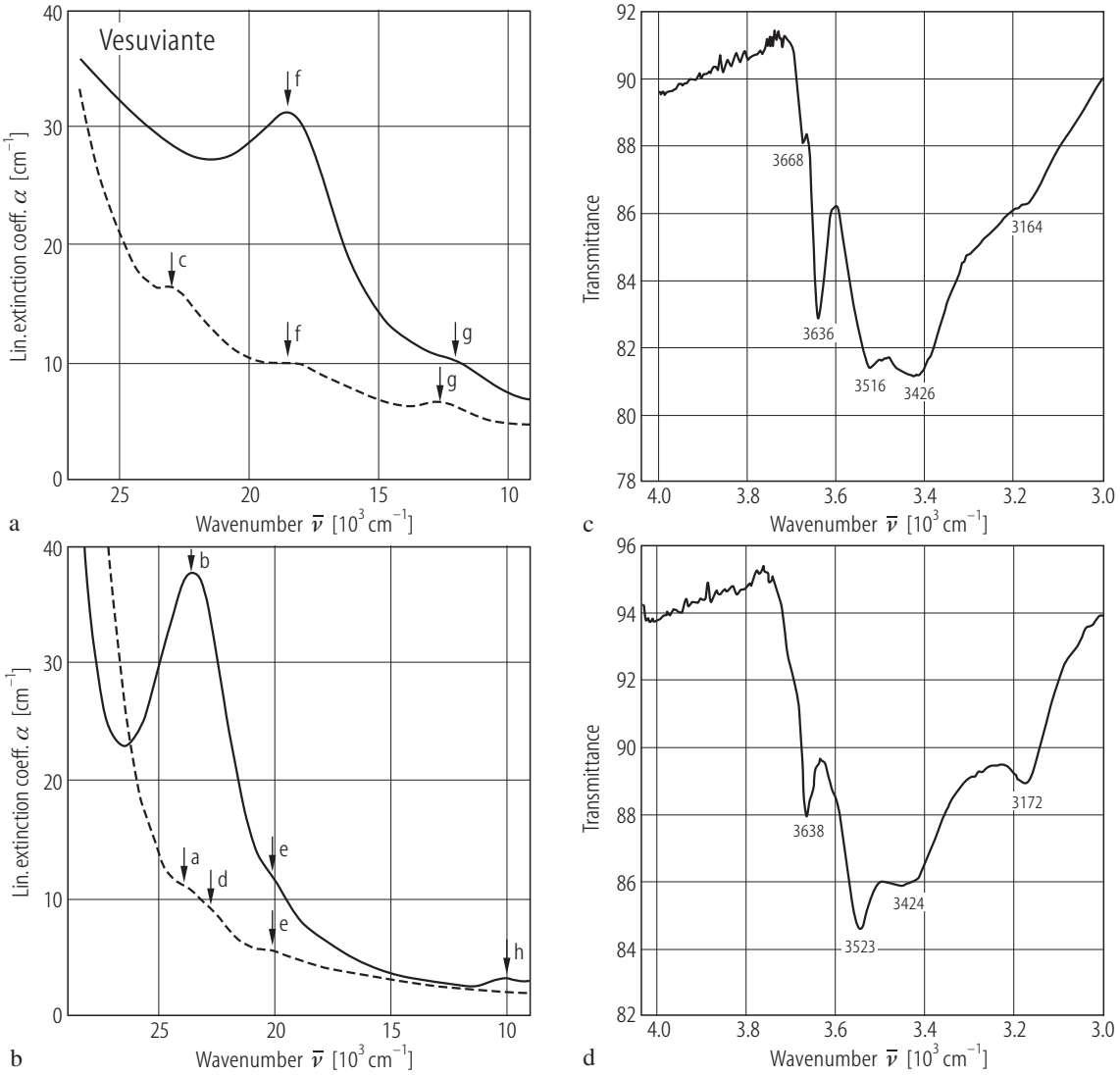

Fig. 25. Vesuvianites. Polarized absorption spectra for natural samples **(a)** [110)] and **(b)** [111)]. Broken line: ***E*** ∥ ***c***, solid line: ***E*** ⊥ ***c.*** In **(c)** and **(d)** are plotted their IR absorption spectra in the OH stretching region [95P1].

References for 8.1.2.7

27G1 Geijer, P.: Sver. Geol. Unders. 20 (1927) 1
31D1 Dunbar, C., Machatschki, F.: Z. Kristallogr. 74 (1931) 133
31W1 Warren, B.E., Modell, D.I.: Z. Kristallogr. 78 (1931) 422
41H1 Hanson, R.A., Pearce, D.W.: Am. Mineral. 26 (1941) 110
50I1 Ito, T.: X-ray Studies on Polymorphism, Maruzen Co., Tokyo, Chap 5 (1950) cited by [71D1]
51K1 Kimura, K., Nagashima, K.: J. Chem. Soc. Jpn., Pure Chem. Sect. 72 (1951) 52
53B1 Belov, N.V., Rumanova, I.M.: Dokl. Akad. Nauk SSSR 89 (1953) 853
53T1 Takubo, J., Ukai, Y., Kakitani, S.: Mineral. J. 1 (1953) 3
54I1 Ito, N., Morimoto, N., Sadanaga, R.: Acta Crystallogr. 7 (1954) 53
55F1 Fesenko, E.G., Rumanova, I.M., Belov, N.V.: Dokl. Akad. Nauk SSSR 102 (1955) 275
55U1 Ueda, T.: Mem. Coll. Sci. Univ. Kyoto B22 (1955) 145
56F1 Fesenko, E.G., Rumanova, I.M., Belov, N.V.: Kristallografiya 1 (1956) 132
59B1 Bakakin, V.V., Kravchenko, V.B., Belov, N.V.: Dokl. Akad. Nauk SSSR 129 (1959) 1155
59B2 Bonatti, S.: Am. Mineral. 44 (1959) 1145
59J1 Johansson, G.: Acta Crystallogr. 12 (1959) 522
59R1 Rumanova, I.M., Nikolaeva, I.M.: Kristallografiya 4 (1959) 829 (Sov. Phys. Crystallogr. 4 (1959) 789)
59V1 Vlasov, K.A., Kuzmenko, M.V., Eskova, E.M.: Izv. Akad. Nauk. SSSR (1959) 423
60E1 Earnshaw, A., Lewis, J.: J. Chem. Soc. (1960) 396
60G1 Gottardi, G.: Am. Mineral. 45 (1960) 1
60R1 Rumanova, I.M., Nikolaeva,I.M.: Sov. Phys. Crystallogr. 4 (1960) 789
61K1 Khvostova, V.A., Bykova, A.V.: Tr. Akad. Nauk SSSR 7 (1961) 130
62M1 Moenke, H.: Mineral Spektren, Akademie-Verlag, Berlin, 1962
63C1 Coster, M., Pollak, H., Amelinckx, S.: Phys. Status Solidi 3 (1963) 283
63K1 Khvostova, V.A.: Dokl. Akad. Nauk SSSR, Earth Science Sect. 141 (1963) 1307
64B1 Brun, E., Ghose, S.: J. Chem. Phys. 40 (1964) 3031
64K1 Kumskova, N.M., Khvostova, V.A.: Gheochem. Int. 4 (1964) 676
64P1 Pen, C.C., Pan, C.L.: Sci. Sin. 13 (1964) 1539
64S1 Strens, R.G.J.: Nature 9201 (1964) 175
64W1 Wappler, G.: Z. Phys. Chem. 228 (1964) 34
66B1 Bonatti, S., Gottardi, G.: Period. Mineral. 35 (1966) 69
66K1 Keller, G.V.: in Handbook of Physical Constants, Ed. S.P.Clark, Geol. Soc., Am. Memoir 97 (1966) 553
67B1 Bancroft, G.M., Burns, R.G., Maddock, A.G.: Acta Crystallogr. 22 (1967) 934
67B2 Bancroft, G.M., Maddock, A.G., Burns, R.G.: Geochim. Cosmochim Acta 31 (1967) 2219
67B3 Burns, R.G., Strens, R.G.J.: Mineral. Mag. 36 (1967) 204
67I1 Ito, J.: Am. Mineral. 32 (1967) 1094
68B1 Blume, M., Tjon, J.A.: Phys. Rev. 165 (1968) 446
68D1 Dollase, W.A.: Am. Mineral. 53 (1968) 1882
68D2 Donnay, G., Allmann, R.: Acta Crystallogr. B 24 (1968) 845
68K1 Kalinin, Ye.P, Yuskin, N.P., Goldin, B.A.: Zap. Vses. Mineral. Ova. 97 (1968) 647
69A1 Arem, J.E., Burnham, C.W.: Am. Mineral. 54 (1969) 1547
69B1 Brinkmann, D., Staehli, J.L., Ghose, S.: J. Chem. Phys. 51 (1969) 5128
69D1 Dollase, W.A.: Am. Mineral. 54 (1969) 710
69S1 Shepel, A.B., Karpenko, M.V.: Dokl. Akad. Nauk SSSR 185 (1969) 1342
69T1 Thorpe, A.N., Senftle, F.E., Donnay, G.: J. Phys. Chem. Solids 30 (1969) 2235
70C1 Coda, A., Della Giusta, A., Isetti, G., Mazzi, F.: Atti Accad. Sci. Torino 105 (1970) 63
70L1 Linke, W.: Tschermaks Mineral. Petrogr. Mitt. 14 (1970) 61
71A1 Allmann, R., Donnay, G.: Acta Crystallogr. B 27 (1971) 1871
71D1 Dollase, W.A.: Am. Mineral. 56 (1971) 447

71G1 Ghose, S., Tsang, T.: Science 171 (1971) 374
71H1 Hutton, D.R.: J. Phys. C: Solid State Phys. 4 (1971) 1251
71I1 Ito, J., Arem, E.: Am. Mineral 56 (1971) 307
71T1 Tung, S., Ghose, S.: J. Chem. Phys. 54 (1971) 856
73D1 Dollase, W.A.: Z. Kristallogr. 138 (1973) 41
73G1 Gabe, E.J., Portheine, J.C., Whitlow, S.H.: Am. Mineral 58 (1973) 218
74C1 Calvo, C., Faggiani, R.: Am. Mineral 59 (1974) 1277
74L1 Langer, K., Raith, M.: Am. Mineral. 59 (1974) 1249
74M1 Moëlo, Y., Choutier, I.P., Gilles, C.: Bull. Soc. Fr. Miner. Cristallogr. 97 (1974) 521
74P1 Phillips, M.W., Gibbs, G.V., Ribbe, P.H.: Am. Mineral. 59 (1974) 79
75M1 Manning, P.G.: Can. Mineral. 13 (1975) 110
75M2 Manning, P.G., Triker, M.J.: Can. Mineral. 13 (1975) 259
75P1 Pollak, H., Bruyneel, W.: Proc. Int. Conf. Mössbauer Spectroscopy, A.Z.Hrynkiewicz, J.A. Sawicki (eds.), Krakow, Poland, 1975, p. 259
75R1 Rucklindge, J.C., Kocman, V., Whitlow, S.H., Gabe, E.J.: Can. Mineral. 13 (1975) 15
76L1 Langer, K., Anastasiou, P., Abs-Wurmbach, I.: Proc. 25th Int. Geol.Congr., Sidney, 1976, vol. 2, p. 578
76L2 Langer, K., Abu-Eid, R.M., Anastasiou, P.: Z. Kristallogr. 144 (1976) 434
76M1 Manning, P.G.: Can. Mineral. 14 (1976) 215
77A1 Anastasiou, P., Langer, K.: Contrib. Mineral. Petrol. 60 (1977) 225
77M1 Manning, P.G.: Can. Mineral. 15 (1977) 508
77W1 Williams, S.A., Duggan, M.: Mineral. Mag. 41 (1977) 429
78N1 Nozik, Y.Z., Kanepit, V.N., Fukin, L.Y., Makarov, Y.S.: Geochem. Int. 15 (1978) 66
78S1 Segalstad, T.V., Larsen, A.O.: Am. Mineral. 63 (1978) 499
79D1 Dornberg-Schiff, K.: Krist. Tech. 14 (1979) 1027
79K1 Keskinen, M., Liou, J.G.: Am. Mineral. 64 (1979) 317
79M1 Moore, P.B., Ito, J., Steele, I.M.: Mineral. Mag.43 (1979) 325
80B1 Bird, D.K., Helgeson, H.C.: Am. J. Sci. 280 (1980) 907
80C1 Carbonin, S., Molin, G.: Neues Jahrb. Mineral. Abh. 139 (1980) 205
80L1 Langer, K., Lattard, D.: Am. Mineral. 65 (1980) 779
80S1 Schiffman, P., Liou. J.G.: J. Petrol. 21 (1980) 441
81B1 Brooks, C.K., Henderson, P., Ronsbo, J.G.: Mineral. Mag. 44 (1981) 157
81O1 Olhoeft, G.R.: in Physical Properties of Rocks and Minerals, Y.S. Touloukian (ed.), Mc Graw Hill, New York, 1981, p. 257
82M1 Mellini, M., Merlino, S.: Proc. 13th General Meeting, IMA ‘89, Varna, Bulgaria, p. 373
82S1 Smith, G., Halenius, U., Langer, K.: Phys. Chem. Miner. 8 (1982) 138
83D1 Dunn, P.J., Peacor, D.R.: Am. Mineral. 68 (1983) 1029
83G1 Giuseppetti, G., Mazzi, F.: Tschermaks Mineral. Petrogr. Mitt. 31 (1983) 277
83H1 Haggerty, S.E., Mariano, N.M.: Contrib. Mineral. Petrol. 84 (1983) 365
83P1 Peasano, A., Kunrath, J.I., Vasquez, A.: Hyperfine Interact. 15-16 (1983) 841
84D1 Dunn, P.J., Cabri, L.J., Ferraiolo, J.A., Grice, J.D., Jambor, J.L., Mueller, W., Shigley, J.E., Puziewicz, J., Vanko, D.A.: Am. Mineral. 69 (1984) 1190
84M1 Mellini, M., Merlino, S., Pasero, M.: Phys. Chem. Miner. 10 (1984) 99
85B1 Berman, R.G., Brown, T.H.: Contrib. Mineral. Petrol. 89(1985) 168
85D1 Dunn, P.J.: Mineral. Mag. 49 (1985) 721
85M1 Moore, P.B., Shen, J., Araki, T.: Am. Mineral. 70 (1985) 171
85S1 Sugiyama, K., Takeuchi, Y.: Z. Kristallogr. 173 (1985) 293
85V1 Valley, J.W., Peacor, D.R., Bowman, J.R., Essene, E.J., Allard, M.J.: J. Metamorph. Geol. 3 (1985) 137
86F1 Fitzgerald, S., Rheingold, S., Leavens, P.B.: Am. Mineral. 71 (1986) 1010
86F2 Fitzgerald, S., Rheingold, A.L., Leavens, P.B.: Am. Mineral. 71 (1986) 1483
86M1 Mellini, M., Merlino, S., Pasero, M.: Am. Mineral. 71 (1986) 176
86R1 Ray, N.J., Putnis, A., Gillet, P.: Bull. Mineral. 109 (1986) 667

86S1 Schreyer, W., Maresch, W.V., Mendenbach, O., Baller, T.: Nature 321 (1986) 510
86Y1 Yoshiasa, A., Matsumoto, T.: Mineral. J. 13 (1986) 1
87B1 Beran, A.: Phys. Chem. Miner. 14 (1987) 441
87B2 Büscher, R., Such, K.P., Lehmann, G.: Phys. Chem. Miner. 14 (1987) 553
87P1 Phillips, B.L., Allen, F.M., Kirkpatrick, R.J.: Am. Mineral. 72 (1987) 1190
87S1 Stergiou, A.C., Rentzeperis, P.J., Sklavounos, S.: Z. Kristallogr. 178 (1987) 297
87T1 Treloar, P.J., Charnley, N.R.: Can. Mineral. 25 (1987) 413
88B1 Bird, D.K., Cho, M., Janik, C.J., Liou, J.G., Canuso, L.J.: J. Geophys. Res. 93 (1988) 13135
88C1 Cressey, G., Steel, A.T.: Phys. Chem. Miner. 15 (1988) 304
88K1 Kvick, A., Pluth, J.J., Richardson, J.W., Smith, J.V.: Acta Crystallogr. B4 (1988) 351
88P1 Peacor, D.R., Dunn, P.J.: Am. Mineral. 73 (1988) 838
88S1 Sundberg, M.R., Valkonen, J., Kivekas, R., Koljonen, T., Malisa, E.: Z. Kristallogr. 185 (1988) 617
89W1 Winkler, B., Langer, K., Johannsen, P.G.: Phys. Chem. Miner. 16 (1989) 668
91G1 Grew, E.S., Esssene, E.J., Peacor, D.R., Su, S.C., Asami, M.: Am. Mineral. 76 (1991) 1990
91N1 Nickel, E.H., Nichols, M.C.: Mineral Reference Manual, Van Nostrand Reinhold, 1991
91P1 Pasero, M., Reinecke, T.: Eur. J. Mineral. 3 (1991) 819
91P2 Patrier, P., Beaufort, D., Meunier, A., Eymery, J.P., Petit, S.: Am. Mineral. 75 (1991) 602
91S1 Schreyer, W., Marech, W.V., Baller, T.: In Progress in Metamorphic and Magmatic Petrology, LL. Perchuk (ed.), Cambrige University Press, U.K., 1991 p.47
91S2 Sokolova, E.V., Nadezhina, T.N., Pantov, L.A.: Sov. Phys. Crystallogr. 36 (1991) 172
91V1 Veblen, D.R., Wiechmann, M.J.: Am. Mineral. 76 (1991) 397
92A1 Allen, F.M., Burnham, C.W.: Can. Mineral. 30 (1992) 1
92D1 Downs, J.W., Swope, R.J.: J. Phys. Chem. 96 (1992) 4834
92D2 Dyrek, K., Platonov, A.N., Sojka, Z., Zabinski, W.: Eur. J. Mineral. 4 (1992) 1285
92G1 Groat, L.A., Hawthorne, F.C., Ercit, T.S.: Can. Mineral. 30 (1992) 19
92G2 Groat, L.A., Hawthorne, F.C., Ercit, T.S.: Can. Mineral. 30 (1992)1065
92H1 Hackwell, T.P., Angel, R.J.: Eur. J. Mineral. 4 (1992) 1221
92L1 Li, Z., Jin, M., Liu, M., Liu, X.: Hyperfine. Interact. 70 (1992) 1057
92O1 Ohkawa, M., Yoshiasa, A., Takeno, S.: Am. Mineral. 77 (1992) 945
92S1 Shannon, R.D., Rossman, G.R.,: Phys. Chem. Miner. 19 (1992) 157
93B1 Bonazzi, P., Menchetti, S., Reinecke, T.: Plinius 10 (1993) 78
93G1 Groat, L.A., Hawthorne, F.C., Ercit, T.S., Putnis, A.: Can. Mineral. 31 (1993) 617
93J1 Janeczek, J., Eby, R.K.: Phys. Chem. Miner. 19 (1993) 343
93R1 Rouse, R.C., Peacor, D.R.: Can. Mineral. 31 (1993) 153
94B1 Bonazzi, P., Menchetti, S.: Am. Mineral. 79 (1994) 1176
94G1 Groat, L.A., Hawthorne, F.C., Ercit, T.S.: Can. Mineral. 32 (1994) 497
94G2 Groat, L.A., Hawthorne, F.C., Ercit, T.S.: Can. Mineral. 32 (1994) 505
95A1 Artioti, G., Quartieri, S., Deriu, A.: Can. Mineral. 33 (1995) 67
95B1 Bonazzi, P., Menchetti, S.: Mineral. Petrol. 53 (1995) 133
95G1 Groat, L.A., Hawthorne, F.C., Rossman, G.R., Ercit, T.S.: Can. Mineral. 33 (1995) 609
95L1 Li, D., Bancroft, G.M., Fleet, M.E., Feng, X.N.: Phys. Chem. Miner. 22 (1995) 115
95P1 Platonov, A.N., Zabinski, W., Sachanbinski, M.: Eur. J. Mineral. 7 (1995) 1345
95R1 Rager, H., Zabinski, W.: Neues Jahrb. Mineral. (1995) 264 (is incomplete ?)
96G1 Groat, L.A., Hawthorne, F.C., Lager, G.A. Schultz, A.J., Ercit, T.S.: Can. Mineral. 34 (1996) 1059
96Z1 Zabinski, W.: Phys. Chem. Miner. 23 (1996) 23
97F1 Fehr, K.T., Heuss-Assbichler, S.: Neues Jahrb. Mineral. Abh.. (1997) 43
98G1 Groat, L.A., Hawthorne, F.C., Ercit, T.S., Grice, J.D.: Can. Mineral. 36 (1998) 1301
98P1 Pavese, A., Prencipe, M., Tribaudino, M., Aagaard, St.S.: Can. Mineral. 36 (1998) 1029
98P2 Poli, S., Schmidth, M.W.: Contrib. Mineral. Petrol. 130 (1998) 162
99A1 Artioli, G., Fumagalli, P., Poli, S.: Am. Mineral. 84 (1999) 1906
99G1 Giuli, G., Bonazzi, P., Merchetti, S.: Am. Mineral. 84 (1999) 933
99L1 Langer, G.A., Xie, Q., Ross, F.K., Rossman, G.R., Armbruster, Th., Rotella, F.J., Schultz, A.J.: Can. Mineral. 34 (1999)

00A1 Armbruster, T., Gros, E.: Am. Mineral. 85 (2000) 563
00G1 Gottschalk, M., Fockenberg, T., Grevel, K.D., Wunder, B., Wirth, R., Schreyer, W., Maresch, U.V.: Eur. J. Mineral. 12 (2000) 935
01G1 Grevel, K.D., Navrotsky, A., Kahl, W.A., Fasshauer, D.W., Magzlan, J.: Phys. Chem. Miner. 28 (2001) 475
01G2 Grodzicki, M., Heuss-Assbichler, S., Amthauer, G: Phys. Chem. Miner. 28 (2001) 675
02L1 Langer, K., Tillmanns, E., Kersten, M., Almen, H., Arni, R.K.: Z. Kristallogr. 217 (2002) 563
02L2 Liebscher, A., Gottschalk, M., Franz, G.: Am. Mineral. 87 (2002) 909